Aus dem Bereich Physiologie

Theoretische Medizin und Biowissenschaften

der Medizinischen Fakultät

der Universität des Saarlandes, Homburg/Saar

Automated detection and analysis of fluorescence changes evoked by molecular signalling

Dissertation

zur Erlangung des akademischen Grades eines

Doktors der Naturwissenschaften

der Medizinischen Fakultät

der UNIVERSITÄT DES SAARLANDES

2022

vorgelegt von: Gebhard Stopper

geb. am: 31.10.1985 in Heilbronn

Date of examination	01.06.2022

Dean of the faculty: **Univ.-Prof. Dr. med. Michael D. Menger**

Examinants: **Prof. Dr. Frank Kirchhoff -** University of Saarland

Prof. Dr. Peter Lipp – University of Saarland

Eidesstattliche Erklärung

Ich erkläre hiermit an Eides statt, dass ich die vorliegende Arbeit ohne unzulässige Hilfe Dritter und ohne Benutzung anderer als der angegebenen Hilfsmittel angefertigt habe. Die aus anderen Quellen direkt oder indirekt übernommenen Daten und Konzepte sind unter Angabe der Quelle gekennzeichnet.

Bei der Auswahl und Auswertung folgenden Materials haben mir die nachstehend aufgeführten Personen in der jeweils beschriebenen Weise

☒unentgeltlich:

☐entgeltlich geholfen:

> Operationen zur Implantation Kranialer Fenster, Kainat Injektionen, sowie EEG Messungen wurden durchgeführt von Laura C. Caudal, CIPMM, Homburg, Universität des Saarlandes

> Na^+ Experimente und Messungen wurden durchgeführt von Lisa Felix und Katharina Everaerts, Institut für Neurobiologie, Heinrich Heine Universität, Düsseldorf

Weitere Personen waren an der inhaltlich-materiellen Erstellung der vorliegenden Arbeit nicht beteiligt. Insbesondere habe ich nicht die entgeltliche Hilfe von Vermittlungs- bzw. Beratungsdiensten (Promotionsberaterinnen/Promotionsberater oder anderer Personen) in Anspruch genommen. Außer den Angegebenen hat niemand von mir unmittelbar oder mittelbar geldwerte Leistungen für Arbeiten erhalten, die im Zusammenhang mit dem Inhalt der vorgelegten Dissertation stehen.

Die Arbeit wurde bisher weder im Inland noch im Ausland in gleicher oder in ähnlicher Form in einem anderen Verfahren zur Erlangung des Doktorgrades einer anderen Prüfungsbehörde vorgelegt.

Ich versichere an Eides statt, dass ich nach bestem Wissen die Wahrheit gesagt und nichts verschwiegen habe.

Die Bedeutung der eidesstattlichen Erklärung und die strafrechtlichen Folgen einer unrichtigen oder unvollständigen eidesstattlichen Erklärung sind mir bekannt.
Ort, Datum

Unterschrift der/des Promovierenden

"Study hard what interests you the most in the most undisciplined,

irreverent and original manner possible."

- Richard Feynman -

Table of contents

I. Abbreviations

2P-LSM	Two-photon excitation laser-scanning microscopy
ACSF	Artificial cerebrospinal fluid
ATP	Adenosine triphosphate
CaM	Calmodulin
CNS	Central nervous system
DFT	Discrete Fourier transform
ECoG	Electrocorticogramm
EEG	Electroencephalography
ER	Endoplasmic reticulum
FFT	Fast Fourier transform
FOV	Field of view
GABA	γ-Aminobutyric acid
GECI	Genetically encoded calcium indicator
GEFI	Genetically encoded fluorescence indicator
GFP	Green fluorescent protein
i.p.	Intraperitoneal
iEEG	Intracranial EEG
IP$_3$	Inositol trisphosphate
LSM	Laser scanning microscopy
NMDA	*N*-methyl-D-aspartate
PDF	Portable document format
ROI	Region of interest
s.c.	Subcutaneous
SBFI-AM	Sodium-binding benzofuran isophthalate-acetoxymethyl ester
SLM	Selective laser melting
UI / GUI	User interface / Graphical user interface

$$\overline{\underline{x}}$$

II. **List of figures**

III. **List of tables**

1 Zusammenfassung

Fluoreszenzfarbstoffe und genetisch kodierte Fluoreszenzindikatoren (GEFI) sind gängige Werkzeuge zur Visualisierung von Konzentrationsänderungen bestimmter Ionen und Botenmoleküle der intra- sowie interzellulären Kommunikation. Während Fluoreszenzfarbstoffe direkt in die Zielzellen eingebracht werden müssen und nur über einen begrenzten Zeitraum funktionieren, kann die Expression von GEFIs zell- und zeitspezifisch gesteuert werden, was darüber hinaus Langzeitanalysen in lebenden Organismen ermöglicht. Farbstoff- und GEFI-basierte Fluoreszenzfluktuationen, die mit Hilfe moderner bildgebender Verfahren aufgezeichnet werden, bilden die Grundlage für die Analyse physiologischer molekularer Kommunikation. Die Analyse einer großen Zahl komplexer Fluoreszenzsignale ist jedoch eine schwierige und zeitaufwändige Aufgabe. Eine automatisierte Analyse ist dagegen weniger zeitaufwändig und unabhängig von der Voreingenommenheit des Anwenders. Allerdings müssen hierzu mehrere Herausforderungen bewältigt werden. Unter anderem die korrekte Schätzung von Fluoreszenzschwankungen bei Basalkonzentrationen von Botenmolekülen, die Detektion und Extraktion von Signalen selbst, die korrekte Segmentierung benachbarter Signale sowie die Verfolgung sich ausbreitender Signale. Darüber hinaus müssen die Algorithmen zur Signalerkennung empfindlich genug sein, um lokalisierte Signale mit geringer Amplitude sowie begrenzter räumlicher Ausdehnung genau zu erfassen.

In dieser Arbeit werden drei neue Algorithmen, PBasE, CoRoDe und KalEve, für die automatische Extraktion und Analyse von Fluoreszenzsignalen vorgestellt, die entwickelt wurden, um die oben genannten Herausforderungen zu bewältigen. Die Algorithmen sind in eine grafische Anwendung namens MSparkles integriert, die speziell für die Analyse von Fluoreszenzsignalen entwickelt und in MATLAB implementiert wurde. Die Fähigkeiten der Algorithmen werden anhand der Analyse astroglialer Ca^{2+}-Signale demonstriert, die in narkotisierten sowie wachen Mäusen aufgezeichnet und mit den genetisch kodierten Ca^{2+}-Indikatoren (GECIs) GCaMP3 und GCaMP5 visualisiert wurden. Erlangte Ergebnisse werden anschließend mit denen anderer Softwarepakete verglichen. Darüber hinaus dient die Analyse neuronaler Na^+-Signale, die in akuten Hirnschnitten mit SBFI-AM aufgezeichnet wurden, dazu, den breiten Anwendungsbereich der Algorithmen aufzuzeigen. Zu guter Letzt wird aufgrund der zunehmenden Indizien auf die zentrale Rolle von Astrozyten bei neurodegenerativen Erkrankungen wie Epilepsie eine Metrik zur Bewertung des synchronen Auftretens fluoreszenter Signale eingeführt. In einer Proof-of-Principle-Analyse wird diese Metrik verwendet, um astrogliale Ca^{2+}-Signale mit EEG-Messungen zu korrelieren.

2 Abstract

Fluorescent dyes and genetically encoded fluorescence indicators (GEFI) are common tools for visualizing concentration changes of specific ions and messenger molecules during intra- as well as intercellular communication. While fluorescent dyes have to be directly loaded into target cells and function only transiently, the expression of GEFIs can be controlled in a cell and time-specific fashion, even allowing long-term analysis in living organisms. Dye and GEFI based fluorescence fluctuations, recorded using advanced imaging technologies, are the foundation for the analysis of physiological molecular signaling. Analyzing the plethora of complex fluorescence signals is a laborious and time-consuming task. An automated analysis of fluorescent signals circumvents user bias and time constraints. However, it requires to overcome several challenges, including correct estimation of fluorescence fluctuations at basal concentrations of messenger molecules, detection and extraction of events themselves, proper segmentation of neighboring events as well as tracking of propagating events. Moreover, event detection algorithms need to be sensitive enough to accurately capture localized and low amplitude events exhibiting a limited spatial extent.

This thesis presents three novel algorithms, PBasE, CoRoDe and KalEve, for the automated analysis of fluorescence events, developed to overcome the aforementioned challenges. The algorithms are integrated into a graphical application called MSparkles, specifically designed for the analysis of fluorescence signals, developed in MATLAB. The capabilities of the algorithms are demonstrated by analyzing astroglial Ca^{2+} events, recorded in anesthetized and awake mice, visualized using genetically encoded Ca^{2+} indicators (GECIs) GCaMP3 as well as GCaMP5. The results were compared to those obtained by other software packages. In addition, the analysis of neuronal Na^+ events recorded in acute brain slices using SBFI-AM serve to indicate the putatively broad application range of the presented algorithms. Finally, due to increasing evidence of the pivotal role of astrocytes in neurodegenerative diseases such as epilepsy, a metric to assess the synchronous occurrence of fluorescence events is introduced. In a proof-of-principle analysis, this metric is used to correlate astroglial Ca^{2+} events with EEG measurements.

3 Introduction

3.1 The central nervous system
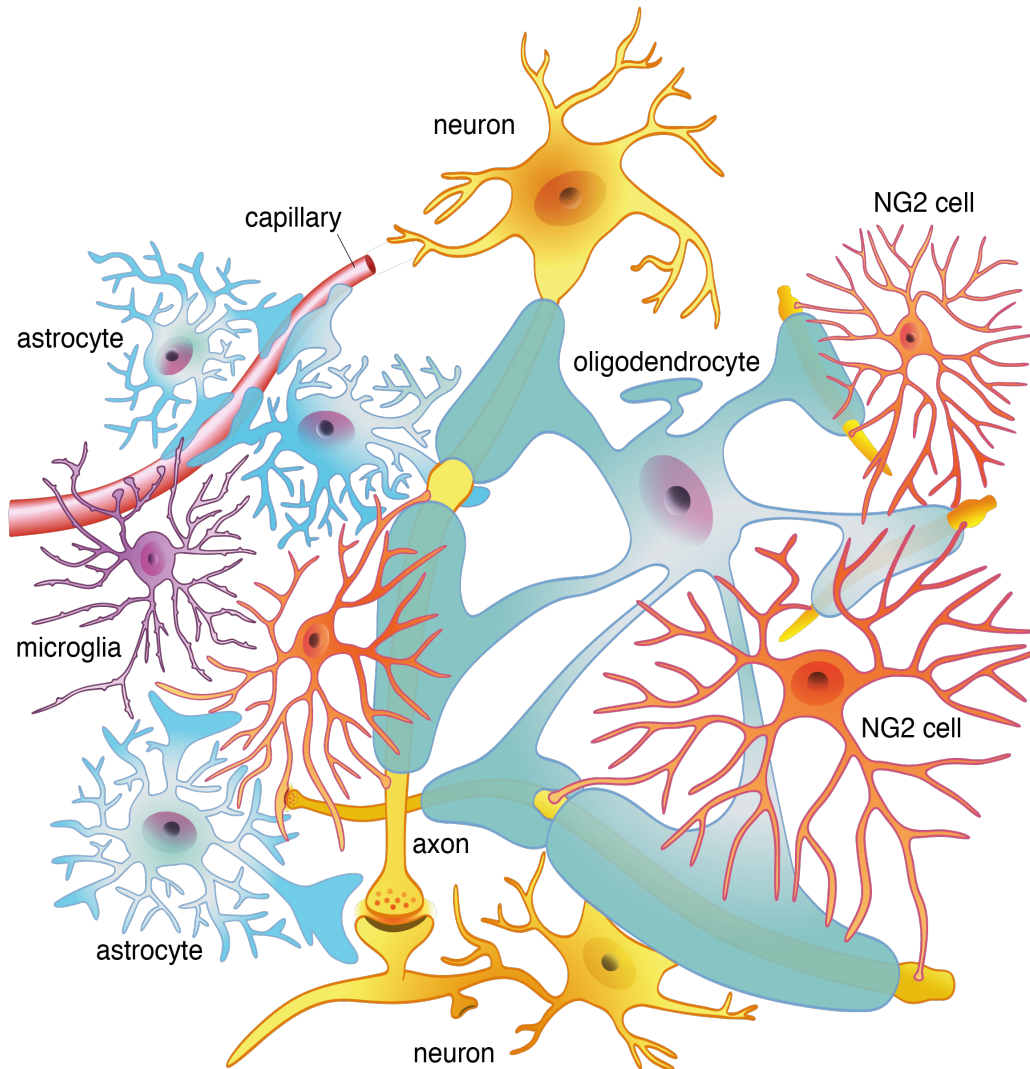
Figure 1: Cells in the CNS. *Glial cells and neurons (yellow) closely interact throughout the entire CNS. Microglia (purple) are the primary immune cells of the CNS surveilling their vicinity. Oligodendrocytes (cyan) ensheathe neuronal axons. Astrocytes (blue) are in contact with capillaries and participate in tripartite synapses. NG2 glia (red) connect to nodes of Ranvier and maintain close proximity to synapses.*

The central nervous system (CNS) consists of two predominant classes of cells - neurons and glial cells. Glial cells far exceed neurons in cellular diversity and function (Fields et al., 2014). Both, glial cells and neurons maintain close contact and interact throughout the entire CNS (Figure 1). In contrast to neurons, glial cells do not generate action potentials (Fields et al., 2014), but communicate via the release of gliotransmitters (Araque et al., 2014), like glutamate, adenosine triphosphate (ATP) or γ-aminobutyric acid (GABA). Various types of glial cells are not only classified based on their function, but with regard to their location within the CNS.

3.2 Neurons

Neurons (Figure 1, yellow) are electrically excitable cells (Rutecki, 1992), communicating via the release of neurotransmitters at their synapses. Each synapse thereby consists of a presynapse at the end of a neuron's axon, where neurotransmitters are released and the postsynapse, located on a dendrite of the receiving neuron (Campbell et al., 2011). Neuronal axons are ensheathed by myelin layers (Figure 1, cyan), produced by oligodendrocytes, providing electric insulation for fast signal propagation. Myelinated sections are intercepted by nodes of Ranvier, short unmyelinated gaps, increasing the conduction velocity and ultimately resulting in the characteristic saltatory conduction of action potentials. In recent years it has become evident that glial cells play a major role in neurodegenerative diseases, especially in the context of epilepsy (Carmignoto and Haydon, 2012; Heuser et al., 2018). Therefore, a compound analysis of glial molecular signalling and neuronal electrical signals has the potential to reveal new insights into the underlying processes of neurodegenerative diseases.

3.3 Glial cells

Microglia (Figure 1, purple) are the resident macrophage cells of the CNS, providing the brains primary immune response (Filiano et al., 2015). Each microglia is continuously monitoring its surrounding by extending and retracting its processes. Territories of neighboring microglia cells are non-overlapping (Kettenmann and Verkhratsky, 2013). Upon detection of e.g. an inflammation or necrotic event, microglia migrate towards the affected region and transition into a reactive state. Thereby, they undergo a morphological transformation from ramified to an amoeboid shape (Stopper et al., 2018).

NG2-glia cells (Figure 1, red), also referred to as oligodendrocyte precursor cells or polydendrocytes, are not only precursor cells to oligodendrocytes, but can further differentiate into astrocytes as well as neurons during early development as well as under pathological conditions (Richardson et al., 2011; Huang et al., 2014). NG2-glia maintain close contact to neurons, by extending their processes to nodes of Ranvier as well as keeping them in close proximity to synapses (Butt et al., 1999).

Oligodendrocytes (Figure 1) are the myelinating cells of the CNS, closely associated with neurons and astrocytes in the developing as well as the adult brain (Kettenmann and Verkhratsky, 2013) (Figure 1, cyan). Oligodendrocytes ensheathe neuronal axons (Bean, 2007), providing support and insulation, enabling rapid neuronal communication. Via gap junctions they form direct cellular contacts with other oligodendrocytes but also astrocytes (Kettenmann and Verkhratsky, 2013). Contacts with other neural cells render oligodendrocytes as important participants of cellular networks within the CNS (Kettenmann and Verkhratsky, 2013).

3.4 Astrocytes

Astrocytes (Figure 1, blue) form a vast family of glia cells, expressing a strongly brain region dependent shape and function. Fibrous astrocytes, located in the white matter, often possess vascular feet, attached to capillaries (Kettenmann and Verkhratsky, 2013). Protoplasmic astrocytes of the gray matter possess many, highly branched processes, of which at least one is bearing one or more perivascular end feet (Kettenmann and Verkhratsky, 2013). Radial astrocytes reside in the embryonic ventricular zone, but are also common in the spinal cord of lower vertebrates (Kettenmann and Verkhratsky, 2013). Bergmann Glia, derived from radial glia, occur solely within the cerebellum, maintaining close contact to Purkinje cells. Finally, Müller cells are the most prominent retinal glia cells (Kettenmann and Verkhratsky, 2013). Astrocytes are an integral part of the blood-brain-barrier by maintaining contact to endothelial cells (Matias et al., 2019) and contribute to the formation of glial scars upon traumatic brain injuries (Sofroniew, 2009). In addition, astrocytes provide nutrients to neurons and are responsible for maintaining ion and water homeostasis (Matias et al., 2019). Each astrocyte occupies and controls a distinct region, only slightly overlapping at interfaces with neighboring astrocytes (Volterra and Meldolesi, 2005). By attaching to neuronal synapses, so-called tripartite synapses are formed (Araque et al., 1999; Haydon, 2003), where astrocytes not only sense neurotransmitters, but actively participate in neuronal communication by releasing gliotransmitters, such as glutamate, ATP, GABA or D-Serine (Haydon, 2001). Most importantly, astrocytes communicate via Ca^{2+} mediated release of gliotransmitters, also modulating neuronal activity (Volterra and Meldolesi, 2005), conferring Ca^{2+} a key role not only in astroglial communication.

3.4.1 Astroglial Ca^{2+} signaling

One of the challenges in analyzing astroglial Ca^{2+} events (potentially migrating, measurable, temporary elevations of local Ca^{2+} concentration), lies in the heterogeneous nature of astrocytes themselves, reflected in the heterogeneity of astroglial Ca^{2+} events (Nimmerjahn et al., 2009; Oberheim et al., 2012; Caudal et al., 2020). Ca^{2+} events can originate from various Ca^{2+} stores within an astrocyte, but also via uptake from extracellular space through Ca^{2+} channels, triggered by diverse mechanisms. For example, inositol trisphosphate (IP_3) mediates the release of Ca^{2+} from intracellular stores like the endoplasmic reticulum (ER), resulting in large Ca^{2+} events (Brazhe et al., 2018). These large events however are infrequent, and it was shown that the majority astroglial Ca^{2+} events occur in the highly ramified astroglial processes (Bindocci et al., 2017), localized at perivascular (Shigetomi et al., 2013) as well as perisynaptic processes (Agarwal et al., 2017), forming functional microdomains (Agarwal et al., 2017). Moreover, astroglial Ca^{2+} events can express highly variable kinetics, resulting in transient

durations from less than a second (Di Castro et al., 2011) up to over one minute (Müller et al., 2021).

Astroglial Ca^{2+} events have been classified in various ways. Ca^{2+} puffs, also termed microdomain events, are elementary signals, serving autonomous functions (Smith and Parker, 2009). They are not location specific and can occur throughout the entire astrocyte. Occurring in functionally independent cellular subunits, they occupy volumes in the sub μm^3 range and cause changes in fluorescence close to noise level (Bindocci et al., 2017; Müller et al., 2021). They were found to play a fundamental role in the formation of somatic Ca^{2+} events as well as global, propagating Ca^{2+} waves (Smith and Parker, 2009). Microdomain events occur in an IP_3 independent manner and originate form mitochondria during brief openings of the mitochondrial permeability transition pore (Agarwal et al., 2017). Somatic Ca^{2+} events occur within a single cell (Hausmann, 2003) and can be classified as puffs or sparks, depending on their generating pathway (Berridge et al., 2003). Intracellular Ca^{2+} events can be transmitted to neighboring cells, independent of their generating pathway (Scemes and Giaume, 2006). Their extent is thereby governed by the effective diffusion properties of Ca^{2+} mobilizing signaling molecules inside and in between cells (Scemes and Giaume, 2006). This permits the formation and propagation of macroscopic Ca^{2+} waves extending over astroglial networks via gap-junctions and purinergic signaling in a highly synchronized and coordinated way (John et al., 1999; Haas et al., 2006). In Bergmann-Glia, Ca^{2+} waves have been classified as sparkles, bursts and flares (Nimmerjahn et al., 2009), restricted to individual fibers, radially spreading across fibers, or appearing across large networks of cells during locomotion, respectively. In addition, depending on their size, Ca^{2+} events can be termed focal events, or expanded events (Volterra et al., 2014). From a purely detection-oriented point of view, Ca^{2+} events can be termed as stationary, with virtually no change in position and only moderate changes in morphology or, non-stationary, with measurable changes in position and morphology, also known as Ca^{2+} waves.

Analyzing and understanding the "language of Ca^{2+} events" is a major step in unravelling complex regulatory functions of astrocytes, as well as the role of all glial cells in health and disease (Araque et al., 1999; Alberdi et al., 2005; Giaume et al., 2007; Caudal et al., 2020). Moreover, due to the pivotal role of astrocytes in health and disease, astroglial Ca^{2+} events are of particular interest. Reliable detection, analysis and interpretation of fluorescence events in general and astroglial Ca^{2+} events in particular however, is a non-trivial task and has been a research subject for over two decades (Cheng et al., 1999; Picht et al., 2007; Ellefsen et al., 2014; Srinivasan et al., 2015; Agarwal et al., 2017; Giovannucci et al., 2019; Wang et al., 2019).

3.4.2 Visualizing Ca²⁺ transients *in vivo*
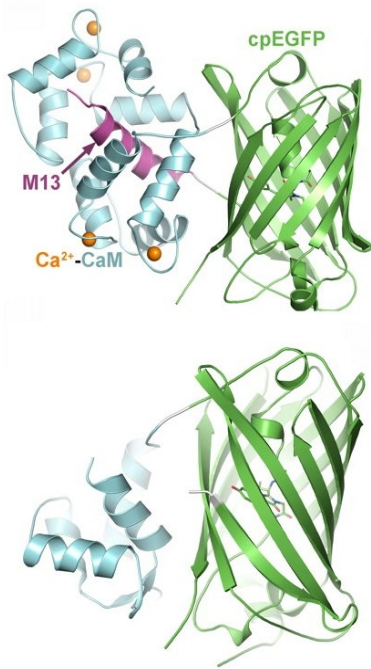
Figure 2: Structure of GCaMP.
Image credit: By Akerboom, Rivera, Guilbe, Malavé, Hernandez, Tian, Hires, Marvin, Looger, Schreiter ER - http://www.jbc.org/content/284/10/6455/F1.large.jpg, CC BY 3.0, https://commons.wikimedia.org/w/index.php?curid=15140508

Genetically encoded Ca²⁺ indicators (GECIs) can not only be expressed in a cell type and time-specific manner, but in living organisms. GCaMP (Figure 2) expresses a high Ca²⁺ affinity, consisting of a single GFP molecule, connected to the M13 fragment of myosin light chain kinase, as well as calmodulin (CaM) (Nakai et al., 2001). Ca²⁺ binding to CaM causes a conformational change due to the Ca²⁺-CaM-M13 interaction, causing a subsequent conformational change in the GFP barrel, resulting in an increased fluorescence intensity (Nakai et al., 2001). The rationale of using GCaMP as a Ca²⁺ indicator is to obtain a stronger fluorescence response with increasing Ca²⁺ concentrations. Since GCaMP is not a ratiometric fluorescence indicator one cannot deduce a specific Ca²⁺ concentration based on a given fluorescence response. Current GCaMP sensors are suspected to cause side effects, ranging from changed Ca²⁺ dynamics up to possible cytotoxicity, due to the buffering effect of CAM and incidental perturbations of signaling networks (Yang et al., 2018). These drawbacks can be overcome by novel GECIs, such as GCaMP-X (Yang et al., 2018).

3.5 Analysis of astroglial and neuronal signals

3.5.1 Analysis of fluorescence events

Reliable detection, analysis and interpretation of fluorescence events is a non-trivial task and has been a research subject for over two decades (Cheng et al., 1999; Picht et al., 2007; Ellefsen et al., 2014; Srinivasan et al., 2015; Agarwal et al., 2017; Giovannucci et al., 2019; Wang et al., 2019). Fluorescence events are classically analyzed using regions of interest (ROIs). Thereby, ROIs are meticulously placed at locations exhibiting fluorescence changes. Individual, per-ROI signals are then obtained via ROI integration. Hereby, the individual mean fluorescence per time-point is computed for any given ROI. Within each obtained ROI signal discrete transients can be extracted by detecting amplitude peaks. Recently, new approaches utilizing the analytical concept of so-called dynamic events (Wang et al., 2019; Bojarskaite et al., 2020; Müller et al., 2021) to extract and analyze non-stationary fluorescence events have been published. In contrast to classic ROIs, dynamic events are in principle not fixed in location

and can adapt to morphological changes of a fluorescence event. However, most fluorescence events, especially astroglial Ca^{2+} events are stationary (Wang et al., 2019) and exhibit only small to no changes in signal morphology and location. For this reason, classical ROI analysis remains a valid and powerful tool for their quantification. The analysis of propagating and morphing events however, is an important extension and can reveal new insights. This is especially important in the context of analyzing large scale network dynamics, as can be observed in the cerebellum (Hoogland et al., 2009) or in the context of neurodegenerative diseases, such as epilepsy (Heuser et al., 2018). Moreover, dynamic events can overcome inherent limitations of the classic approach. For example, if multiple events occur at the same location but at different time points, they likely vary in spatial extent and magnitude. Classic ROI-based analysis uses a single ROI to segment both events. Such improper segmentation in turn leads to underestimated transients in case of over-sized ROIs. Contrary, ROIs significantly smaller than the spatial extend of the actual event cause overestimation of the resulting transient. Another issue arises, if multiple fluorescence events partially overlap in space. Using stationary ROIs may result in a single event being detected as multiple transients, if a superimposed detection threshold of the neighboring ROI is overcome.

It is important to note, that neither of the above analysis paradigms automatically qualifies or disqualifies for the analysis of fluorescence events in general, and low amplitude events e.g. occurring in the gliapil or microdomain events in particular. A necessary requirement for genuine signal extraction, especially important for microdomain and other miniscule, low amplitude events, is the ability to compensate fluorescence fluctuations at basal molecule concentrations, allowing to extract fluorescence events independent of the underlying tissue structure and brain region. Moreover, this process should be independent of the level of a microscope's optical magnification as well as temporal resolution, and must work equally well in single cell and network recordings.

However, limiting factors for the analysis of fluorescence events can be the optical resolution of a microscope or the pixel sampling factor, contributing to underrepresented events in digital images. Low photon yields and insufficient signal amplification can result in low amplitude fluorescence changes being discarded as statistical noise. In combination, these factors can lead to indiscriminable, diffuse fluctuations, rendering an analysis impossible.

3.5.2 Electroencephalography
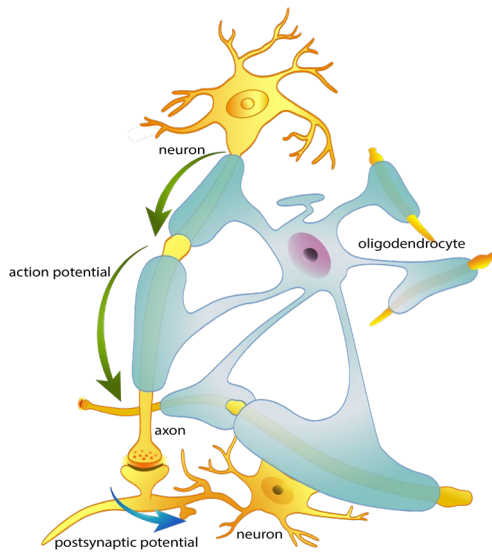
Figure 3: Action potentials and postsynaptic potentials. *Saltatory conduction of action potentials (green) along a myelinated axon from one node of Ranvier to another. Postsynaptic potentials (blue) generated at the postsynaptic terminal can spawn (or inhibit) new action potentials.*

Electroencephalography (EEG) measures potentials, reflecting electrical activity in the brain (Siuly et al., 2016) using a pair of electrodes either inside or outside the scalp (Im, 2018). The main sources of these potentials are cortical neurons (Im, 2018). There are two main types of intracellular potentials contributing to EEG signals, *action potentials* and *postsynaptic potentials* (Im, 2018) (Figure 3). Action potentials occur due to rapid changes in transmembrane resting potential, caused by changes in intracellular and extracellular ion concentrations (Bearden et al., 1980; Im, 2018). When an action potential propagates along a neuron's axon towards a synapse, a postsynaptic potential is generated across a pair of neighboring neuronal membranes (Im, 2018), via the presynaptic release of neurotransmitters. If this postsynaptic potential exceeds a certain threshold, the action potential is delivered from one neuron to another (Im, 2018). Postsynaptic potentials are believed to have a higher contribution to the generation of measurable signals (Siuly et al., 2016; Im, 2018). Although action potentials exhibit a higher signal amplitude, postsynaptic potentials last longer (~30 ms) and can thus occur synchronously over a large number of neurons (Siuly et al., 2016; Im, 2018). EEG signals can be recorded as scalp EEG, where the electrodes are attached non-invasively to the scalp surface. Alternatively, intracranial EEG records signals inside the skull. In order to avoid brain damage, brain surface electrodes can be used to record a so-called electrocorticogramm (ECoG). In the context of this thesis, EEG refers to ECoG unless specified otherwise. A brain surface electrode was developed in our lab, specifically designed for recording ECoG signals while simultaneously performing 2P-LSM in awake mice (Schweigmann et al., 2021).

EEG recordings not only help to understand normal processes and functions in the brain, but also to detect various brain pathologies. In the case of epilepsy, electrical brain activity is drastically increased during periods of hyper synchronized neuronal activity (Stevanovic, 2012).

3.5.3 Spectral analysis

Compared to advanced imaging methods used in fluorescence microscopy, EEG recordings exhibit a low spatial resolution. However, their temporal resolution is significantly higher, and signals are typically recorded at a sampling rate of 1200 Hz. This permits spectral analysis of EEG recordings, where signals are subdivided into specific wave bands (Table 1) (Drongelen, 2007). The definitions of wave bands for EEG analysis may vary however, and (Siuly et al., 2016; Im, 2018) both use slightly different bands. Some authors even specify additional sub-bands (e.g. the mu-band (μ) as an additional sub-band within the range of 8 – 12 Hz (Im, 2018)). In this thesis, the ω and γ wave bands were adapted in order to comply with recent literature (Deshpande et al., 2020). Wave-bands can be associated with different brain functions. Delta waves, for example, can be associated with deep sleep, serious brain disorders and waking state (Siuly et al., 2016). Theta waves can be related to emotional stress, but also creative inspiration and deep meditation (Siuly et al., 2016). Although it is not known if the latter two can occur in mice. It is also known, that higher frequencies are more common in abnormal brain states, such as epilepsy (Siuly et al., 2016).

Table 1: Frequency bands of EEG signals. *Frequency bands used to classify EEG activity with their respective frequency ranges.*

Band name	Frequency range
Delta (δ)	0.5 – 4 Hz
Theta (θ)	4 – 8 Hz
Alpha (α)	8 – 12 Hz
Beta (β)	12 – 30 Hz
Gamma (γ)	30 – 50 Hz
Omega (ω)	50 – 120 Hz
Rho (ρ)	120 – 250 Hz
Sigma (σ)	250 – 600 Hz

4 Aim

Automated detection and analysis of fluorescence events has been an active research topic over the past two decades. Estimation of the fluorescence signal at basal concentrations of messenger molecules is thereby a crucial step for analysing fluorescence events, laying the foundation for the analysis of low amplitude events predominantly occurring in the highly ramified processes of neuronal and glial cells. On top of that, event detection algorithms need to be sensitive enough to extract such low amplitude signals. Recently, the interplay between neurons and glial cells has moved into the focus of research, especially in the context of neurodegenerative diseases. Correlated analysis of EEG recordings in relation to molecular signalling is therefore highly intriguing, requiring the combined analysis of electrical and fluorescence signals. However, this requires the combined analysis of inherently different signals. These challenges can be met by developing new, interactive algorithms and automating computations, allowing to generate highly detailed analyses.

The aims of this thesis are 1) to devise a fully automated, unbiased, interactive and user-friendly system for the analysis of fluorescence fluctuations. 2) integrate the fluorescence analysis with EEG analysis, and 3) to thoroughly characterize fluorescence events with this application. This will require to develop:

1. Standardized, data-driven analysis routines, requiring minimal user input.
2. An adaptive algorithm to estimate the fluorescence signal at basal concentrations of messenger molecules (PBasE).
3. Algorithms, to detect and analyze macroscopic, as well as microscopic events, by
   a. Generating and analyzing stationary ROIs (CoRoDe).
   b. Tracking dynamic events and capturing their morphological changes (KalEve).
4. Methods for automatic detection, analysis, classification and statistical evaluation of transients, obtained from detected ROIs.
5. Automated documentation of analyses, results, as well as analysis parameters.
6. Analysis of EEG signals using spike-train analysis e.g. for the analysis of epileptic seizures.
7. Correlation and synchronization of EEG recordings with fluorescence events to analyze combined temporal characteristics.

These aims pose several challenges to algorithm development. In particular, the developed algorithms must not only be capable to work with arbitrary subsets of data to generate previews, but are also subject to time constraints in order to maintain interactivity. Moreover, signals recorded with fundamentally different technologies and differing spatial as well as temporal resolutions have to be brought together for a thorough combined analysis.

5 Mathematical foundations and methods

Digital signals, such as EEG recordings or images require discretization of the original (continuous) signal or image in order to be processable by a computer. One can thereby consider one-dimensional signals, such as EEG recordings, as a simplified case, compared to two-dimensional signals, such as images. In most cases it is possible to extend signal processing techniques from 1D to 2D and even to higher dimensional cases, such as image series or multi-spectral images. The discretization of n-dimensional, continuous signals is typically based on amplitude measurements of the continuous signal at a regular sampling interval T_s (resulting in the sampling frequency $F_s = \frac{1}{T_s}$), and is the basis for the digital measurement of any signal, including EEG recordings as well as digital images. The mathematical concept behind this is based on the Dirac impulse function δ. Simply speaking, δ is shifted across the continuous signal, generating measurement pulses in regular intervals, resulting in a so-called Dirac comb. At each measurement pulse, the current amplitude of the continuous signal is measured and appended to the discretized signal. In technical terms, the sampling function

$$x_s(n) = x(t)\delta_{T_s}$$

5-1

generates the n-th sample of the signal x_s as a result of the continuous signal x at time t multiplied with the Dirac function δ with sampling interval T_s. In order to discretise any signal without compromising its relevant information, the minimally required sampling rate is twice the value of the so-called Nyquist frequency, being the highest frequency to be recorded. It is derived from the sampling theorem, which states that the sampling rate must be $> 2F_{max}$ (where F_{max} is the maximum frequency of interest). This is important to reduce aliasing artefacts and distortions in the discretized signal. Amplitude changes occurring at a higher frequency than the Nyquist frequency cannot be reconstructed properly or may even be completely lost. For more details and exact derivations, the interested reader is referred to (Drongelen, 2007; Gonzalez and Woods, 2008).

5.1 Signal processing

When referring to signal processing, there is in general no restriction to the dimensionality of a given signal, and image processing can be treated as a sub-discipline of signal processing. However, for a better readability, signal processing shall refer to one-dimensional, time dependent signals, such as EEG recordings or fluorescence signals obtained by ROI integration. The concepts introduced for signal processing can in many cases be directly extended from one dimension to n-dimensions, and be adapted to apply to digital images.

5.1.1 Correlation & cross-correlation

Linear correlation quantifies the similarity, or relation between two given signals a and b. In the context of this thesis, (linear) correlation is used synonymously for the computation of Pearson's linear correlation coefficient

$$\rho(a,b) = \frac{\sum_{i=1}^{n}(a_i - \mu_a)(b_i - \mu_b)}{\left[\sum_{i=1}^{n}(a_i - \mu_a)^2 \sum_{j=1}^{n}(b_i - \mu_b)^2\right]^{1/2}},$$

<div align="right">5-2</div>

here n is the number of samples in each signal, and μ_a, μ_b are the mean values of the signals a and b, respectively. The resulting correlation coefficient ρ is in the range $[-1,1]$, where -1 indicates a negative correlation, 0 indicates no correlation and 1 indicates full positive correlation. The cross-correlation of two signals is computed by shifting one signal against the other while keeping the second signal fixed

$$P_{a,b}(m) = \mathrm{E}\{a_{n+m}b_n^*\} = \mathrm{E}\{a_n b_{n-m}^*\},$$

<div align="right">5-3</div>

where $-\infty < n < \infty$, * denotes the complex conjugate and E denotes the expected value operator.

5.1.2 Frequency analysis and Fourier transform

Any periodic function can be expressed as the sum of weighted sines and/or cosines of different frequencies, independent of the complexity of the function (Gonzalez and Woods, 2008). This sum is called the *Fourier series*. Moreover, even non-periodic functions (with a finite area under their curve) can be expressed as the integral of weighted sines and cosines (Cheng et al., 1999; Gonzalez and Woods, 2008). This formulation is known as the Fourier transform, and is defined as

$$\Im\{f(t)\} = \int_{-\infty}^{\infty} f(t)e^{-i2\pi\mu t}\, dt$$

<div align="right">5-4</div>

Where t and μ are continuous variables. Any function expressed as a Fourier series or transform can be reconstructed completely by an inverse process without loss of information (Gonzalez and Woods, 2008). Using the Fourier transform, it is possible to transfer a function or signal to the frequency (Fourier) domain. The Fourier transform of a sampled, band-limited function extending from $-\infty$ to ∞ also extends from $-\infty$ to ∞ (Gonzalez and Woods, 2008). To work with a finite set of samples, the discrete Fourier transform (DFT) is used. Computing the brute-force DFT of a signal however, comes with a significant computational burden and is practically infeasible (Gonzalez and Woods, 2008). The Fast Fourier Transform (FFT) (Cooley and Tukey, 1965) is an efficient algorithm, significantly reducing the computational overhead

of the DFT, permitting the widespread use of Fourier transform in science and engineering. For a full derivation of the Fourier Transform, DFT and FFT, refer to (Drongelen, 2007; Gonzalez and Woods, 2008).

5.1.3 Power-spectral density

The distribution of power into the frequency components of a signal is described by a signal's power spectrum. These individual frequency components can be obtained employing the Fourier transform $\Im\{f(t)\}$. The power spectral density (PSD) (of a finite total energy) can then be computed within a finite, but sufficiently large time interval, representing the spectral energy distribution per unit time. It can be computed by

$$\frac{1}{2T} \int_{-\infty}^{\infty} |f_T(t)|^2 \; dt = \frac{1}{2T} \int_{-\infty}^{\infty} |\Im(f_T)(\omega)|^2 \; d\omega, \qquad \text{5-5}$$

where $f_T(t)$ is a finite interval of the time dependent signal $f(t)$ and $\Im(f_T)(\omega)$ is the Fourier transform of the finite interval for all frequencies ω.

5.1.4 The Kalman filter

The Kalman filter (Kalman, 1960) is an iterative filter to estimate a new state of a linear, dynamic system, based on previous measurements. It explicitly models not only measurement noise, but also the uncertainty of the current system state. Kalman filters have been used to control the lunar landing of the Apollo 11 mission in 1969. Nowadays, Kalman filters find their most prominent use in GPS navigation systems (Marchthaler and Dingler, 2017), correcting measurement errors and predicting positions during temporals signal loss (e.g. when driving through a tunnel). The underlying model is based on a state space of the following form

$$S_{t+1} = AS_t + EV_t + \xi_t \qquad \text{5-6}$$

$$X_t = CS_t + \eta_t \qquad \text{5-7}$$

starting at time $t = 1$ with initial state S_1. A, C, and E are the known system matrices and V_t is the observable input process (measurement). ξ_t and η_t are latent (unobserved) noise terms. Kalman filters are considered very robust and used in a wide variety of applications, such as navigation, control systems and signal processing. The ability of a Kalman filter to predict a new system state solely based on a previous state will be used later in a predictor-corrector approach to track dynamic fluorescence events (section 6.1.3). For an in-depth introduction, further applications and mathematical derivations, refer to (Bohn and Unbehauen, 2016; Marchthaler and Dingler, 2017; Deistler and Scherrer, 2018).

5.2 Image processing

This section introduces some fundamental concepts of image processing, laying the foundation for the analysis of image sequences obtained using fluorescence microscopy, depicting temporal, localized fluorescence fluctuations. First, images and their internal structure are introduced, followed by digital filters. In addition to these essential concepts, an informal introduction to scalar field topology and scale spaces is given. All of these concepts build upon the definitions presented in section 5.1, thus images can be interpreted as multi-dimensional signals. However, some image dimensions can be treated as independent, e.g. color channels, reducing the analytical complexity.

5.2.1 Digital images

A digital image I is typically represented using a 2D rectangular grid, of which each individual pixel stores a scalar (grayscale) value and can be addressed via a pair of coordinates (x, y), specifying a row and column index.

$$\boldsymbol{p} = I(x, y). \tag{5-8}$$

Color or multi-channel images do not only store a single value per pixel, but a vector $\boldsymbol{p}$ of size n, where n is the number of recorded colors or band-limited channels. Color images are thus typically represented as 3D grids, where the 3rd coordinate specifies a color channel.

$$\boldsymbol{p} = I(x, y, c). \tag{5-9}$$

Volumetric (3D) images possess image data recorded in three spatial dimensions and can also be represented by a 3D grid, where the 3rd coordinate refers to the 3rd spatial dimension.

$$\boldsymbol{p} = I(x, y, z). \tag{5-10}$$

Moreover, scalar 2D, time-dependent data is also frequently represented as 3-dimensional data, with time in the 3rd dimension

$$\boldsymbol{p} = I(x, y, t). \tag{5-11}$$

These ambiguities however conflict with each other, and require context-sensitive knowledge by the analyst. Moreover, additional challenges are imposed when the data at hand simultaneously requires three spatial dimensions, multiple color channels and is further time-dependent. By convention, such data is typically recorded as a 5D matrix with the following order of dimensions

$$\boldsymbol{p} = I(x, y, c, z, t). \tag{5-12}$$

However, due to technical reasons, popular microscope operating software, such as ScanImage (Pologruto et al., 2003), uses a 6D representation of images

$$\boldsymbol{p} = I(x, y, c, z, s, t),$$

Where s is a slice, or position index, allowing to record multiple image slices per discrete time-step (e.g. used for image stitching). This representation of images will be used throughout this thesis. For simplicity, one usually assumes that all pixels (or voxels in case of thee spatial dimensions) are recorded instantaneously and the time to acquire a single frame is neglected.

5.2.2   Spatial filters
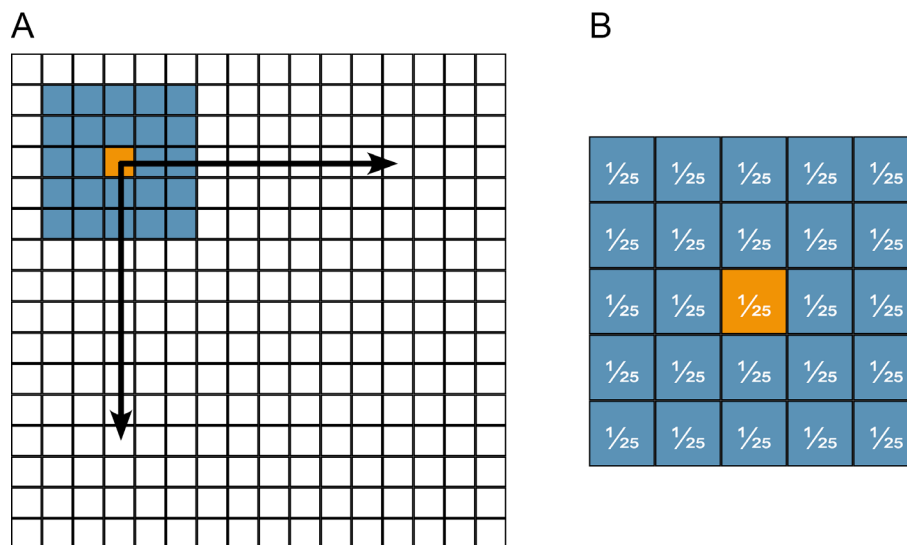
Figure 4: Image filters. *A) The filter matrix is moved across an image. Each pixel in the resulting image is replaced one-by-one by a combination of the current pixel (orange) and its neighbors (blue) based on the filter coefficients of the kernel. B) The filter matrix of the averaging filter, covering a $5x5$ neighborhood, exhibiting the same coefficients (weights) for each pixel covered by the matrix.*

Filters in image processing operate within a pixel's neighborhood (Figure 4 A). For example, an averaging or boxcar filter, computes a smoothed version of an image, by replacing each pixel's value in the result image with the average value of the neighborhood around said pixel. Since the filter is moved across all pixels (Figure 4 A), these filters are also called moving window or sliding window filters. Generally speaking, linear filters, such as an averaging filter (Figure 4 B), can be represented by a matrix H, also called filter mask or filter kernel (Figure 4 B). This matrix contains the filter coefficients and the resulting pixel values are computed as the weighted sum (linear combination) of the neighboring pixels with their corresponding coefficients.

Linear (low-pass) filters blur edges and have a dampening effect on critical points, such as local minima and maxima. Non-linear filters on the other hand can overcome this drawback.

Examples of non-linear filters are minimum, maximum or median filters, where for each pixel the minimum, maximum or median value within the filter window will be selected, respectively. To understand spatial filtering, it is important to understand two closely related concepts, correlation and convolution (Gonzalez and Woods, 2008). The process described previously, where the filter mask is moved across the image and the linear combination is computed for each pixel with its neighborhood is called correlation. From a technical point of view, convolution works in the same way, with the exception that the kernel is rotated by 180° (Gonzalez and Woods, 2008). This distinction is especially important when working with filters employing derivatives, e.g. used for edge detection. For symmetric filter kernels, such as an averaging kernel or a Gauss-kernel, correlation and convolution yield the same results.

When working with filters, it is important to consider the attenuating effect a particular filter can have on a signal. Especially if the filter kernel is larger than a given signal, various effects can arise. For example, when using a smoothing filter, signal edges are typically blurred, in addition to an attenuated amplitude. In extreme cases the entire signal can be eliminated.

Morphological filters

Morphological filters are non-linear filters, and were originally designed for binary images, where a pixel can only have one of the two values 0 or 1 (black or white). The two fundamental operations of morphological filters are erosion and dilation, typically formulated using set theory. In the context of morphological operations, the filter window is represented by a so-called structuring element, H, which is not necessarily limited to a rectangular shape. The erosion equation

$$I \ominus \mathrm{H} \equiv \left\{ p : I_p \subseteq H \right\} \qquad\qquad \textit{5-14}$$

states that an image I eroded by H is the set of all points, such that H, centered at point p is contained in I. Meaning, that a pixel p remains "white" if and only if all neighbors covered by the structuring element H, also cover "white" pixels. The dilation of I by H

$$I \oplus H \equiv \left\{ p : I_p \cap H \neq \emptyset \right\} \qquad\qquad \textit{5-15}$$

is the non-empty set of neighboring pixels, covered by H, centered at point p. Meaning, that if any one of the neighboring pixels covered by H is "white", the value of the pixel p will also be "white". Simply put, morphological erosion removes bright pixels by setting them to 0, if the filter mask in not fully inside a bright image region. Morphological dilation on the other hand expands regions of bright pixels, by setting a pixel's value to 1, as soon as the filter mask covers a single white pixel.

Alternatively, erosion and dilation can be formulated by using a minimum and maximum filter, respectively. This generalizes the concept of morphological erosion and dilation and allows their application to gray-scale images. Erosion and dilation are quasi-complementary operations, meaning that a dilation can undo the effects of a previously applied erosion and vise-versa. However, if an erosion completely removes a structure from an image, e.g. because it was smaller than the specified structuring element, this structure cannot be recovered by a subsequent dilation

$$I \circ H = (I \ominus H) \oplus H. \qquad \textit{5-16}$$

This operation can be used to remove small, isolated bright pixels (spot-noise) or to widen gaps between neighboring structured within an image. Inversely, if a dilation operation closes small holes within an image, a subsequent erosion will have no eliminating effects on these pixels

$$I \cdot H = (I \oplus H) \ominus H. \qquad \textit{5-17}$$

This can be used to expand local maxima into their neighborhood as well as to close small gaps between neighboring image structures. Due to these properties, these morphological operators are called opening and closing, respectively.

Morphological reconstruction

Morphological reconstruction is a powerful transformation, involving a marker image, a mask image and a structuring element. The marker image (F) specifies the starting points of the operation, the Mask image (G) constrains the operation and the structuring element (H) specifies the connectivity (Gonzalez and Woods, 2008). The central concepts of morphological reconstruction are geodesic dilation and geodesic erosion. Geodesic dilation of size 1 of the marker image with respect to the mask is defined as

$$D_G^{(1)}(F) = (F \oplus H) \cap G \qquad \textit{5-18}$$

where $\cap$ denotes the set intersection (Gonzalez and Woods, 2008). The geodesic dilation of size n is recursively defined as

$$D_G^{(n)}(F) = D_G^{(1)}\left[D_G^{(n-1)}(F)\right]. \qquad \textit{5-19}$$

The intersection operator ensures that the growth of the marker image F is limited by the mask image G. Geodesic erosion, can be defined analogously. Morphological reconstruction can now be realized by repeated geodesic dilation of the marker image F by the mask image G, until stability is achieved (Gonzalez and Woods, 2008). Using morphological reconstruction,

prominent maxima can be enhanced for a more robust detection while smaller, less prominent maxima are effectively removed. Thereby the structure of an image and its essential topological information are retained.

5.2.3 Scalar field topology

A scalar field $f : \mathcal{D} \to \mathbb{R}$ is a function, where usually $\mathcal{D}$ is a subset of $\mathbb{R}^2$ or $\mathbb{R}^3$, in which each point maps to a single, one dimensional value, called a scalar. In the context of this thesis, scalar fields are Euclidean and span two spatial dimensions. For example, a grayscale image is a scalar filed, where each pixel stores a single number, representing its brightness. Scalar field topology describes topological changes, which can only occur at critical points (Chazal et al., 2011b) (minima and maxima). In the context of scalar field topology, maxima are also called sources and minima are called sinks. Key to the analysis of scalar field topology is to extract *meaningful* minima and maxima, e.g. within an image. To achieve this, a given scalar field typically undergoes several iterations of simplification, in order to extract the most persistent features (Edelsbrunner et al., 2000; David and Lucioles, 2006; Chazal et al., 2011a; Bubenik, 2012; Kovacev-Nikolic et al., 2014). In the context of the analysis of fluorescence events, particular interest is paid to extracting local maxima in order to identify fluorescence events, and minimal separating lines (also called valley lines) between two adjacent maxima for segmentation.

5.2.4 Scale space
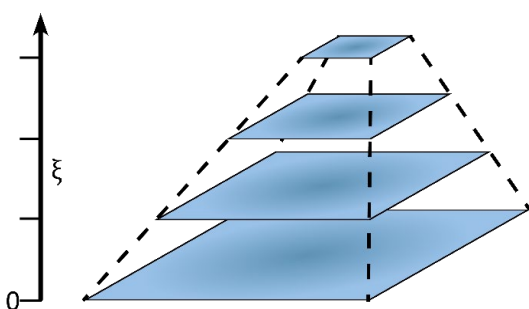
Figure 5: Image scale-space. *Scale spaces can be thought of as image pyramids where at increasing scales the amount of detail decreases.*

A scale space $f(p, \xi)$ of an image $f(p)$ is a construct, consisting of a series of images at different resolutions (scales) (Jähne, 2012), where $p \in \mathbb{R}^n$ specifies a point in the n-dimensional image f and ξ specifies the scale. Scale spaces can be computed for signals and images of any dimension, e.g. by repeated down sampling, resulting in an image pyramid (Figure 5). Another common way of computing scale-spaces is by repeated convolution of a given image with a Gaussian kernel. Two important properties of scale spaces are that with increasing scale no new details are generated (Jähne, 2012) and local extrema are not enhanced. Meaning, that the amount of detail in a higher scale is either equal or less, compared to a lower scale. Typically, one can expect a (gradual) reduction of detail, resulting in prominent image features (such as local extremal points) persisting throughout a larger range of scales, compared to smaller ones.

5.2.5 Extraction of image regions

A   B
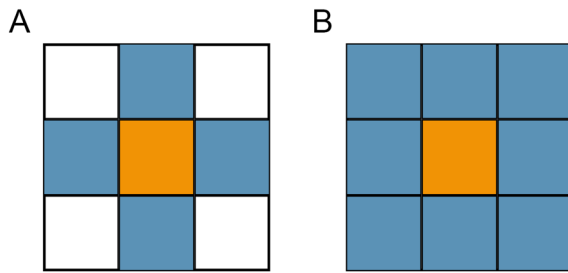
Figure 6: Types of pixel connectivity. A) 4-connectivity regards the four perpendicularly adjacent, directly neighboring pixels (blue) of the current pixel (orange). B) 8-connectivity additionally takes diagonally adjacent pixels onto account.

An image region is a group of connected pixels. The type of connectivity used to determine if two pixels are connected thereby plays a crucial role for the shape and size of the resulting region. In 2D, two common types of connectivity are used, 4- connectivity (Figure 6 A) and 8- connectivity (Figure 6 B). Using 8-connectivity permits region finding algorithms to detect groups of pixels, connected via a diagonal line, having a width of only one pixel, to be belonging to the same image region. Using 4-connectivity on the other hand would result in distinct regions. In the context of this thesis, 8-connectivity is used exclusively.

Extraction of connected image regions is usually performed on binary images. In a binary image, each pixel can take one of two values, "0" or "1", representing background and foreground pixels, respectively.

Each image region ideally represents a real-world object or a part thereof within an image and allows to compute various, region specific metrics, such as average gray value, area or circumference, to name a few. In the context of this thesis, identification and extraction of connected image region plays a fundamental role in order to detect, segment and finally analyze fluorescence events.

5.3 Experimental mice

For Ca^{2+} imaging experiments conducted in Homburg, mice were kept and bred in strict accordance with the recommendations to European and German guidelines for the welfare of experimental animals. Animal experiments were approved by the Saarland state's "Landesamt für Gesundheit und Verbraucherschutz" in Saarbrücken/Germany (veterinary licenses: 71/2013, 36/2016, 08/2021).

Na^{+} imaging experiments conducted in Düsseldorf, Germany, were carried out in accordance with the institutional guidelines of the Heinrich Heine University Düsseldorf, and the European Community Council Directive (86/609/EEC). All experiments were approved by the Animal Welfare Office at the Animal Care and Use Facility of the Heinrich Heine University Düsseldorf (institutional act number: O52/05).

Imaging sessions were performed at 8-10 weeks of age.

5.3.1 Ca^{2+} indicator mice

A
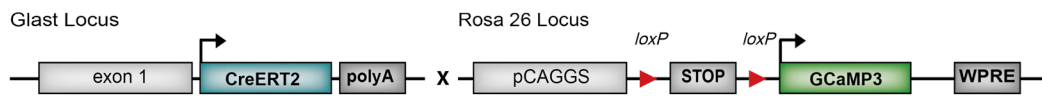
B
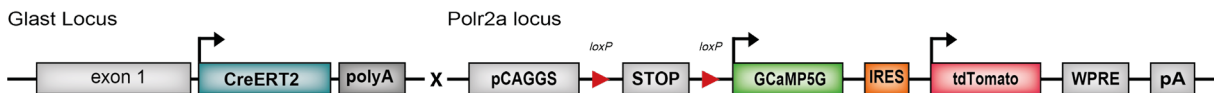
Figure 7: Mouse constructs. *Schematic construct of tamoxifen inducible astroglial expression of (A) GCaMP3 (Rosa 26 locus) and (B) GCaMP5G (Polr2a locus), additionally tagged with an IRES tdTomato for cell detection.*

The astrocyte-specific knockin line GLAST-CreERT2 (Slc1a3tm1(cre/ERT2)Mgoe, MGI:3830051) (Mori et al., 2006) was crossbred to Rosa26 reporter mice with GCaMP3 expression (Gt(ROSA)26Sortm1(CAG-GCaMP3)Dbe, MGI: 5659933 (Paukert et al., 2014) (Figure 7 A) or to Polr2a-based GCaMP5G reporter mice, additionally tagged with an IRES-tdTomato construct (Gee et al., 2014) (Figure 7 B).

5.4   Surgeries
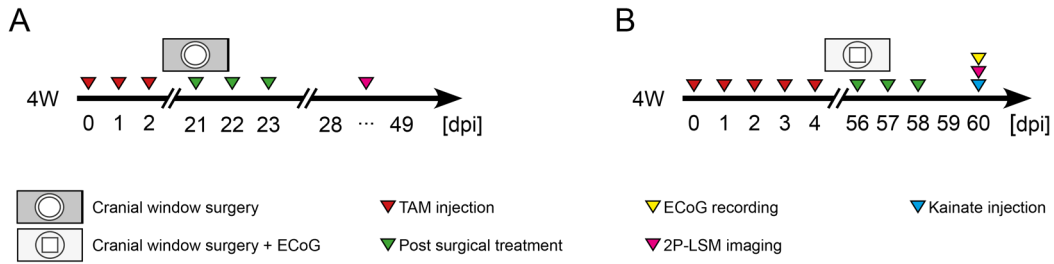
Figure 8: Scheme of experimental plan. *A) Experimental design of standard cranial window surgery. B) Experimental design of cranial window surgery in combination with ECoG brain surface electrode implantation.*

During all surgical procedures, animals were kept on heating pads and eyes were covered with Bepanthen eye ointment (Bayer, Leverkusen, Germany). Prior to surgery, instruments were sterilized using a hot bead sterilizer (FST GmbH, Heidelberg, Germany). Antiseptic povidone iodine solution (Betaisodona, Mundipharma GmbH, Frankfurt am Main, Germany) was applied at and around the incision site. Anesthesia was induced with a mixture of 5 % isoflurane, 47.5 % O_2 (0.6 l/min) and 47.5 % N_2O (0.4 l/min) and maintained with 2 % isoflurane (Harvard Apparatus anesthetic vaporizer). Buprenorphine (0.1 mg/kg, s.c.) was administered as analgetic, in conjunction with dexamethasone (0.2 mg/kg, i.p.) as anti-inflammatory treatment, except for kainate injections. Buprenorphine and dexamethasone were administered in addition to tramadol hydrochloride (Grünenthal GmbH, Stolberg, Germany) in the drinking water (100 mg/ 200 ml) for three days, including the day of surgery (Figure 8). After surgery, the animals were kept on a heating pad until complete recovery.

5.4.1   Tamoxifen treatment

For standard craniotomy (section 5.4.2) and subsequent imaging of GCaMP3 and GCaMP5 mice, tamoxifen (TAM, Carbolution, Neunkirchen, Germany) was administered in three consecutive intraperitoneal injections (100 mg/kg), one per day (Jahn et al., 2018) (Figure 8 A), with 10 µg/mL Tamoxifen in Mygliol®812 (Caesar and Lorentz GmbH, Hilden, Germany). For craniotomies in combination with implantation of an brain surface electrode, TAM was administered on five consecutive days (Figure 8 B).

5.4.2   Cranial window surgery for *in vivo* two-photon imaging

A standard craniotomy (Cupido et al., 2014) of 3 mm in diameter was performed over the somatosensory cortex (2 mm posterior and 1.5 mm lateral to bregma). The craniotomy was sealed with a glass coverslip (Glaswarenfabrik Karl Hecht, #1.5 thickness code) and fixed with dental cement (RelyX®, 3M ESPE). A custom metal holder, having a cylindrical hole (5 mm diameter) was fixed to the skull using dental cement (Figure 9). Five to seven days post surgery the first imaging session was performed (Figure 8). Cranial window surgeries were performed by Laura C. Caudal.

5.4.3   Intracortical kainate injection

Mice were placed in the stereotaxic frame (Robot stereotaxic, Neurostar, Tübingen, Germany) and injected with 70 nl of a 20 mM solution of kainate (Tocris, Wiesbaden-Nordenstadt, Germany) in 0.9 % NaCl, above the dorsal hippocampus (AP: -1.9 mm, ML: -1.5 mm at a depth of 1.3 mm from the skull surface, adapted by Laura C. Caudal from (Bedner et al., 2015)). Kainate was injected at a rate of 70 nl/ min with a 10 µl Nanofil syringe (34 GA blunt needle, World Precision Instruments, Sarasota, FL, USA). The syringe was kept in place for 2 minutes after the injection was completed, to avoid liquid reflux. The wound was closed by simple interrupted sutures (non-absorbable, FST GmbH, Heidelberg, Germany). Combined Ca^{2+} imaging and ECoG recording was conducted during the acute phase of induced epilepsy, immediately after kainate injection (Figure 8 B). Kainate injections were performed by Laura C. Caudal.

5.4.4   ECoG-electrode implant for combined *in vivo* 2P-LSM

After exposing the skull, a custom-made holder for head restraining was applied and fixed with dental cement (RelyX®, 3M ESPE). Then, a standard craniotomy (4 mm in diameter) (Cupido et al., 2014; Kislin et al., 2014) was performed over the somatosensory cortex (3.4 mm posterior to bregma and mediolateral 1.5 mm) and the surface electrode was placed on the dura mater before applying the glass coverslip (#1.5 thickness code, Glaswarenfabrik Karl Hecht, Sondheim vor der Rhön, Germany). The ground electrode (platinum wire) was placed centred on the cerebellum through a hole in the skull. Finally, all components were fixed with dental cement. Five days after electrode implantation animals were injected with kainate (Figure 8). Surgeries were performed by Laura C. Caudal.

5.5   Data acquisition

5.5.1   Two-photon excitation laser scanning microscopy (2P-LSM)

In vivo 2P-LSM (Figure 9) was performed using a custom-built four-channel microscope equipped with a resonant scanner (RESSCAN-MOM, Sutter instrument) and a 20x water-immersion objective (W Plan-Apochromat 20x/1.0 DIC D=0.17 M27; Zeiss). Scanning and image acquisition were controlled by ScanImage (SI 5.6R1) (Pologruto et al., 2003) at a frame rate of 30 Hz. Frame-averaging over 10 frames was applied to increase imaging quality, resulting in an effective acquisition rate of 3 Hz. Each FOV covered an area of 256x256 µm, sampled with 512x512 pixels (0.5 µm/pixel). Laser power was controlled using a Pockels cell (Conopticx 350-80). Excitation laser power, incident to the tissue,

Figure 9: 2P-LSM schema. Near infrared light is used for fluorescence excitation. Emitted light from fluorescently labeled cells is deflected, bandpass filtered and then detected by PMTs.

was kept between 30 - 40 mW to maintain a sufficient signal-to-noise ratio, and simultaneously minimize phototoxic effects. Excitation laser wavelength was set to 890 nm (Chameleon Ultra II, Ti:Sapphire Laser, Coherent). Emitted fluorescence light was detected by a photomultiplier tube (PMT, R6357, Hamamatsu) (Cupido et al., 2014) and pre-amplified (DHPCA-100, Femto). Digitizer (NI-5734) and control hardware (NI-6341) were housed in a NI PXIe (1082) chassis, connected to a control-PC via a high bandwidth PXIe-PCIe8398 interface. Animals were imaged 21 days post tamoxifen induced recombination.

5.5.2   *In vivo* 2P-LSM Ca^{2+} imaging

In preparation for Ca^{2+} imaging, animals were habituated before the first imaging session according to adapted protocols without water restriction (Guo et al., 2014; Kislin et al., 2014). Animals were imaged at 8 to 10 weeks of age, at least 21 days after tamoxifen induced recombination. Animals were head-fixed with a custom-designed head-restrainer, 3D-printed using stainless steel. During imaging, anesthesia was applied using a custom-made, magnetically attachable anesthesia mask. Each field of view (FOV) was imaged twice: first in anesthetized, then in awake state. During imaging in anesthetized state, isoflurane concentration was kept at 1.5 %, and flow of O_2 and N_2O was set to 0.6 l/min and 0.4 l/min, respectively. Before awake state imaging, isoflurane and other gases were switched off and it

was verified that the animals were fully awake. The selected FOVs for Ca^{2+} imaging were located in the somatosensory cortex, 80 – 100 µm beneath the dura. Each FOV was imaged for 5 minutes per condition to investigate the Ca^{2+} events. The total duration of one imaging session ranged between 30-60 minutes per animal. During and after imaging, animals were kept on a heating pad at 37°C until they recovered completely from anesthesia, additionally Fresubin (Fresenius Kabi GmbH) was provided *ad libitum* as a high caloric and high protein food supplement.

5.5.3 *In vivo* 2P-LSM imaging synchronized with ECoG recording

Images were acquired on a custom made 2P-LSM setup with a mode-locked Ti:sapphire laser (Vision II, Coherent) using ScanImage. The excitation wavelength of the laser was tuned to 890 nm and a 20x water-immersion objective (W Plan-Apochromat 20x/1.0 DIC D=0.17; Zeiss, Jena, Germany) was used. Signals were recorded by photomultiplier tubes (PMT) H10770PB-40 (Hamamatsu). Images were acquired with a frame rate of 3.3 Hz at a laser power of 30 - 50 mW (exiting the objective). Each FOV consisted of a single focal plane for Ca^{2+}-imaging and were chosen 256 µm x 192 µm (512 x 384 px), at a depth of 50-100 µm (from the dura mater). The ECoG recording system consisted of a 16-channel biosignal amplifier (g.USBamp, gTec) and a custom-made recording software, written in Matlab / Simulink, (Schweigmann et al., 2021). ECoG signals were acquired at a sampling rate of 1.2 kHz. Raw signals (with exception of the synchronization signals) were filtered with a band pass filter of 0.5 Hz to 250 Hz and a notch filter of 50 Hz. An additional preamplifier (g.HEADstage, gTec) was used to avoid input saturation of the bio-signal amplifier. In combined experiments with *in vivo* 2P-LSM, one input channel was used to acquire synchronization signals (scanning mirror deflections). Imaging sessions with ECoG recording took place within 30 min and 2 h post kainate injection.

5.5.4 Wide-field *in situ* Na⁺ imaging

Balb/c mice aged between postnatal day (P) 14-18, were anaesthetized using CO_2 before being quickly decapitated and 250 µm hippocampal slices were prepared (Karus et al., 2015b; Felix et al., 2019). Slices were transferred into an experimental bath, continuously perfused with standard, CO_2/HCO_3^--buffered artificial cerebrospinal fluid (ACSF) and their CA1 region bolus-stained with the Na⁺ sensitive dye SBFI-AM (sodium-binding benzofuran isophthalate-acetoxymethyl ester; Invitrogen, Karlsruhe, Germany) (Karus et al., 2015b; Felix et al., 2019). SBFI was alternatingly excited at 340/380 nm and emissions > 440nm were imaged with 0.5 Hz from defined ROIs reflecting cell bodies of CA1 pyramidal neurons. Changes in SBFI ratio were transferred into changes in intracellular Na⁺ concentration based on *in situ* calibrations

(Karus et al., 2015b; Felix et al., 2019). Recurrent network activity was induced via perfusion with an ACSF lacking Mg^{2+} and containing 10 µM bicuculline, in order to remove the Mg^{2+} block from NMDA receptors, and to prevent $GABA_A$ receptor activation respectively (Karus et al., 2015b). Na+ data were recorded and analyzed by Lisa Felix and Katherina Everaerts.

5.6 Statistical analysis and figures

Statistical analysis of computed data was conducted using GraphPad Prism 8. D'Agostino-Pearson normality test was used to investigate whether the obtained transient and event properties were normally, log-normally or otherwise distributed. For non- (log-) normally distributed data median values, with their associated ranges, inter quartile ranges and percentiles were used for statistical evaluation, instead of mean values and their corresponding standard deviations. Analogous, statistical significances were computed using the Mann-Whitney test for individual, or Kruskal-Wallis test for multiple comparisons, as non-parametric tests, suitable for non-normal distributions.

Figures were arranged using Adobe InDesign 2020, Adobe Illustrator 2020 and GraphPad Prism 8. Graphs, trace plots, kymographs, and ROI maps were directly exported from MSparkles. Additional ROI maps were extracted from the respective Ca^{2+} analysis tools.

6 Results

6.1 An automated system to analyze fluorescence events

Automated investigation of fluorescence events, in particular astroglial Ca^{2+} events recorded *in vivo*, poses several challenges, impeding the extraction of events as well as subsequent transient analysis. Spatially and temporally varying levels of fluorescence at basal concentrations of messenger molecules (F_0) as well as spatially overlapping events are thereby among the most common. In addition, propagating waves as they can occur during macroscopic astroglial Ca^{2+} events cannot be adequately represented by stationary regions of interest. Following, three algorithms (PBasE, CoRoDe and KalEve) are presented to solve these challenges. In addition, an amplitude-based classification method for extracted fluorescence transients is presented. Finally, a metric to assess the synchronicity of fluorescence events is introduced, enabling the correlation of fluorescence events with other, simultaneously measured signals, such as EEG.

6.1.1 F_0-estimation with PBasE

Proper estimation of the fluorescence signal at basal concentrations of messenger molecules (F_0) using non-ratiometric dyes is essential for genuine event extraction and analysis (O'Carroll et al., 2020). However, during *in vivo* imaging, especially when performing long-term imaging, basal fluorescence levels can vary for several reasons, such as dye bleaching, phototoxicity or dilating and constricting blood vessels. Additionally, when using water immersion objectives, water leakage, e.g. due to animal motion can cause a steadily progressing loss of the fluorescence signal. These variations do not necessarily occur homogeneously throughout the FOV. Therefore, a per-pixel estimate of F_0 is necessary. Among several background estimation methods, fitting of a low-order polynomial before and after the occurrence of a transient was found to generate accurate results (Balkenius et al., 2015). Recently, an adaptive algorithm to automatically estimate F_0 was introduced (Müller et al., 2021), and verified to be a valid alternative to a reference signal, F_R (e.g. cytosolic expression of tdTomato), recorded in a second fluorescence channel. Adaptive approaches based on biophysical principles (Balkenius et al., 2015; Müller et al., 2021) allow to reveal the time profile of fluorescence changes (Müller et al., 2021), and make it possible to reliably detect even low amplitude events close to noise level. Unfortunately, it is not clear if the former approach (Balkenius et al., 2015) performs automated transient detection. The latter approach (Müller et al., 2021) has the shortcoming to be not well suited for preserving very slow and long-lasting fluorescence changes not considered as basal background and thus underestimates such transients (Müller

et al., 2021). Here, the PBasE (**P**olynomial **Bas**eline **E**stimation) algorithm for automated F_0 estimation is presented to overcome these shortcomings. It is able to preserve slowly progressing and long-lasting fluorescence fluctuations. In addition, it is designed for long-term recordings (> 5 – 10 minutes), recorded at high frame rates (> 3-10 Hz).

PBasE operates solely along a pixel's temporal axis and is independent of the number of spatial dimensions. It interprets each pixel's temporal profile as individual signal and is equally well suited for 2D and 3D time-dependent datasets. To obtain F_0, the presented algorithm performs three consecutive steps, signal cleanup, simplification and finally fitting of a polynomial curve.

Signal cleanup and simplification

For an accurate F_0 estimation, potential transients need to be excluded from a signal. Moreover, special care has to be taken to avoid artificial oscillations of the fitted polynomial near the beginning and end of the signal, especially when higher order polynomials are fitted. Further, optional F_0-masking (Balkenius et al., 2015) allows to exclude pixels with no or little fluorescence activity, regarded as noise.

Signal clean-up and simplification of the pre-processed signal are performed prior to fitting a polynomial (Figure 21 A). Signal clean-up removes statistically large peaks (transients), and is implemented in two variants, a temporal mean filter (Figure 21 A, B, red line), operating on the entirety of a pixel's signal, and a Hampel filter (Hampel, 1974) (Figure 21 A, B, yellow line) as sliding window analogue. The temporal mean filter computes the mean value µ and the corresponding standard deviation σ over a pixel's entire fluorescence profile. Then, all values $> \mu + n\sigma$ are eliminated, where n is a user-definable factor. To obtain refined results, this process can be repeated multiple times. Please note, that only values $> \mu + n\sigma$ are removed and not $< \mu - n\sigma$. The rationale behind this is that typically fluorescence events cause an increase in measured fluorescence. However, decreases in measured fluorescence can not only occur due to reduced basal molecule concentrations, but are often related to (technical) issues, e.g. dye depletion or leaking water. It is thus desirable to preserve and incorporate decreases in basal fluorescence into the computed F_0 baseline.

The Hampel filter, utilizing a sliding window approach, computes the median m with corresponding standard deviation σ of the values inside the filter window, and then rejects all values $> m + n\sigma$. The Hampel filter typically follows a given signal very closely (Figure 21 A, B, yellow line), which is desirable in some cases and closely resembles the behavior published before (Müller et al., 2021). Therefore, the Hampel filter can eliminate long lasting and slow transients by incorporating them into the computed F_0 baseline. This is especially true if the

transients are much wider than the filter window. The temporal mean filter on the other hand can be parameterized to preserve these slow transients (Figure 21 B). Both methods return similar results, if only small and short-lived fluctuations in basal fluorescence are present.

To avoid high frequency oscillations of the fitted polynomial, especially near the beginning and the end of a signal, a simplified guidance signal is computed. Simplification is achieved by coarse approximation using piece-wise constant functions. Therefore, a scale space with k piecewise constant approximations, each containing 2^k sections, where $k \in [1..n]$ is computed. Each constant section is computed as the local mean value of the interval $[(k-1) * \frac{T}{2^k} + 1, \ k * \frac{T}{2^k}]$, where T is the number of recorded time points. The final guidance signal can then be optimized with respect to local minima, maxima, or minimal error to the cleaned-up signal.

F_0 estimation by polynomial fitting

After signal cleanup and simplification, a polynomial curve of user-definable degree n is fitted to each pixel's guidance signal in a least squares sense. For each pixel, this requires to solve a linear system of equations of the following form

$$\begin{bmatrix} y_1 \\ y_2 \\ \vdots \\ y_m \end{bmatrix} = \begin{bmatrix} 1 & x_1 & x_1^2 & \cdots & x_1^{n-1} \\ 1 & x_2 & x_2^2 & \cdots & x_2^{n-1} \\ \vdots & \vdots & \vdots & \ddots & \vdots \\ 1 & x_m & x_m^2 & \cdots & x_m^{n-1} \end{bmatrix} \begin{bmatrix} a_0 \\ a_1 \\ \vdots \\ a_n \end{bmatrix},$$ 6-1

where m is the number of recorded time-points per pixel. In matrix notation, this simplifies to

$$y = Xa$$ 6-2

Where y is the vector of m sample points, given by the guidance signal. X is a $m \times n$ Vandermonde matrix, with m as the number of samples in y and n as the degree of the polynomial to be fitted, and a is the vector of polynomial coefficients to be computed. To obtain the vector a of polynomial coefficients, this system can be solved by premultiplying the transpose X^T

$$X^T y = X^T X a$$ 6-3

which can be solved by

$$(X^T X)^{-1} X^T y = a$$ 6-4

Using the polynomial coefficients in a, the F_0 signal is obtained by generating the corresponding polynomial curve, matching the length and number of samples of the original dataset (Figure 21 A, B).

F_0-masking

Normalizing and detrending a dataset by computing $\Delta F/F_0$ may cause artificially amplified artifacts in dark, noisy image regions with no fluorescence activity. Independent of the method used to estimate the basal background, values $1 > F_0 \geq 0$ can occur. Which is likely to amplify noise and lead to the detection of false-positive events, ultimately resulting in the detection of false transients. This issue is solved by F_0-masking, similar to (Balkenius et al., 2015). The F_0 mask (Figure 21 E, F) is computed based on the fluorescence range of the pre-processed image stack F (Figure 21 C, D) by applying a minimal, user-definable threshold. An initial threshold value is estimated using Otsu's method, instead of using a fixed percentile as in (Balkenius et al., 2015). Pixels (with their respective time-course) covered by the F_0-mask are excluded from the F_0 estimation and set to their respective pre-processed time-course. This ensures that for all pixels, covered by the exclusion mask

$$F = F_0 \qquad\qquad\qquad \textit{6-5}$$

thus

$$\Delta F = F - F_0 = 0 \qquad\qquad\qquad \textit{6-6}$$

resulting in

$$\frac{\Delta F}{F_0} = 0 \qquad\qquad\qquad \textit{6-7}$$

for any non-zero value of F_0, effectively preventing the detection of false events and subsequent false transients. A side effect of this technique results in a linear speedup of the F_0 computation, corresponding to the percentage of excluded pixels.

6.1.2 Detection of fluorescence events

Detection and analysis of fluorescence events is key to analyzing the complex signaling patterns of Ca^{2+} as well as other important messenger molecules and ions. Proper F_0 estimation facilitates the extraction of fluorescence events, by effectively removing tissue structures and compensating fluctuations in basal fluorescence levels. Nevertheless, accurate extraction of events remains challenging not only due to the heterogeneity of fluorescence events, especially astroglial Ca^{2+} events, but also due to persisting artefacts and perturbations. Moreover, spatial and temporal proximity in combination with possible overlap pose substantial challenges to event detection and segmentation. Here, a simplified model of fluorescence events is introduced (Figure 10), based on astroglial Ca^{2+} events, visualized using GCaMP3. In addition, two automated algorithms to detect fluorescence events are presented. CoRoDe (**Co**rrelation-based **RO**I **De**tector) to extract stationary ROIs, and KalEve (**Kal**man filter based **Eve**nt detection and tracking) to extract and track dynamic events.

6.1.2.1 Model of fluorescence events, based on cytosolic GCaMP3
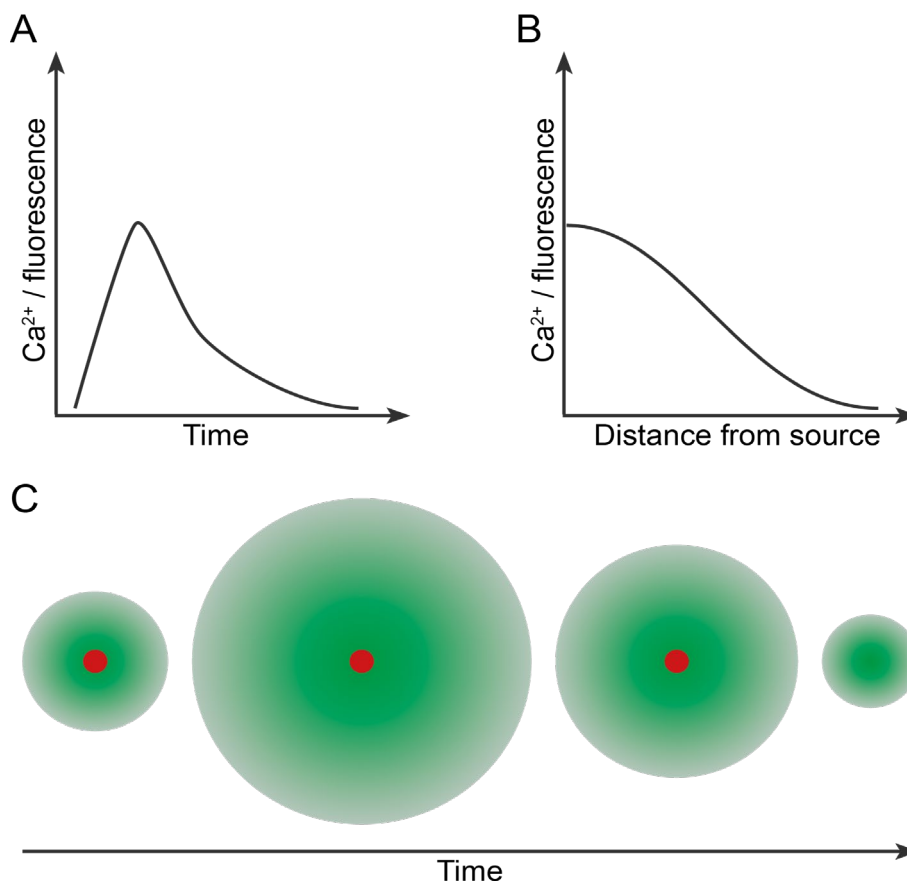
Figure 10: Simplified model of astroglial Ca^{2+} signal. *(A) Temporal profile of a characteristic astroglial Ca^{2+} event, with rapid increase in fluorescence and subsequent, slower decrease. (B) Fluorescence intensity decays with increasing distance from the Ca^{2+} source. (C) Four discrete time points depicting the spatial evolution of a Ca^{2+} event, with marked active Ca^{2+} source (red circle). Gradient indicates decreasing Ca^{2+} concentration with increasing distance from source.*

A general model for fluorescence events originating from molecular signalling is derived, based on astroglial Ca^{2+} events, visualized using cytosolic GCaMP3. Assuming a homogeneous distribution of GCaMP3 throughout the cytosol, one can expect an increase of fluorescence with increasing Ca^{2+} concentration, up to the saturating point of the available GCaMP3. Buffering effects of fluorescent dyes are neglected in this model. When intracellular Ca^{2+} levels rise, Ca^{2+} can bind to free GCaMP3 molecules, causing a conformational change, ultimately resulting in increased fluorescence. More Ca^{2+} entering intracellular space and binding to free GCaMP3 molecules further increases the fluorescence response (Figure 10 A) up to a temporal maximum. To keep this model generally applicable, no explicit assumption about the spatial distribution of the concentration of messenger molecules and thus the resulting fluorescence levels is made. Fluorescence events are assumed to express a fluorescence peak around the source (e.g. Ca^{2+} release site from internal stores, or Ca^{2+} channels in the cell membrane). In addition, the local neighbourhood around the source, covered by the event is assumed to show temporally correlated fluorescence fluctuations. Both, the fluorescence intensity as well as the temporal correlation with respect to the source are assumed to attenuate with increasing distance from the source (Figure 10 B). Fluorescence events, in particular astroglial Ca^{2+} events typically show a characteristic rapid increase in their temporal fluorescence profile (Figure 10 A) as well as a rapid spatial extend (Figure 10 C), both followed by a slower decay (Figure 10 A, C) phase. Thus, one can define a fluorescence event as a spatiotemporal fluorescence increase exhibiting a spatial fluorescence peak around the source and a temporal fluorescence peak at the time point of maximal concentration.

Based on this definition, one could assume a simple thresholding algorithm should suffice for automated event detection. However, this approach is too naïve for most experimental scenarios, especially when applied to *in vivo* recordings obtained in awake animals. This is due to several reasons, e.g. heavy motion artefacts spanning multiple frames, causing image distortions, insufficient temporal resolution or persistent image noise due to low photon yield and other artefacts, such as varying levels of (auto) fluorescence of tissue structures, such as blood vessels. In addition, multiple astroglial Ca^{2+} events can occur simultaneously within close spatial and temporal proximity and thus overlap, requiring additional segmentation. Pure thresholding approaches are typically too simple and thus fail in these scenarios. As a further complicating factor, multi-peak events may occur, where smaller amplitude peaks sprout during the rise or decay of a dominant temporal fluorescence peak. For these reasons, a robust algorithm is required to genuinely extract and segment Ca^{2+} events in order to obtain corresponding ROIs. Depending on the research question, multi-peak events might or might not be of importance. Therefore, the explicit inclusion of a singular temporal peak is omitted for the task of event detection. The extraction and dissection of multi-peak events is implemented as an independent process and deferred to the subsequent transient analysis.

36

6.1.2.2   Automated detection of stationary events

MSparkles supports several ways to generate stationary ROIs. These include a single, global ROI covering the entire FOV, regular, customizable ROI grids, hand-drawn ROIs as well as importing ROIs previously drawn with ImageJ (Rueden et al., 2017). Global ROIs and regular ROI grids however, are not appropriate in all scenarios, since they are either too coarse, usually provide sub-optimal segmentation and do not account for the location and morphology of Ca^{2+} events. Manually drawn ROIs on the other hand require tedious work, are usually biased and depend on the experience of the analyst. For these reasons, MSparkles features a novel automated algorithm for the detection of fluorescence events in order to generate representative stationary ROIs.

The goal of automated detection is to identify regions in which fluorescence events occur by requiring minimal user input. Ideally, such an algorithm is able to perform this task faster than a human expert, detects and demarcates events more accurately and is able to detect events hardly detectable by humans. Moreover, events within close proximity need to be reasonably segmented. CoRoDe (**Co**rrelation-based **RO**I **De**tector) is a novel algorithm, explicitly utilizing temporal information to overcome the aforementioned challenges.

6.1.2.3   The CoRoDe algorithm

Event identification and segmentation are performed in two consecutive steps. First, central event regions are identified and subsequently used as seed-points for a region growing algorithm. Temporal information is thereby explicitly included in order to achieve a meaningful segmentation of proximal event regions. The driving idea behind this concept is to only group neighboring pixels to a ROI, if they exhibit a minimal amount of similarity in their temporal evolution, in addition to an activity-based threshold.

Extraction of seed points

Based on the fluorescence event model introduced in section 6.1.2.1, seed point extraction can be achieved by identifying local fluorescence maxima. In order to detect actual fluorescence changes it is desirable to be independent of the underlying cell morphology and tissue structure (Figure 11 A). This is achieved by using the background-corrected dataset $\Delta F/F_0$. Assuming sources remain spatially invariant, and considering that most fluorescent (Ca^{2+}) events are in fact stationary (Wang et al., 2019) permits the utilization of projection along the temporal axis. This not only reduces computational complexity, but also completely omits the tracking and assignment problem. Projecting the range of $\Delta F/F_0$ (Figure 11 B) provides

additional robustness against persistent perturbations and possible negative values. For each pixel p, the maximum change (range) in $\Delta F/F_0$ is computed by

$$R = \max\left(\frac{\Delta F}{F_0}(p)\right) - \min\left(\frac{\Delta F}{F_0}(p)\right),$$

<div align="right">6-8</div>

subtracting the minimal value of p from the maximum value of p. Each pixel in the range map R thus represents the maximal change it undergoes in $\Delta F/F_0$ during the recorded time period (Figure 11 B). Finally, regional maxima can be extracted from R (Figure 11 C). Using the range projection of $\Delta F/F_0$ brings practical advantages over a maximum intensity projection (Figure 36 A, B)

$$M = \max\left(\frac{\Delta F}{F_0}(p)\right).$$

<div align="right">6-9</div>

The maximum projection represents the theoretical ideal condition, and applies if, and only if

$$\min\left(\frac{\Delta F}{F_0}(p)\right) = 0,$$

<div align="right">6-10</div>

in which case M and R are identical. However, this condition is particularly difficult to achieve in experimental scenarios. Summed intensity projections (Figure 36 C, D) do not necessarily correspond to fluorescence events (Figure 11 A, B) and further tend to suppress events exhibiting a low fluorescence amplitude. This is especially true, if they are performed on the original dataset F.

A limitation of projection-based event detectors arises, if multiple events (partially) overlap during the recorded time period. These events might not be resolved properly and in some situations, they might not be detected. Overcoming this limitation requires a fundamentally different approach (see section 6.1.3). Pixels excluded by the F_0-mask are zero in R.

Segmentation of stationary regions
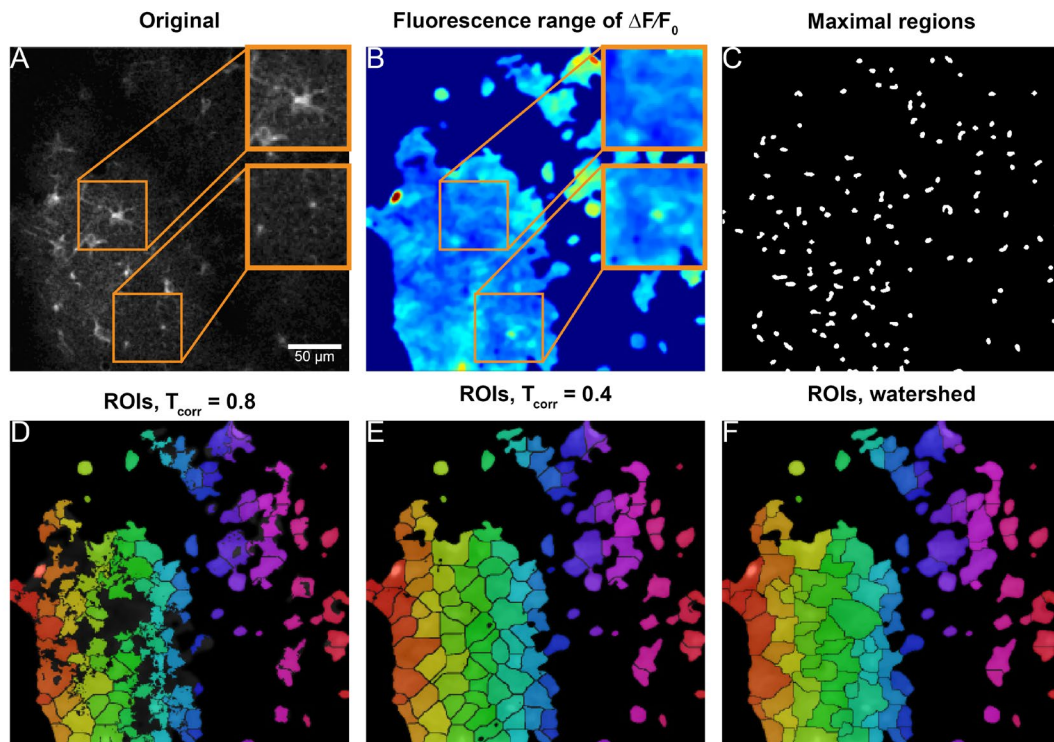
Figure 11: Automated detection of stationary ROIs. *A) The original dataset is not well suited for signal extraction and contains unwanted cell morphology. B) The fluorescence range map reveals active regions, not directly visible in the original dataset, and not necessarily located in bright somatic regions (see orange boxes). C) Regional maxima extracted from the fluorescence range form the basis for correlation-based region growing (D). Comparing the extracted ROIs, one can see that the correlation-based algorithm is able to obtain finer resolved ROI boundaries (D), compared to the watershed transform (F). E) A less stringent correlation threshold can result in ROIs similar to regions obtained with a watershed transform.*

Segmentation of ROIs can be performed by utilizing a watershed transform (Fernand, 1993). Using the range projection of $\Delta F/F_0$, R, as basis for the watershed segmentation will produce segmentation boundaries along valley lines, representing connected pixels, exhibiting a minimal range in at least one dimension. While this can lead to a reasonable segmentation in simple cases, it is subjected to two shortcomings. Watershed segmentation generally segments the entire image, requiring a subsequent, usually intensity-based, thresholding operation to limit region growth beyond a reasonable extent. Further, and more importantly, this method only relies on spatial information of the projected data, neglecting temporal information and thus a large part of the information available in any given dataset. Therefore, to the best of the author's knowledge, a novel temporal correlation-based segmentation algorithm is introduced.

Based on the detected seed points in R (Figure 11 C), simultaneous region growing is performed. A correlation threshold (t_{corr}) thereby establishes a criterion of minimally required correlation, (similarity in temporal evolution) with the temporal evolution of the initial seed point. This similarity cannot be guaranteed using a watershed transform. A secondary range threshold applied to R serves to establish a quality criterion in order to extract events exceeding

a minimal change in $\Delta F/F_0$. Temporal correlation is computed on $\Delta F/F_0$, using Pearson's linear correlation coefficient

$$\rho(s, v) = \frac{\sum_{i=1}^{n}(s_i - \mu_s)(v_i - \mu_v)}{\sqrt[2]{\sum_{i=1}^{n}(s_i - \mu_s)^2 \quad \sum_{j=1}^{n}(v_j - \mu_v)^2}}$$

6-11

where s is the averaged time course of all pixels of a given seed point, v is the time course of an adjacent pixel and μ_s and μ_v are the mean values of v and s, respectively.

To obtain the final segmentation, the seed points are simultaneously grown into their local neighborhoods of R until either the intensity threshold or the correlation threshold is violated. Pixels adjacent to more than one region are marked as boundary pixels. Decreasing the correlation threshold to zero results in region growing being governed solely by the range threshold, and the detected regions become more similar to those obtained by a watershed segmentation (Figure 11 D, E, F).

6.1.3 Automated detection and tracking of dynamic events

Analyzing fluorescence events using stationary ROIs is an important concept to gain insight into molecular signaling mechanisms. Yet, it suffers from intrinsic limitations. Especially the inability to adapt to event propagation and morphology changes prohibit the analysis of waves. In particular, when analyzing astroglial Ca^{2+} events, Ca^{2+} waves can spread not only within individual cells, but across astroglial networks, e.g. propagating through gap-junctions or along capillaries. These limitations can be overcome by dynamic event analysis. However, this poses additional challenges, such as tracking and accurate per-frame segmentation of Ca^{2+} events. Tracking needs to be robust in the presence of image distortions, such as motion artefacts and temporary brightness changes. In addition, this prohibits the extensive use of projections as it was possible for the detection of stationary ROIs, making dynamic event analysis more affective to noise and perturbations.

Once detected events need to be re-identified and tacked across multiple frames. Moreover, an already identified event might be temporarily lost. This, for example, can happen due to image distortions originating from animal motion. Events might cross-over, merge or split into two or more separate events, propagating in different directions. Following, the KalEve algorithm (**Kal**man filter based **Eve**nt tracking and segmentation) for event tracking is introduced to overcome these challenges.

6.1.3.1 The KalEve algorithm
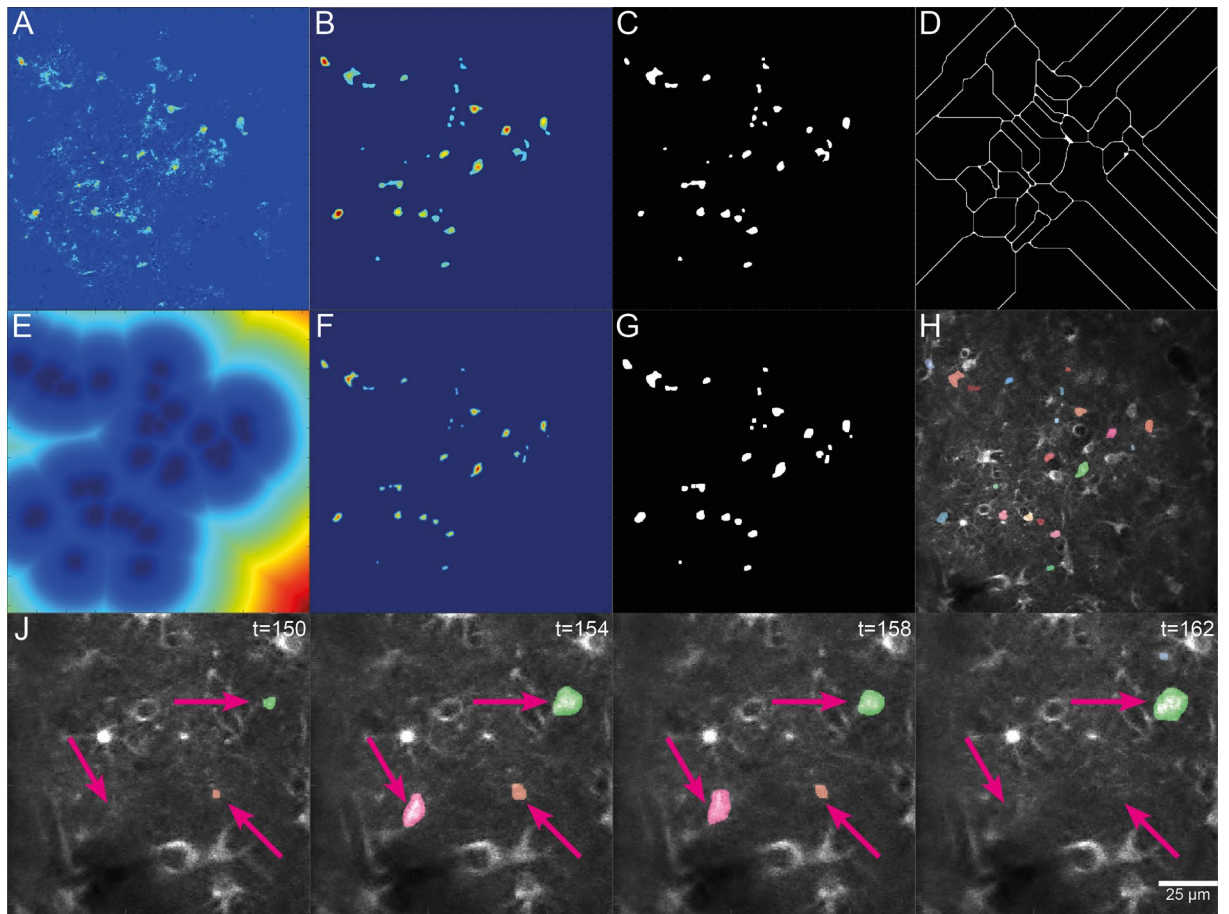
Figure 12: The KalEve algorithm. *A) Single frame as $\Delta F/F_0$, depicting fluorescence activity above background as bright spots. B) Thresholding and morphological erosion remove fluctuations not meeting specified quality parameters. C) Extracted and dilated maximal regions. D) Coarse segmentation using watershed transform. E) Distance field computation of distance to maximal region. F) Inverted distance field, weighted by $\Delta F/F_0$. G) Detected regions of connected pixels. H) Final segmented dynamic events overlayed over pre-processed image of original stack. J) Image sequence showing the evolution of dynamic events.*

Based on the definition from section 6.1.2.1, a fluorescence event can be identified on a frame-to-frame basis (Figure 12 J) by extracting local spatial maxima in $\Delta F/F_0$ (Figure 12 A-C). These maxima need to be reliably trackable, i.e. being unambiguously identified in a subsequent frame. Therefore, a Kalman filter is used to predict locations of known local maxima in a subsequent frame. This has the advantage of being robust against temporary miss detections e.g. due to motion artefacts and results in a unique track record for each individual maximum. Once the maxima and their tracks are known, segmentation is performed (Figure 12 D-H). Therefore, the maxima are first back-projected into $\Delta F/F_0$, effectively reconstructing temporarily missing maxima and allowing proper segmentation even during tracking gaps. After segmentation is completed, quality constraints ensuring a minimally required size and duration are applied.

Tracking of Ca²⁺ transients using a Kalman filter

To obtain stable and persistent local maxima across frames, a spatiotemporal Gaussian scale space $\Delta F/F_0$ (ξ) is computed. The scale ξ required to obtain satisfactory results largely depends on the quality of the dataset and is parameterized individually. Morphological reconstruction is used to expand maxima for subsequent extraction. An additional dilation operation further expands detected maxima and closes small gaps to increase detection robustness. Each maximum is individually tracked using a Kalman filter. Hereby, the Kalman filter is used to predict the new location of a known maximum in a subsequent frame. Each predicted location, called candidate location, of a maximum is then corrected, based on a corresponding detection in the succeeding image frame, using the MATLAB function `assignDetectionsToTracks`. This function solves the assignment problem, by minimizing a cost matrix, where the costs of an assignment increases with the distance of a known location to a candidate location. Since the candidate locations are predicted using a Kalman filter, they already respect knowledge about previous location and velocity of the (moving) maximum. It is thus sufficient to minimize the distance from a known to a candidate location. In case of an assignment, a track is generated, representing the trajectory of the maximum. In addition to returning assigned tracks, `assignDetectionsToTracks` also returns a list of unassigned maxima, as well as unmatched tracks. Unassigned maxima spawn new tracks, i.e. identify the beginning of a new event. Unmatched tracks are used to overcome temporary miss detection. In case of one or more failed detections, the predicted location serves as new location permitting robust tracking. If, however, a track is unassigned for too many frames, it is considered lost and terminated, marking the endpoint of an event.

Segmentation by morphological operators and weighted distance fields

Spatial segmentation of neighboring fluorescence events is carried out first coarsely and then refined to obtain the spatial extent of each event (Figure 12 D-G). To avoid a faulty segmentation, due to temporarily undetectable maxima (e.g. caused by motion artifacts), extracted maxima from the Kalman filter are back projected into the dataset. Next, a coarse segmentation is obtained by applying a watershed transform to the spatiotemporal scale-space $\Delta F/F_0$ (ξ) (Figure 12 D). This guarantees each maximum to be contained within a distinct, non-overlapping region. However, these regions are typically too large and do neither respect intensity levels in $\Delta F/F_0$ nor the previously defined threshold. Therefore, a distance transform is computed for each segmented region with respect to the regional centers, weighted by $\Delta F/F_0$ (Figure 12 E-F). This allows the segmentation of more accurate, regions of connected pixels for each detected maximum. After segmentation, region labels are assigned, based on the tracking results. In some cases, a maximum, suddenly originating within an existing region

can occur, causing a false segmentation and thus generating a new region-label. To increase coherence, sudden changes of assigned labels are suppressed by enforcing the constraint that new maxima cannot originate within an existing region of a succeeding frame. As a consequence of this rule, two consecutive Ca^{2+} events occupying the same spatial region must have a gap of at least one frame to be counted as two individual dynamic events.

6.1.4 Analysis of Ca^{2+} transients
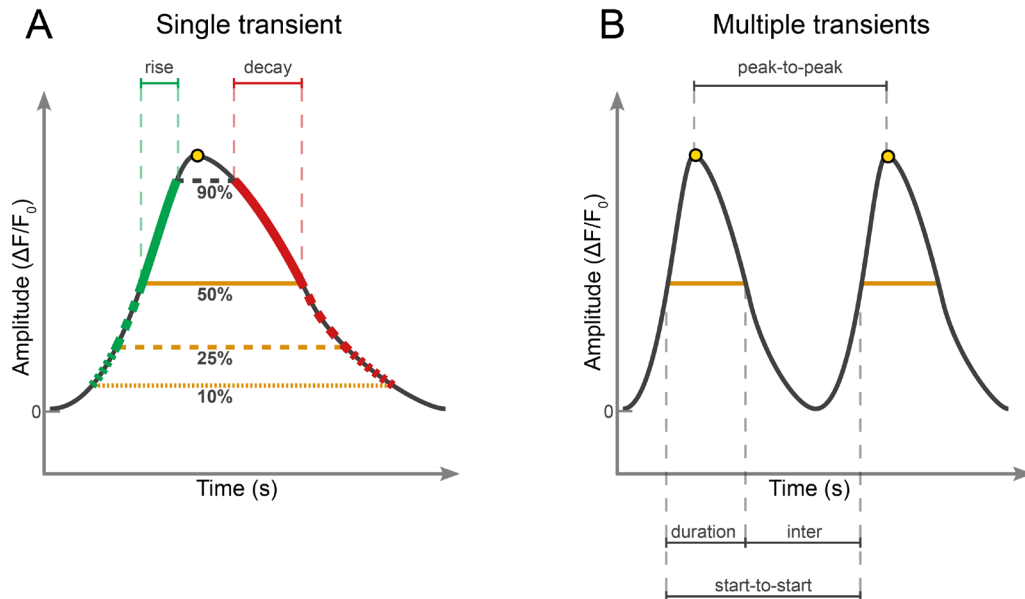
Figure 13: Properties of Ca²⁺ transients. *A) Properties of individual transients include peak amplitude (yellow dot), duration (orange lines) as well as rise (green) and decay times (red). Depending on the height reference, 50% (FWHM, orange line), 25%, or 10% (dashed orange lines), the duration, but also rise and decay times can be calculated more accurately. This however, requires a high signal quality. B) Consecutive transients allow to compute various signal timings, like peak-to-peak, inter signal and start-to-start. It is important to notice that these timings are influenced by the choice of the height reference.*
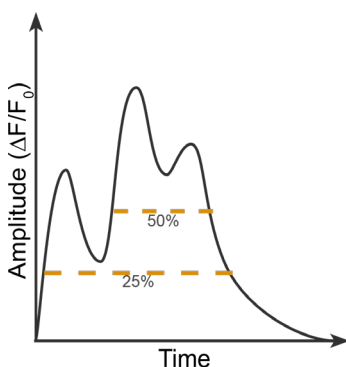
Figure 14: Multi-peak transient. *Depending on the definition of transient duration, the multi-peak transient consists of two (FWHM) or three (25%) peaks.*

Peak amplitudes, durations, rise and decay times as well as inter-transient timings between consecutive transients (Figure 13) are automatically extracted, using a customized version of MATLAB's findpeaks function. Transient duration is by default computed as the full width at half maximum (FWHM). In addition, transient duration can be computed as full width at 25% or 10% of the peak value (Figure 13 A). The latter two can lead to a much more accurate estimation of the transient duration, but set higher requirements to signal quality. Inter-transient timings (Figure 13 B) and frequencies are automatically computed for ROIs exhibiting more than one transient. Optionally sub transients can be excluded. Sub transients are local peaks of a multi-peak transient (Figure 14), i.e. amplitude peaks occurring during a stronger peak. This option

strongly depends on the percentage of the peak amplitude at which transient duration is computed. Transient rise time is computed on the rising flank of the transient as the time span between detected transient start and the first time the transient reaches 90% of its peak amplitude (Figure 13 A). Similarly, transient decay time is computed on the falling flank of the transient as the time span between the first time the transient drops to 90% of the peak amplitude and the detected end of the transient (Figure 13 A).

6.1.4.1 Peak amplitude classification

MSparkles automatically classifies extracted transients based on their peak amplitude. This classification can be performed by manually defining classification intervals. Alternatively, MSparkles can compute these classification intervals automatically, based on intrinsic properties of a given dataset. In either case, transients not exceeding the minimal classification threshold will be ignored. In addition, ROIs not exceeding this threshold at any time are considered false positives and are automatically removed.

For automatic classification, thresholds are calculated based on the overall mean (μ_{tot}) and standard deviation (σ_{tot}) of all integrated ROIs and a minimal classification threshold is determined as $\mu_{tot} + \sigma_{tot}$. Three classification intervals are defined as $[T_1 .. T_2)$, $[T_2 .. T_3)$ and $[T_3 .. \inf)$, with $T_n = \mu_{tot} + n\sigma_{tot}$. However, intrinsic statistical properties and the resulting classification intervals vary among datasets and can impede a direct comparison.

Assigned classes are used to analyze the signal composition, revealing changes in signaling behavior. Signal composition is defined as the relative frequency of transients belonging to a specific class (Figure 24 H, J). Using the signal composition can help to uncover changes in signaling behavior, independent of, but also in conjunction with the absolute number of detected transients or detected ROI sizes.

6.1.4.2 Synchronicity analysis

Astroglial networks can exhibit highly synchronized Ca^{2+} events (Nimmerjahn et al., 2009). To detect and analyze synchronous events, a synchronicity index (Figure 37 B) ranging from 0 to 1 is automatically computed as the relative frequency of the maximal area, covered by all detected events for a given time point t.

$$s(t) = \frac{1}{A_{tot}} \sum_{i=1}^{n} A_i(t) \qquad \text{6-12}$$

where A_{tot} is the total area of all detected events, projected along the temporal axes, n is the number of transients a time t and A_i is the area covered by the ith active event.

In the case of stationary ROIs, ROI area remains invariant over time and a ROI is considered active during the period between the start and end time of an identified transient, resulting in a binary on/off behavior. Thus, the computation of the synchronicity index can be simplified as the relative frequency of simultaneously active ROIs.

Peaks of the synchronicity index and their respective duration are automatically extracted. All ROIs exhibiting a fluorescence peak during the duration of a synchronous event are extracted together with their activation sequence. Activation sequences are determined, based on the starting times of affected peaks. This not only allows to identify synchronously active regions, but also the internal activation pattern and spread of a synchronous event. However, the transient duration and the percentage at which it is obtained determines the length of the period in which a ROI is considered active, and affects the correct determination of the activation sequence.

6.1.4.3 Differential analysis of fluorescence events

Differential analysis builds upon the unique ability of MSparkles to define multiple analyses per dataset, and allows to intersect two sets of ROIs. This allows to investigate different aspects of a dataset, while taking advantage of already performed pre-processing and F_0 computations. Differential analysis can be used, e.g. to analyze and compare somatic events with events in the gliapil. To achieve this, somatic regions can be hand drawn or imported from an ImageJ ROI set and subsequently be intersected with automatically detected ROIs, for example. The result of this operation are two mutually exclusive sets of ROIs which can then be analyzed independently of each other.

6.1.5 Correlated analysis of imaging data and secondary recordings

In addition to analyzing fluorescence events, MSparkles supports the analysis of correlated, multi-channel signals. Such secondary signals could be obtained by Electroencephalography (EEG), Electromyography (EMG) or Pulse oximetry, for example. The only requirement to these recordings is, that they contain a synchronization signal in a dedicated channel. Synchronization and analysis of secondary signals is demonstrated here as a proof-of-concept, by the analysis of eight-channel ECoG recordings, obtained by brain surface electrodes (Schweigmann et al., 2021). Therefore, an ECoG dataset is attached to a corresponding Ca^{2+} dataset as a subsidiary. Both datasets are synchronized, using the control signal of the galvanic mirrors of the 2P-LSM, included in the ECoG dataset as additional channel (Schweigmann et al., 2021). This sawtooth signal is emitted by ScanImage during the recording of each dataset and is obtained from the slower (y-axis) mirror as frame-trigger

signal. Amplitude peaks of the frame trigger signal demarcate the beginning of a new image frame of the fluorescence image stack. By selecting an appropriate synchronization mark, MSparkles then performs a per-frame synchronization correction to avoid potential drift between both signals.

6.1.5.1 Quantitative spike-train analysis

Spikes are short-lived, significant increases in EEG voltage. A spike train consists of a series of bursting EEG spikes, exceeding a definable voltage threshold (Figure 15), typically set well above healthy conditions. Individual spikes of a spike train occur in rapid succession, such that the time points of two consecutive spikes fall within a definable interval, $t_n - t_{n-1} < \Delta t$ (Figure 15). Spike train analysis (Figure 15) is a simple, yet powerful tool to detect hyper-synchronized pathological brain activity and plays an important role for the investigation of neuropathological diseases, such as epilepsy. Epileptiform EEG activity is thereby divided into two predominant states: ictal activity, recorded during a seizure and inter-ictal activity in between two epileptic seizures (Stevanovic, 2012). Inter-ictal activity can show isolated spikes and spike trains, sharp waves or spike-wave complexes. Ictal activity on the other hand is composed of a continuous discharge of polymorphic waveforms of variable frequency and amplitude, spike and sharp wave complexes or rhythmic hypersynchrony (Stevanovic, 2012), resulting in a massive series of spikes in rapid succession. Depending on the form of epilepsy (or neurodegenerative disease in general) different EEG wavebands may play a more important role than others. MSparkles thus provides the ability to select various sub bands and derived signals as the source for an analysis. These include wavebands from δ to σ (Table 1), as well as the signal magnitude, signal power and signal variance. The spike train detector is configured, by specifying a voltage threshold in µV, maximum Δt between two consecutive spikes, as well as a minimum spike train duration (Figure 15). Spike-train analysis is then performed for all valid EEG channels. Spike trains are automatically documented in a spreadsheet file, containing individual tables for each channel, including the starting time, duration, number of spikes and the mean spiking frequency, of each detected spike train.
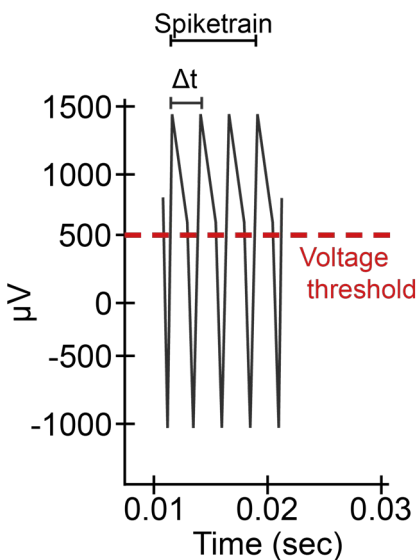
Figure 15: EEG spikes and spike-trains. *Illustration of an idealized EEG/ECoG signal, depicting four spikes, above a defined threshold level. Δt measures the interval between two consecutive spikes. A spike train must exhibit a minimum duration, and consists of multiple spikes, with intervals < Δt.*
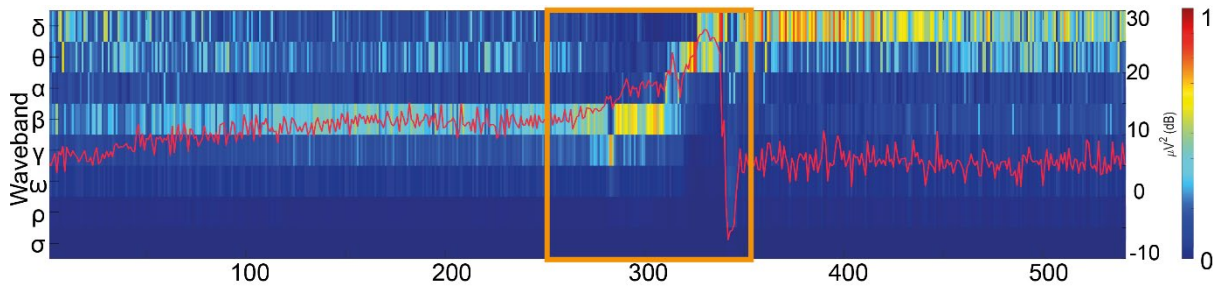
6.1.5.2 Qualitative spectral analysis

Figure 16: Power spectral density visualization. The normalized power-spectral density (PSD) shows the relative power distribution, binned to epochs of 1 second, across eight wavebands from δ to σ. Frequency bands from δ to σ are depicted with increasing frequencies from top to bottom. Actual signal power is displayed as red line in $\mu V^2 \ (dB)$. Orange box highlights progressing increase in signal power during epileptic seizure, followed by post ictal depression, resulting in a rapid drop of the signal power. Relative PSD shows the change of the predominant brain waves before and after the seizure.

In order to assist the analysis process of EEG signals, MSparkles features qualitative spectral analysis (*Figure 16*). By subdividing the original signal into the relevant EEG wavebands (Table 1) it becomes possible to discover peculiarities of neuropathological diseases, otherwise not noticeable. Once known, these distinctive features can then be implemented into an automatic detection algorithm, extending MSparkles capabilities.

The original EEG signal is first transformed from the time domain into the Fourier domain, using FFT. Next, a bandpass filter is applied to extract the components of each EEG wave-band. This foundation is used to create two distinct visualizations.

1. Waveband contribution. The components of the wavebands are transformed back to the time domain, using the inverse FFT, and then overlaid onto of the original signal, depicting individual contributions of each wave-band in contrast to the original signal.

2. Visualization of the relative power spectral density (Figure 16). The Fourier-transformed and band-filtered signal is subdivided into 1 second epochs. For each epoch, relative power-spectral density (PSD) is computed in addition to the absolute signal power. This is then used to create a heat-map, displaying the relative power distribution per wave-band and epoch (Figure 16) and absolute signal power as overlaid curve. This not only shows the relative contribution of each wave-band, but also outlines the rise in signal power, during the course of a seizure.

6.1.5.3 Cross-correlation analysis of fluorescence and EEG recordings
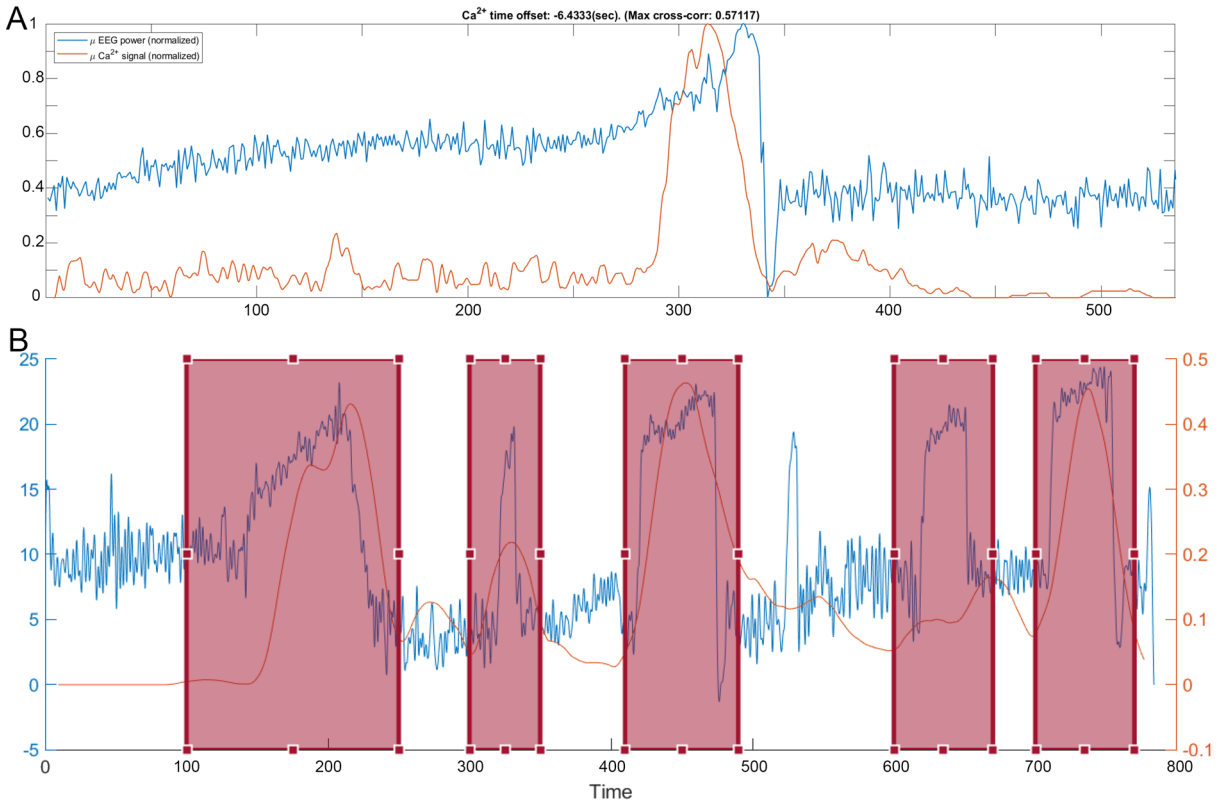
Figure 17: Ca²⁺ / EEG cross-correlation. *Cross-correlation between Ca²⁺ synchronicity (orange line) and EEG power (blue line). Both, EEG power and Ca²⁺ synchronicity exhibit distinct peaks. A) Global cross-correlation analysis determined a single peak in Ca²⁺ synchronicity about 6.4 seconds before the peak in EEG power occurs. B) advanced correlation analysis allows to specify multiple analysis intervals (red boxes). For each interval, an independent correlation analysis between Ca²⁺ synchronicity and EEG power is computed.*

Cross-correlation determines the similarity of two signals by shifting one signal relative to the other (reference signal). It can easily be applied automatically and is robust against noise. This allows to determine the point of highest correlation between the two signals and subsequently to compute the temporal shift between those signals. MSparkles uses normalized cross-correlation, producing values between -1 and 1, indicating negative or positive correlation

$$\gamma(u) = \frac{\sum_t [f(t) - \mu_f][g(t-u) - \mu_g]}{\sqrt{\sum_t [f(t) - \mu_f]^2 \sum_t [g(t-u) - \mu_t]^2}},$$

6-13

where f is the fixed signal, g is the signal being shifted along f and μ_f and μ_g are the means of f and g, respectively. A value of 0 indicates no correlation at all, while 1 indicates perfect correlation. -1 indicates perfect negative correlation, i.e. an inverse relation. Identifying the maximum correlation between two signals allows to obtain the displacement between those signals (Figure 17 A). To determine the temporal displacement, it is sufficient to compute the difference of the time of maximal correlation with the relative start of the reference signal. Additionally, the delay between the start of both recordings needs to be accounted for, by

adding this shift to the computed delay of the shifted signal. Finally, a positive cross-correlation result indicates a leading reference signal, whereas a negative value indicates a lead of the shifted signal. In MSparkles, the EEG signal or one of its derived signals, such as epoch power or a specific wave band, always serves as reference signal. By default, the reference signal is correlated with the synchronicity index of the corresponding fluorescence signals. Alternatively, the mean signal over all detected ROIs can be chosen.

In the presence of multiple hyper synchronous EEG events, accompanied by corresponding fluorescence synchronicity spikes, comparing two signals in their entirety may become inaccurate, especially when the complementary temporal displacements vary. For this reason, MSparkles features an extended fluorescence/EEG correlation analysis, allowing to specify multiple, independent analysis intervals (Figure 17 B). Within each interval, a distinct correlation analysis is performed, providing individual results.

EEG and fluorescence signals exhibit fundamentally different sampling rates (typically 600-1200 Hz and 0.5-10 Hz, respectively), mandating resampling of the fluorescence signal to match the sampling rate of the EEG recording, preserving its high temporal resolution. The EEG signal is normalized to become independent of scaling. Conversely, 2P-LSM recordings exhibit a high spatial resolution often with a single pixel covering ¼ μm^2 or less, whereas the brain surface electrodes used in this study cover an area >1 mm^2 with eight peripheral electrodes.

6.1.6 Application design

The algorithms presented above are fused together in MSparkles - an interactive, graphical application, based on MATLAB (Figure 35). A core principle underlying the application design is to provide direct visual feedback for data exploration and parameter optimization. In order to make the presented algorithms easily accessible, MSparkles implements a four-stage processing pipeline, including a freely configurable pre-processing stage. Automated export of results, as well as customizable graphs and videos facilitate result presentation.

6.1.6.1 Design of the processing pipeline
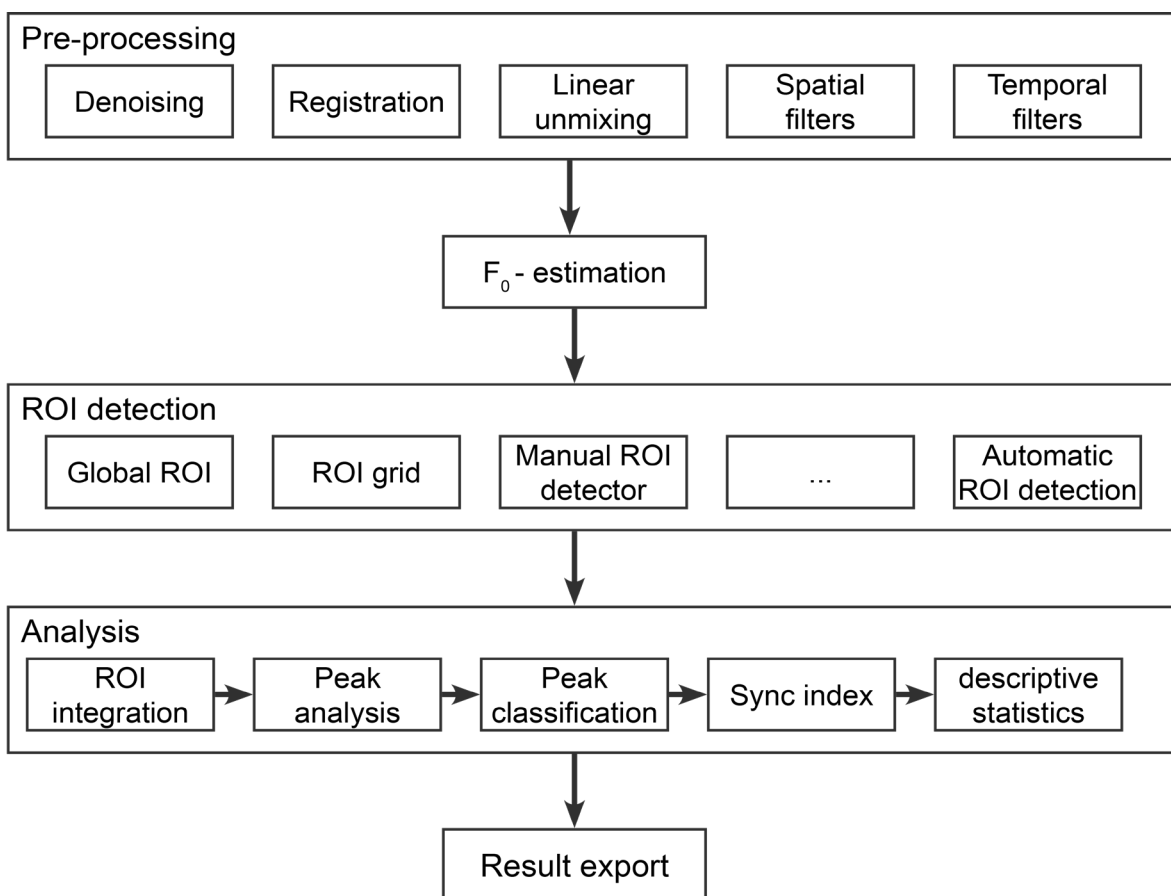
Figure 18: The processing pipeline. *The four main stages of the analysis pipeline, pre-processing, F_0 estimation, ROI detection and ROI analysis are individually configurable. Pre-processing is equipped with various, freely combinable algorithms to enhance image quality. ROI detection features various detectors which can be extended by additional detection algorithms. The analysis stage executes a series of consecutive tasks to extract and analyze individual transients. Finally, automatic result export generates graphs, PDF reports and spreadsheets for further analysis and documentation purposes.*

In order to reduce unnecessary computations, MSparkles features a modular processing pipeline, consisting of four consecutive, but individually executable stages. Each stage (pre-processing, F_0 -estimation, ROI detection and transient analysis) (Figure 18) is configured individually via a specialized graphical editor (Figure 35 B, C, D). The processing pipeline is dynamically compiled at run-time. Prior to each (partial) execution of the pipeline, it is

automatically determined if required preceding computations have already been carried out and can thus be omitted. If required computations are missing, they are automatically inserted at the appropriate position in the pipeline. The processing pipeline can be configured to execute all computations up to a specific stage (e.g. F_0-estimation), execute an individual stage or process an entire dataset at once. In addition, batch-processing of multiple datasets as well as entire folder structures is natively supported. To avoid unnecessary access to the (network) filesystem, the processing pipeline operates on a per-dataset basis, meaning that all computations concerning an individual dataset are carried out before continuing to the next.

6.1.6.2 Pre-processing

Data acquired using 2P-LSM is often degraded by various kinds of noise and other perturbations. Especially *in vivo* data obtained from awake animals is typically perturbed by motion artifacts and image drift. MSparkles therefore provides a customizable and freely configurable pre-processing pipeline. It provides algorithms for denoising (SURE-LET, (Luisier et al., 2007)), image registration and spectral unmixing. In addition, a set of common spatial and temporal filters, such as Gaussian, median, boxcar and Savitzky-Golay filters is also available. An interactive preview directly visualizes the effects of any selected filter in the configured pre-processing pipeline. Although the pipeline is freely customizable, a default set of filters is automatically added to the pre-processing pipeline, consisting of spatial denoising, followed by a temporal median filter. The temporal median filter by default has a kernel size of three temporal samples. This ensures that no amplitude peaks with respect to the Shannon-Nyquist theorem are removed. Simultaneously this filter can eliminate small motion artifacts and perturbations that persist only during a single frame, so-called shot-noise, while at the same time preserving sharp signal edges. In general, it is recommended to individually add or omit preprocessing stages, based on the quality (i.e. degree of degradation) of a given dataset. For this study, the default preprocessing pipeline was used and only adapted for individual datasets, if either the fluorescence signal was of low quality or significant image drift was present.

6.1.6.3 Interactivity and direct visual feedback

A fundamental design choice was made to not only develop a context sensitive graphical user interface (GUI, Figure 35), but further display interactive visual feedback during the configuration of each step of the processing pipeline. This creates rigorous runtime and modularity requirements for each algorithm. For example, individual steps of an algorithm are required to be executable independently and return an immediate result in order to allow a user to judge subjected modifications. This interactivity brings the benefit of immediately

recognizing quality improvements or deteriorations, eliminating laborious and time-consuming cycles of repeated parameter tuning and subsequent execution of the processing pipeline. Moreover, this approach supports the analyst in gaining a visual understanding of each individual parameter of a particular algorithm.

In addition to the interactive configuration of algorithms, MSparkles features a dynamic, context sensitive GUI providing a reactive dataset preview which allows to explore the fluorescence profile of each individual pixel. Detected ROIs and obtained results are not only presented to the user, but can be individually explored. Thereby, the spatiotemporal relationship between a ROI, its temporal evolution and extracted transients is maintained and graphically highlighted.

6.1.6.4 Visualization

Visualizing data is essential, not only to present results, but also to help better understand and interpret observed phenomena. The former is part of information visualization, presenting data, results and interconnections in a more abstract manner. The latter is the essence of scientific data visualization. MSparkles provides a variety of visualization methods (Figure 37) as well as built-in tools to easily create and export graphs and videos (Figure 35). Display adjustments allow to change the brightness, perform γ-correction and assign individual channel colors.

Data visualization

Data obtained using 2P-LSM are scalar by nature. This is also true for multi-channel recordings, since the channels can be assumed to be independent. The go-to method for visualizing scalar fields is color mapping, where the scalar values in the range $[I_{min}, I_{max}]$ are mapped to a table containing N colors, $C_1, \dots, C_N$. MSparkles provides a set of standard and custom color maps, which are freely combinable with the original dataset and derived scalar fields, such as F_0, $\Delta F/F_0$ and others (Figure 37 A). In addition, the per-frame fluorescence range can be visualized. This allows to see the absolute change in fluorescence per frame with respect to the minimal fluorescence per pixel. Moreover, computing temporal differences $\frac{\delta}{\delta t}\left(\frac{\Delta F}{F_0}\right)$ permits to visualize and color-code increasing as well as decreasing levels of $\Delta F/F_0$. Increasing $\Delta F/F_0$ levels result in a positive value, while decreasing levels will produce negative values. Constant concentrations result in $\frac{\delta}{\delta t}\left(\frac{\Delta F}{F_0}\right) = 0$. In combination with a *hot-and-cold* color-code (Figure 37 A), where increasingly positive values are associated with brighter red and decreasingly negative values are associated with brighter blue values, one can easily spot regions of increasing and decreasing fluorescence levels in $\Delta F/F_0$, corresponding to extending and decaying molecular signalling events, respectively.

Information visualization

Besides presenting statistical information about a dataset (Figure 37 D), MSparkles uses several types of graphs to represent spatiotemporal information. Some of them, such as trace-plots (Figure 19, Figure 37 C) are extended versions of already existing visualizations. Others, like transient-duration-heatmaps (Figure 37 B) and Wave plots (Figure 20) are novel visualizations, introduced by MSparkles.

Descriptive statistics

For each analyzed dataset, descriptive statistics about the distribution of transient amplitudes and durations are automatically computed and presented as box-plots (Figure 37 D). Detected transients are automatically classified based on their peak amplitude. Therefore, each of these charts contains an individual boxplot per transient class, plus an additional box-plot providing an overview over all transients. These box-plots are complemented by a scatter plot (Figure 37 D), correlating the peak amplitude on the y-axis with the corresponding transient duration on the x-axis. Computing the linear correlation between the amplitude and duration distribution allows to find relationships between these two properties. Within MSparkles, the interactive correlation-scatter plot highlights individual signals originating from a selected ROI, creating an additional spatial relationship. Both, box-plots and correlation-scatter (Figure 37 D, right) plots are automatically exported at the end of an analysis.

Kymographs

A Kymograph ("Wellenschreiber") originally introduced by Thomas Young (Young, 1807) is a device, monitoring a position over time. Today, the term Kymograph is also used to describe graphical representations, detailing the temporal course of an observation. MSparkles uses color-coded kymographs, also referred to as *heatmaps*, as a dense representation of the time courses of detected ROIs (Figure 37 B). Such kymographs tend to present huge amounts of data in a confined space, and thus can easily become overloaded and difficult to interpret. For this reason, MSparkles introduces a minimalistic version of a kymograph, termed *transient-duration-heatmap* (Figure 37 B). It only shows actually detected and classified transients. The respective color of a depicted transient represents its class and thus indicates transient amplitude strength. The length of a colored segment indicates the transient duration. This permits to visually assess timepoints of high synchronicity. Moreover, this visualization can help to spot patterns and phenomena, requiring further investigation. Finally, MSparkles enhances kymographs by attaching the corresponding synchronicity index, creating a combined qualitative and quantitative visualization (Figure 37 B).
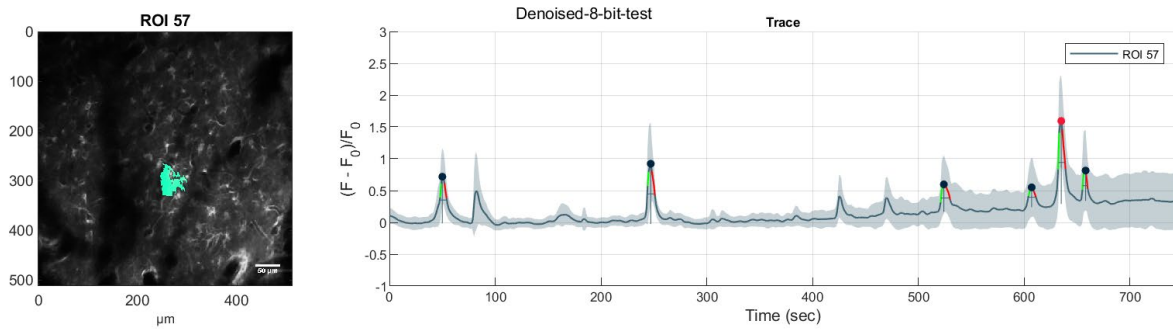
Trace plots

Figure 19: Trace plots. *Trace plots establish a spatiotemporal relation between a ROI and its temporal evolution. The image on the left-hand side of the plot provides an overview of the dataset and highlights the affected ROI. The right-hand side of the plot shows the respective fluorescence profile, with detected and classified peak amplitudes (colored dots), rise and decay times (green and red line segments) as well as the per-frame standard deviation within the ROI (gray semi-transparent area).*

Trace plots (Figure 19) are an extended variant of a commonly used visualization method. By highlighting individual ROIs situated at their precise location within the field of view, alongside with their temporal evolution creates an effective spatiotemporal visualization. This type of graph permits to visually connect the location and extent of an active region with its signaling behavior. In MSparkles, this basic visualization is extended in several ways. Classified transient peaks are marked with distinct colors to intuitively assess a transient's peak amplitude strength. Moreover, transient rise and decay times as well as the measured transient duration are highlighted. This is further extended by the per-frame standard deviation of the recorded fluorescence within the associated ROI, giving an intuition about the uniformity of the fluorescence change within the depicted regions.

Wave plots

Building upon the concept of trace plots, wave plots (Figure 20) are a novel way to visualize the spatiotemporal evolution of dynamic events. Similar to trace plots, wave plots depict the location and spatial extent of an event within the context of the recorded field of view. In order to depict the area occupied by the event in the overview image, the event is projected along its temporal axes. This creates a maximum extent visualization, highlighting each occupied pixel during the event's lifetime. Spatiotemporal event dynamics are depicted in the attached chart, where the X-axis represents the recorded time frame, and the Y-axis shows the spatial extent of the event. The color coding, filling the area of the resulting shape indicates the mean amplitude in $\Delta F/F_0$ at each time point. The wave plot design was developed to be equally well suited for datasets with two as well as three spatial dimensions. Depending on the number of spatial dimensions, the Y-axis can depict occupied area (2D), or volume (3D). For reasons of symmetry, the Y-axis is centered at zero.

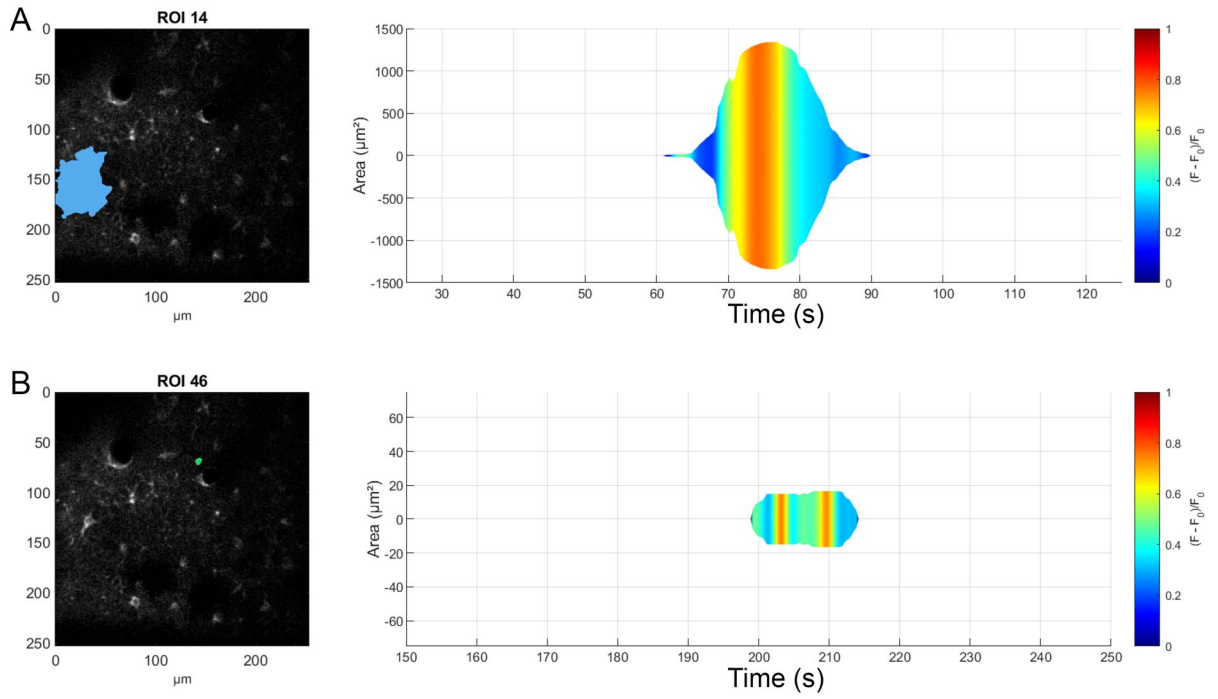***Figure 20: Wave plots.*** *Wave plots are a novel way to visualize spatiotemporal characteristics of a dynamic event. Besides the event duration (X-axis) and amplitude (color gradient), they also display changes in size (Y-axis). A) Large dynamic event, with a single peak in fluorescence (orange section). B) Event with much smaller and almost constant extent, showing two fluorescence pulses (orange).*

6.2 Algorithm evaluation and analysis of fluorescence microscopy data

The PBasE algorithm for F_0 estimation, the CoRoDe algorithm for detecting stationary fluorescence events as well as the KalEve algorithm for extracting dynamic events were individually evaluated. To demonstrate the applicability of these algorithms for the analysis of fluorescence events, astroglial Ca^{2+} events, recorded *in vivo* using GCaMP3 as well as GCaMP5 were analyzed. As a proof-of-concept and to demonstrate the wide applicability of MSparkles' fluorescence event analysis, neuronal Na^+ events, visualized using SBFI-AM, obtained in acute hippocampal slices were analyzed and compared to current literature. For this analysis, ROIs were manually created in ImageJ and imported.

Astroglial Ca^{2+} signals were recorded *in vivo* from three transgenic mice expressing GCaMP3 as well as three mice expressing GCaMP5. Three to four FOVs per animal were recorded in the somatosensory cortex, resulting in a total of 23 and 22 image sequences, respectively. For each recorded FOV animals were imaged first during anesthesia and subsequently during wakefulness. Similar studies, investigating the effects of common anesthetics as well as natural sleep on astroglial Ca^{2+} signaling in the neocortex (Thrane et al., 2012a) and the somatosensory cortex (Bojarskaite et al., 2020; Müller et al., 2021) had previously been performed. These studies served as reference.

Ca^{2+} events were first analyzed in their entirety to compare differences in anesthetized and awake mice. In addition, GCaMP3 signals were subjected to an differential analysis. Therefore, cell somata were marked manually and intersected with the automatically detected ROIs, resulting in two distinct ROI sets, enabling the comparative analysis of somatic events and events in the gliapil.

Next, the CoRoDe algorithm was compared to three other applications for Ca^{2+} analysis, CHIPS (Barrett et al., 2018), CaSCaDe (Agarwal et al., 2017) and AQuA (Wang et al., 2019). The former two generate and evaluate stationary ROIs, whereas AQuA extracts and analyses dynamic events. For this comparison, one FOV was randomly selected per mouse and analyzed in both conditions. In addition, the KalEve algorithm was assessed by direct comparison to dynamic events extracted by AQuA (Wang et al., 2019).

Finally, as a proof-of-principle, MSparkles was used to analyze EEG signals and correlate them to simultaneously recorded Ca^{2+} signals.

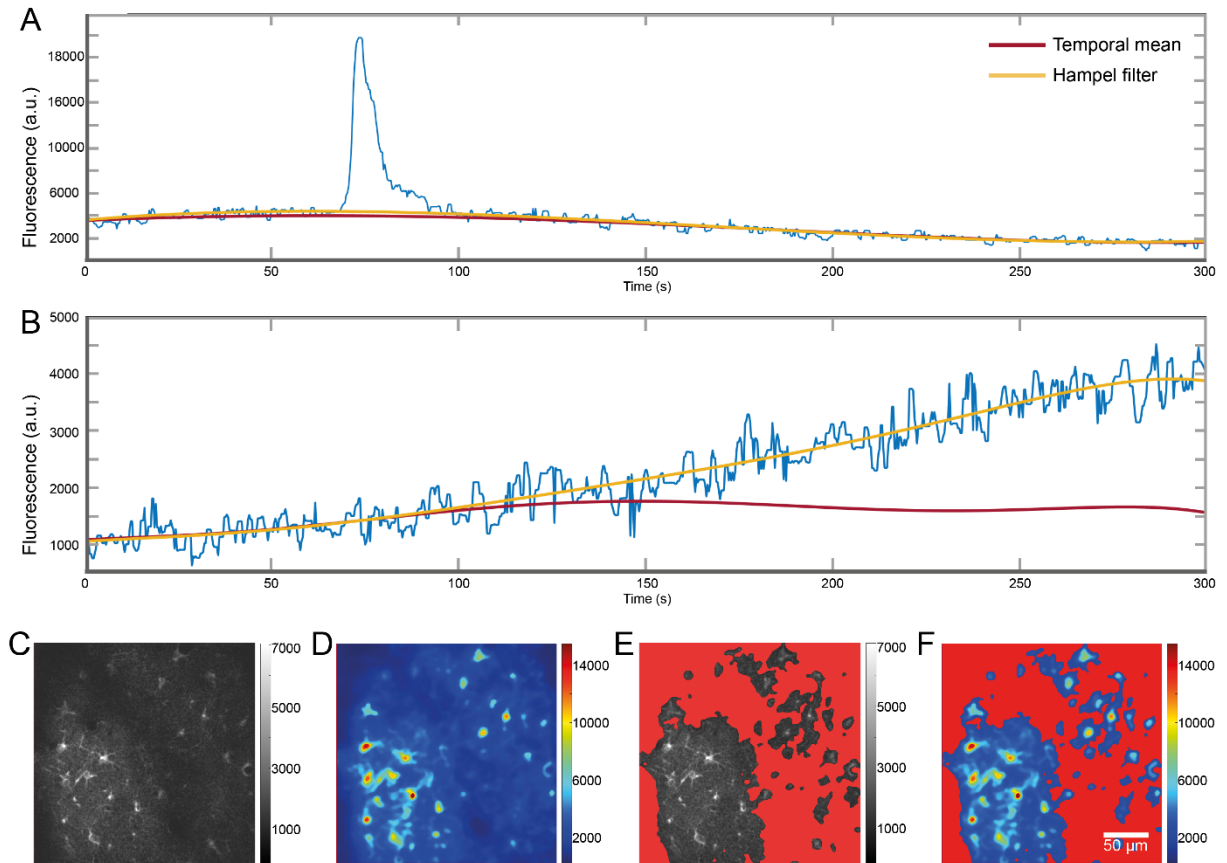## 6.2.1 Evaluation of computational methods

6.2.1.1 F_0 estimation

Figure 21: F_0 estimation. *From the pre-processed fluorescence profile of a pixel (A, B blue curve) potential transients are excluded from background estimation. A polynomial is then fit to the 'clean' signal in a least-squares sense in order to obtain the estimate of the basal fluorescence level. Signal clean-up performed with a Hampel filter (A, yellow curve) returns similar results as the temporal mean filter (A, red curve) if no long-lasting transients are present. The temporal mean filter is capable to retain a stable estimate of baseline fluorescence, preserving long-lasting and slow changes (B, red curve), while the Hampel filter integrates such transients into the background (B, yellow curve). Comparing original fluorescence (C) to the fluorescence range (D) reveals spots of fluorescence activities, not immediately visible in the original image. F_0-mask superimposed on the original image (E) and range projection (F), effectively masking pixels with no, or only little fluorescence activity (dark blue pixels in D).*

The PBasE F_0 estimation algorithm presented in this thesis provides two methods for signal cleanup, a temporal mean filter and a Hampel filter, in order to adapt to different scenarios and requirements (Figure 21). In the presence of moderate fluctuations in basal fluorescence, the temporal mean filter and the Hampel filter both produce similar results (Figure 21 A). In the presence of slow, but strong increases of fluorescence levels (Figure 21 B) the Hampel filter (depending on the kernel size) tends to incorporate these increases into F_0, whereas the temporal mean filter is able to preserve such long lasting and slowly rising transients.

F_0-masking is performed on the range projection of the pre-processed image stack (Figure 21 C, D). This allows to effectively exclude pixels with no or only insignificant changes in fluorescence. Pixels covered by the F_0-mask (Figure 21 E, F) are excluded from the F_0 estimation and set to their respective pre-processed temporal profile. This results in $\Delta F/F_0 = 0$ for the affected pixels and thus prevents the detection of false ROIs and subsequently false transients. A side effect of this approach allows to gain a linear speedup of the F_0 computation, corresponding to the percentage of excluded pixels.

6.2.1.2 Accurate correlation-based detection of stationary events

To assess the quality of ROIs generated by the CoRoDe algorithm as well as the influence of the correlation threshold (t_{corr}), ROIs were obtained at t_{corr} = 0.75, t_{corr} = 0.5 as well as t_{corr} = 0.25 (Figure 22 A), and compared against a matching set of 41 ground-truth ROIs at corresponding locations (Figure 22 B). In addition, ground-truth ROIs were compared to ROIs obtained using a watershed transform, applied to the range projection R (Figure 22 A). In all cases a peak detection threshold of 0.6 $\Delta F/F_0$ on R was used. Ground-truth ROIs were carefully outlined using ImageJ, such that the largest visible extent of a fluorescence event was captured. The dataset, was pre-processed using PURE-LET denoising (Luisier et al., 2010), followed by a temporal median filter with a kernel width of 3 samples. Areas of ground-truth ROIs were compared to the areas of the detected ROIs by computing mean differences as well as relative and absolute size differences (Table 2). The quality of integrated ROI traces was assessed by computing the mean signal-to-noise-ratio (SNR)

$$SNR = 10 \, log_{10} \left(\frac{\mu_{signal}}{\mu_{noise}} \right) \, dB \qquad\qquad 6\text{-}14$$

over all detected ROIs. Here, μ_{signal} and μ_{noise} represent the mean amplitude of the signal and noise portion of an integrated ROI trace. Since 0.5 $\Delta F/F_0$ was chosen as the lowest boundary for transient classification, all values of a given ROI fluorescence profile below 0.5 were considered noise.

Table 2: Validation of detected ROIs. *ROIs detected using CoRoDe are more accurate, than those detected using a watershed transform with identical range threshold. Selecting an appropriate value for t_{corr} reduces nominal and relative errors of extracted ROIs and results in a SNR almost identical to ground truth.*

	Ground truth	Watershed	t_{corr} = 0.75	t_{corr} = 0.5	t_{corr} = 0.25
Mean diff	0.00	51.22	-42.72	-21.30	4.26
Mean abs diff	0.00	51.56	42.72	21.80	13.81
Relative diff (%)	0.00	76.78	-57.13	29.73	18.93
Mean area (µm²)	59.31	110.54	27.18	38.01	63.58
Signal-to-Noise-ratio (dB)	15.60	13.90	18.58	17.20	15.70

Absolute differences in ROI area with respect to the ground truth were significantly reduced for ROIs detected by CoRoDe, when compared to ROIs obtained by the watershed transform (Figure 22 B, D, Table 2). Further, supposing an appropriate correlation threshold, here 0.25 $\Delta F/F_0$, ROIs obtained by the CoRoDe algorithm were found to resemble ground truth ROIs much more accurately, compared to regions obtained by watershed transform (Figure 22 B, zoomed regions). ROIs obtained using a watershed transform were not only found to be oversized (Table 2, Figure 22 B, bottom), but resulting transients were suppressed and in some cases not detected, due to not meeting the minimally required condition of the peak amplitude being ≥ 0.5 $\Delta F/F_0$ (Figure 22 C, bottom). Contrary, ROIs obtained using a correlation threshold of 0.75 turned out to be undersized in this experiment, which resulted in overestimated transient peaks (Figure 22 B, C, top). The quality of ROI fluorescence profiles obtained using the CoRoDe algorithm was assessed and compared to fluorescence profiles of ROIs obtained using watershed segmentation by their SNR (Figure 22 D, Table 2). ROI fluorescence profiles, integrated using ROIs obtained by the CoRoDe algorithm showed an improved SNR, compared to ROIs obtained using a watershed transform (Table 2, Figure 22 E). SNR was significantly reduced in fluorescence profiles integrated with ROIs obtained using watershed transform (Table 2, Figure 22 E). Most importantly, no difference in SNR with respect to the ground truth was computed, using an appropriate correlation threshold of t_{corr} = 0.25 (Table 2, Figure 22 E).
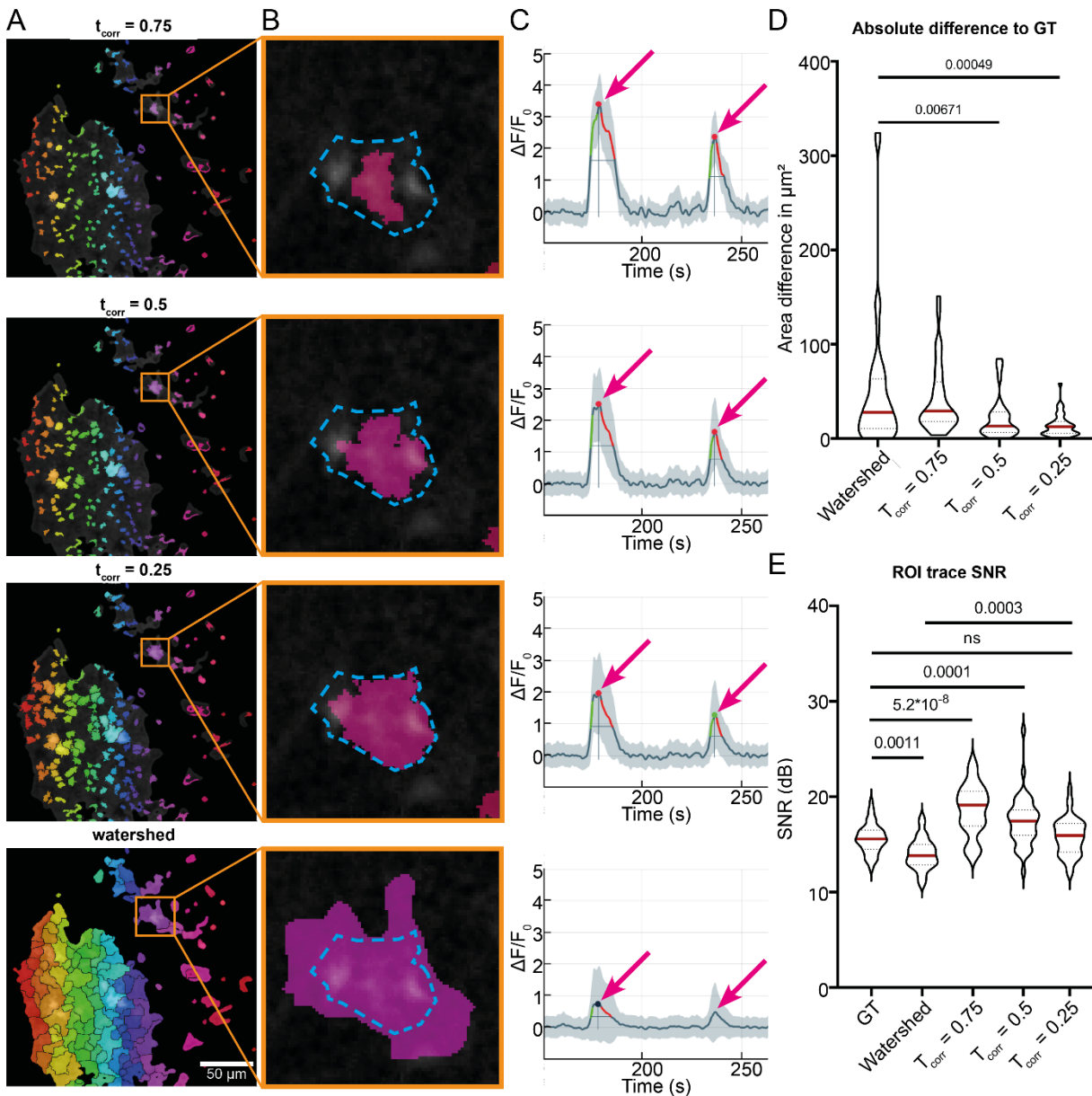
Figure 22: Temporal correlation-based ROI detection. *A) ROIs obtained using CoRoDe with different correlation thresholds (t_{corr}) as well as watershed transform. Correlation thresholds were set to 0.75, 0.5 and 0.25. B) Direct comparison of automatically extracted ROIs to a manually evaluated ground truth. The obtained ROIs (pink) are contrasted to the manually extracted maximal extent of the fluorescence event (dashed blue line). C) Fluorescence profiles from the highlighted ROIs show the influence of segmentation parameters on resulting peak amplitudes. Transients of ROIs obtained by watershed segmentation exhibit too small peak amplitudes (C, arrows), due to improper segmentation. D) ROIs obtained using CoRoDe show significantly less difference from ground truth, compared to watershed transform. E) Integrated fluorescence profiles from ROIs with appropriate t_{corr} show no difference in SNR, compared to ground truth, whereas profiles from ROIs obtained using a watershed transform show a significantly reduced SNR.*

6.2.1.3   Accurate detection of dynamic Ca²⁺ events
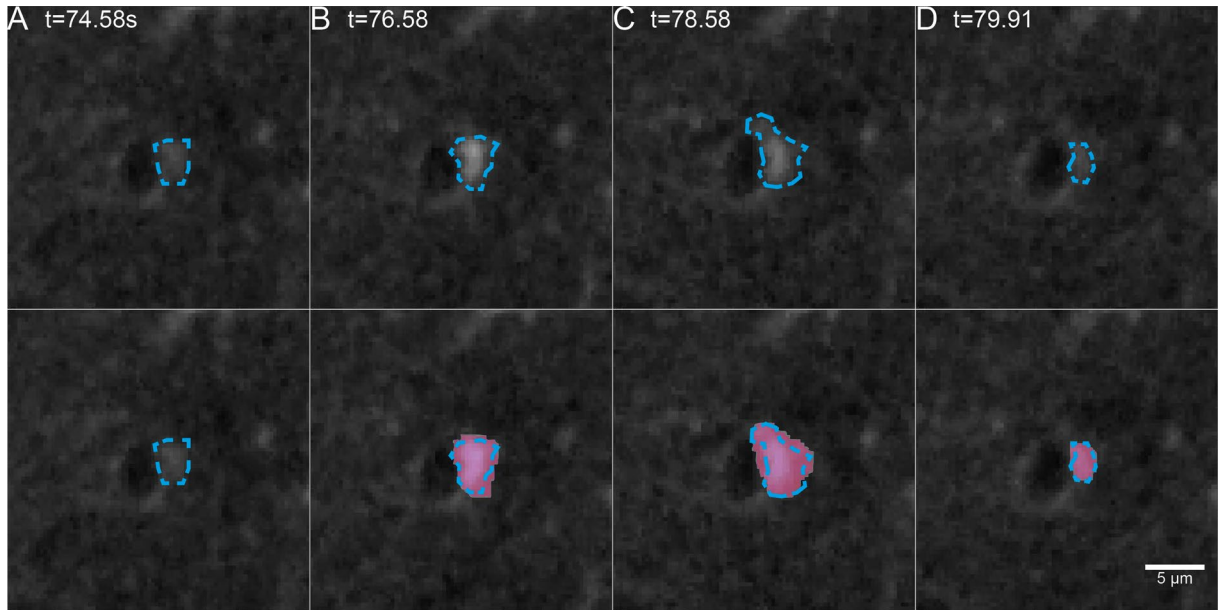

Figure 23: Accurate detection of dynamic events. *Ca^{2+} signal at the vicinity of a capillary. The extent of the Ca^{2+}signal is manually traced and outlined (blue dashed line). The signal extent detected by MSparkles is highlighted in green (lower row). A) Manually determined start of signal, fluorescence change is below detector sensitivity. B-D) Morphological changes of the Ca^{2+} event are detected and traced over time.*

Segmentation and extent of dynamic events extracted using the KalEve algorithm was verified through careful visual evaluation (Figure 23). To do so, dynamic events were first manually tracked and outlined over multiple frames, using ImageJ. Subsequently, events detected by the KalEve algorithm were overlayed with corresponding events outlined in ImageJ for visual comparison (Figure 23). The KalEve algorithm was not only able to detect large dynamic evets, exhibiting strong fluorescence amplitudes (Figure 32 A), but also localized events (Figure 23). In particular, it was verified that the KalEve algorithm is able to reliably detect small events, covering only a few µm² in the FOV (Figure 23).

6.2.2   Characterization of fluorescence events extracted by CoRoDe

6.2.2.1   Number and size of ROIs increased in awake animals

In awake GCaMP3 reporter mice a significant increase in both, the number of detected ROIs as well as the median ROI area was detected (Table 3, Figure 24 A, B), compared to anesthetized animals. ROIs detected in anesthetized animals were exclusively located in the gliapil. The minimal number of detected ROIs was three times higher in awake animals (Table 3). In conjunction to a 50% increase of median ROI count during wakefulness, the median number of transients detected per ROI also doubled (Table 3, Figure 24 C), resulting in the absolute number of detected ROIs to almost double during wakefulness (Table 3, Figure 24 J).

6.2.2.2   Per-ROI transient frequencies did not change

The frequency per ROI was only computed, if a ROI contained more than one transient. Further, the frequency per ROI was computed as the average frequency of transients between the first and the last transient and not as average of total number of transients divided by the recorded timespan. Contrary to previous findings, where a 10-fold reduction in astroglial transient frequency was reported in anesthetized mice (Thrane et al., 2012a), investigating median signaling frequencies per ROI (Table 3, Figure 24 D) showed no difference (0.0285 Hz and 0.0203 Hz) between anesthetized and awake animals, respectively.

6.2.2.3   Ca^{2+} activity increased in awake animals

Investigation of transient kinetics (peak amplitude and transient duration, Table 3, Figure 24 E, F, G, H) revealed no prolongation of median transient duration during wakefulness, compared to anesthetized animals (Figure 24 F). During wakefulness signalling activity was increased and stronger fluctuations in $\Delta F/F_0$ were detectable (Figure 24 E, G), however, the median amplitude did not change between both states (Table 3, Figure 24 E). For further investigation, transients were classified by their peak amplitude (Figure 24 H), and assigned to one of the three classification intervals [0.5, 1), [1, 1.5), [1.5, ∞). This revealed virtually no difference in median amplitude among transients in the lower two classes between anesthetized and awake animals. In awake animals a significant increase in median peak amplitude was found for transients $> 1.5\ \Delta F/F_0$. Based on the amplitude classification, the signal composition was computed (Figure 24 J). Besides an increased number of detected transients in awake animals, a shift in relative frequencies was revealed, nearly doubling the percentage of transients $> 1.5\ \Delta F/F_0$, while the percentage of lower amplitude transients decreased.
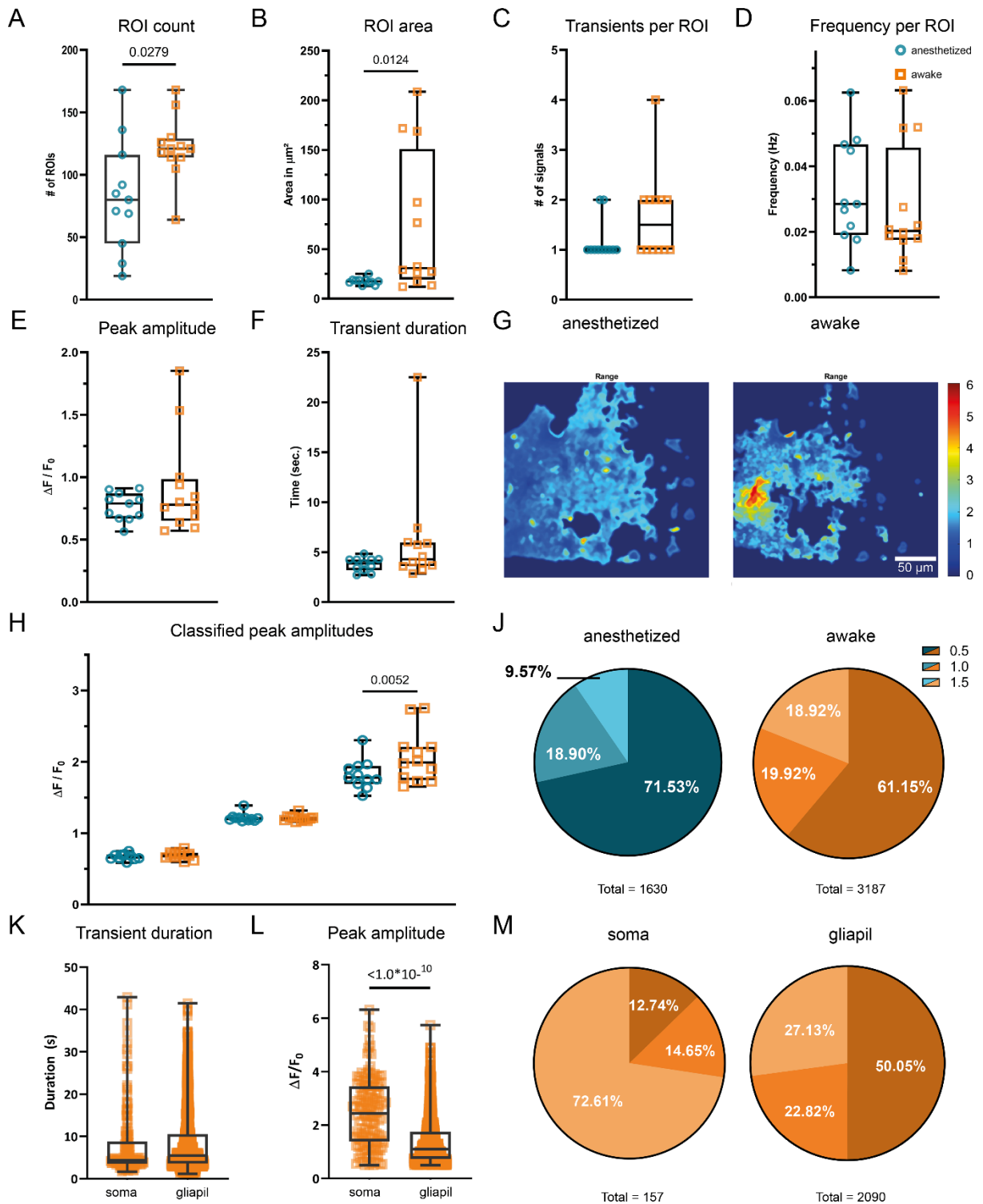
Figure 24: Statistical analysis and transient characterization in GCaMP3 mice. *The median number of detected ROIs (A), as well as the ROI area (B) increased in awake animals. The median number of transients per ROI also doubled in awake animals expressing GCaMP3 (C). Per-ROI transient frequencies did not change (D). The overall median transient peak in awake animals did not change (E). Overall median transient duration also showed no change in awake GCaMP3 animals (F). This increase in fluorescence activity is also reflected in the range projection of $\Delta F/F_0$ (G). Individual classes (H, J) show not only a increase in median amplitude above 1.5 $\Delta F/F_0$ (H) but also a relative increase (signal composition) in strong transients during wakefulness (J). Differential analysis of somatic transients and transients occurring in the gliapil (K, L, M) shows similar median durations (K). Somatic transients exhibit not only a higher median peak amplitude (L), but also occur mostly as high amplitude transients (M), compared to transients in the gliapil.*

6.2.2.4 Differences in somatic and peripheral Ca²⁺ transients

During wakefulness, somatic Ca^{2+} activity could be observed in 75% of the recorded FOVs, whereas no somatic Ca^{2+} activity was observed during anesthesia. In order to analyze somatic events independent of events occurring in the gliapil, a differential analysis was configured. Therefore, an additional ROI set containing manually marked somatic regions was generated. These regions were then subtracted from automatically detected ROIs, resulting in two distinct ROI sets, covering somata and the gliapil, respectively. Comparing somatic transients to transients occurring in the gliapil (Table 4, Figure 24 K, L, M) revealed similar ranges of both, peak amplitude as well as transient duration in both regions. Obtained median durations were also comparable between somatic regions and the gliapil (Table 4, Figure 24 K). Somatic transients exhibited a significantly higher median peak compared to gliapil (Table 4, Figure 24 L). Analyzing raw transient counts revealed about 13 times more transients in the gliapil, compared to somatic regions (Table 4, Figure 24 M). Moreover, the vast majority of somatic transients exhibited a peak amplitude of 1.5 $\Delta F/F_0$ or greater, whereas half of the transients in the gliapil had a peak amplitude < 1.0 $\Delta F/F_0$ (Figure 24 M).

Table 3: Statistical analysis of extracted ROI and transient properties. *ROI counts, area, transient count, mean frequency, peak amplitude and transient duration are shown with their respective minima, 25%iles, 50%iles (median), 75%iles and maxima.*

	Anesthetized						Awake					
	#ROIs	Area (µm²)	#Tran	Freq. (Hz)	Amp	Dur	#ROIs	Area (µm²)	#Tran	Freq. (Hz)	Amp	Dur
Min	19	12.91	1	0.008	0.56	2.71	64	12.17	1	0.008	0.57	2.85
25%	45	16.39	1	0.019	0.67	3.19	114	19.37	1	0.018	0.65	3.60
50%	80	17.50	1	0.028	0.79	3.88	121	30.79	1.5	0.020	0.78	4.28
75%	116	18.74	1	0.047	0.87	4.27	129	150.9	2	0.046	0.99	5.96
Max	168	25.08	2	0.063	0.91	4.84	168	208.6	4	0.063	1.85	22.51

Table 4: Detailed statistical analysis of classified peak amplitudes. *Classified peak amplitudes are shown with their respective minima, 25%iles, 50%iles (median), 75%iles and maxima.*

	Anesthetized			Awake		
	[0.5. 1.0)	[1.0. 1.5)	> 1.5	[0.5. 1.0)	[1.0. 1.5)	> 1.5
Min	0.59	1.17	1.52	0.60	1.16	1.65
25%	0.64	1.18	1.69	0.66	1.18	1.75
50%	0.69	1.21	1.78	0.69	1.21	1.99
75%	0.69	1.22	1.94	0.73	1.23	2.21
Max	0.75	1.39	2.30	0.79	1.32	2.75
#Tran	1166	308	156	1949	635	603

6.2.2.5 Synchronous events are highly diverse

Ca^{2+} activity within a recorded FOV was considered synchronous, if at least half of the detected ROIs were simultaneously active (Figure 25 A). During anesthesia, no significant synchronous activity was detectable (Table 20). In fact, no more than 20% of the detected ROIs were simultaneously active (Table 20). During wakefulness, synchronous activity was detectable with synchronicity values exceeding 90% (Table 20). Investigating the activation sequences of three consecutive synchronous events showed three things. (I) Synchronous activity started from a few ROIs and then spread across the field of view (Figure 25 B, C, D), (II) in the datasets investigated, it was neither possible to identify a predominant direction of propagation nor a repeating propagation pattern (Figure 25). In contrast, some regions directly neighboring the origin of the synchronous event did not show any considerable activity until the very end of the synchronous period (Figure 25 C). (III) In the case of multiple synchronous events being detected, there was a considerable overlap in the active ROIs, but they were never 100% identical. Moreover, the number of ROIs participating in a synchronous event degraded in repeated events (Figure 25 B, C, D). Further, the order of activation was different in consecutive synchronous events (Figure 25 B, C, D). These are only observations from a very limited number of datasets and require further investigation to obtain conclusive results.

6.2.2.6 Ca^{2+} transients based on GCaMP5 are comparable to GCaMP3

Analyzing astroglial Ca^{2+} transients obtained in GCaMP5 reporter mice showed comparable tendencies to those obtained in GCaMP3 mice (Figure 26). Although in awake animals, an increased median ROI count (Figure 26 A), ROI area (Figure 26 B) as well as transient-count per ROI (Figure 26 C) was detectable, only the increased transient count was of statistical significance. Comparing median ROI frequency (Figure 26 D), overall median peak amplitude (Figure 26 E) as well as median transient duration (Figure 26 F) showed no statistical differences between anesthetized and awake animals. Analyzing classified signals showed no difference among comparable classes (Figure 26 H). Due to the reduced intensity of the GCaMP5 fluorescence response (Figure 26 , an additional classification interval in the range of [0.25, 0.5) was introduced. Analyzing signal composition (Figure 26 J) showed a relative increase of higher amplitude transients, as well as a decrease of relative frequency mainly on the expense of signals in the range of [0.25, 0.5), besides an increased total signal count of about 3x in awake animals. Similar to GCaMP3, periods of highly synchronous Ca^{2+} fluctuations only occurred exclusively while animals were awake (Table 21).
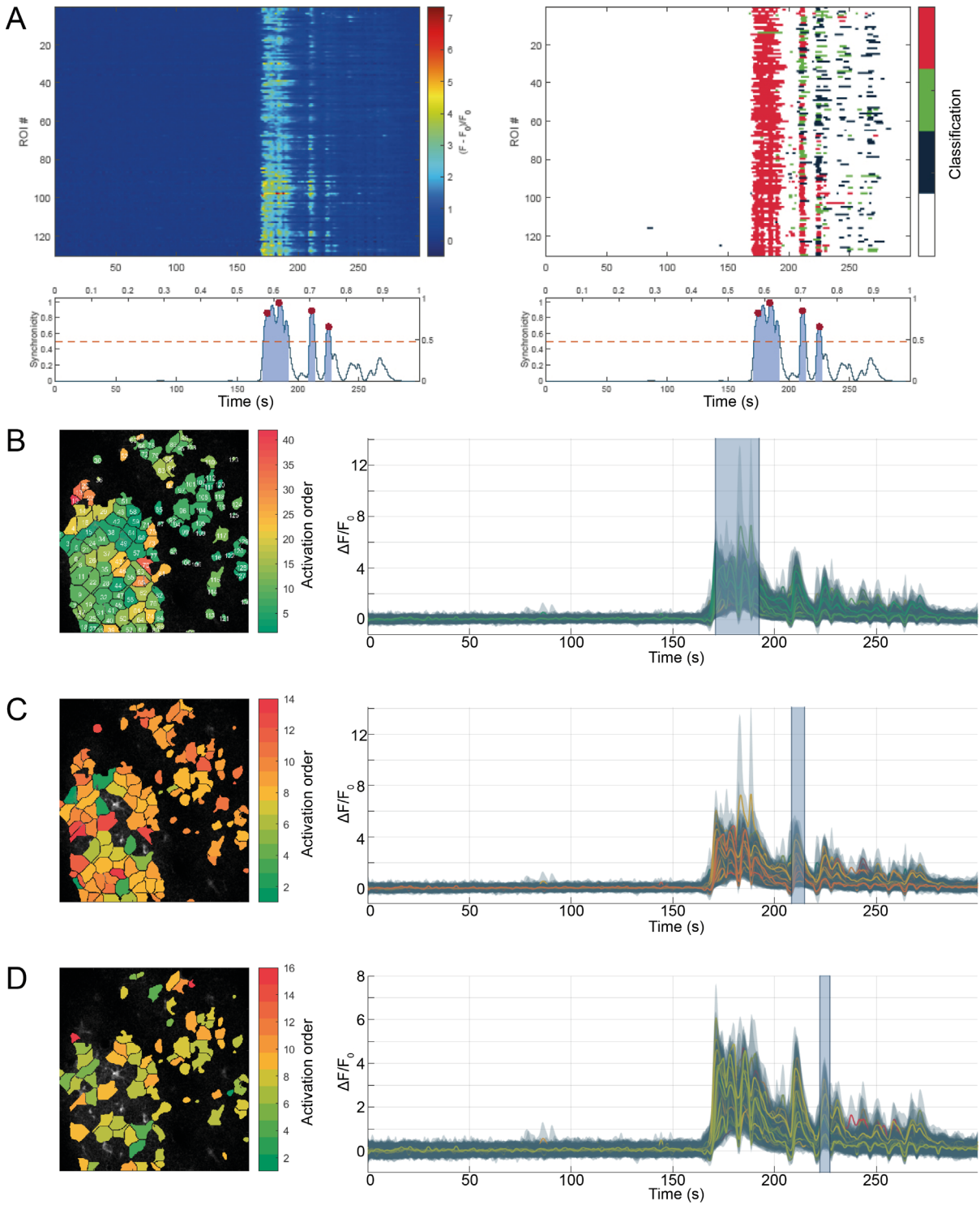
Figure 25: Synchronous events are diverse. *Three separate, but consecutive synchronous events in the same recording. Synchronous events are qualitatively assessable via kymographs, showing unclassified fluorescence profiles (A, left) as well as classified transients (A, right). In addition, synchronicity plots (A, beneath kymographs) allow to quantify the relative frequency of synchronous activity, with respect to the number of detected ROIs. Synchronous periods above threshold (red, dashed line) are highlighted (blue areas), and peaks in synchronicity are marked (red circles). Analyzing individual synchronous events, can reveal activation patterns. Here, color indicates first activation of ROIs, from beginning (green) to end (red) of synchronous event. B) The first synchronous event spread through all of the detected ROIs. C) The second and third (D) synchronous event occured in successively smaller subsets of the detected ROIs. All three events exhibited different activation sequences, and ROIs had substantially different activation time points despite being spatially close to one another. Highlighted time-spans in the attached fluorescence profiles (B, C, D, right) indicate affected period of synchronicity.*
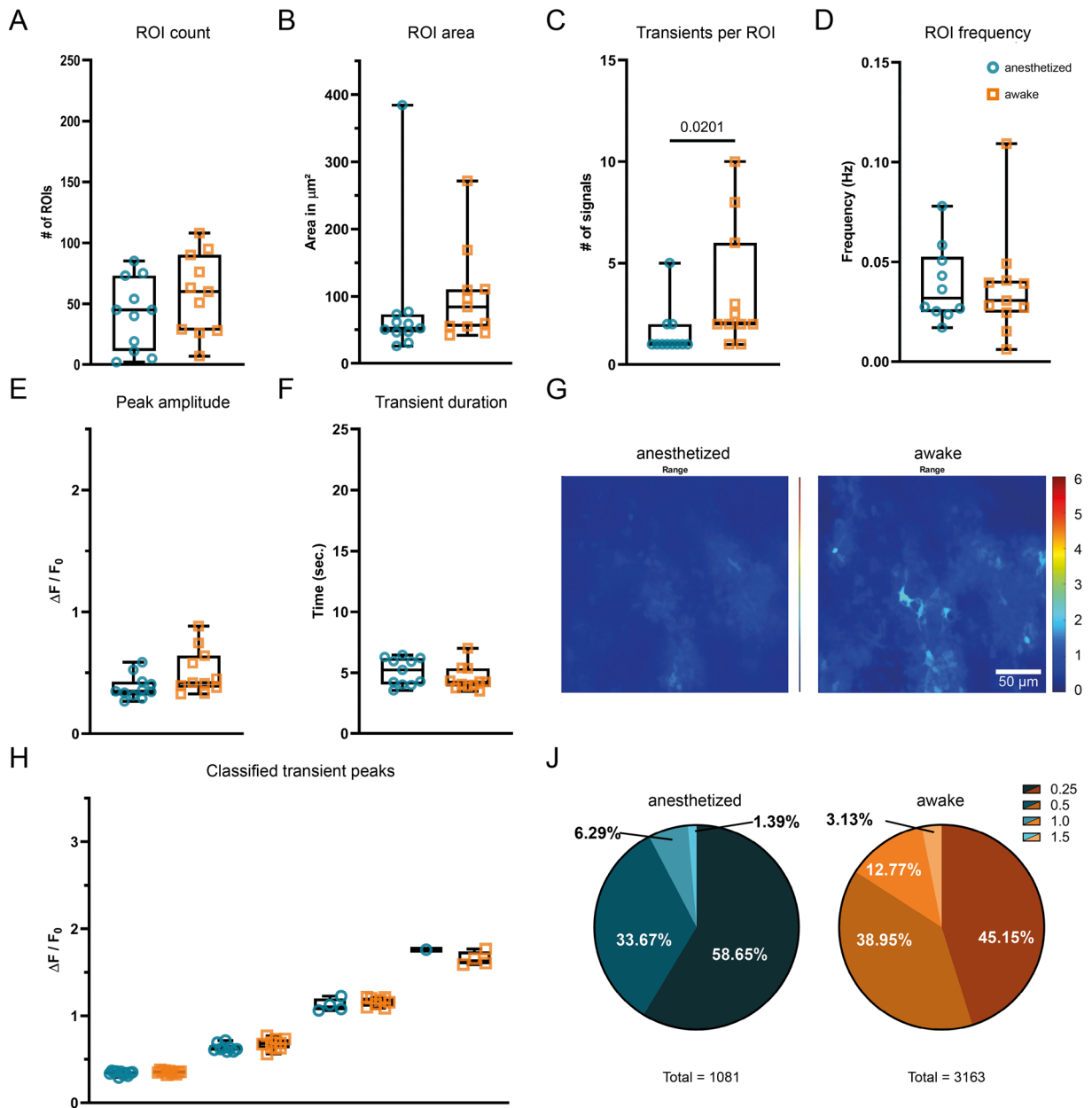
Figure 26: Statistical analysis and signal characterization in GCaMP5 reporter mice. *Awake animals showed no statistical difference in median ROI count (A) and ROI area (B), compared to anesthetized animals. The median count of transients per ROI was increased in awake mice (C). However, per-ROI signaling frequencies did not change significantly (D). No statistical difference in median peak amplitude (E) as well as transient duration (F) was detectable. Comparing classified peak amplitudes, showed no significant in-class differences among anesthetized and awake animals (H). Analysing the signal composition, showed an relative increase in high amplitude transients > 1.0 $\Delta F / F_0$, next to a relative decrease in low amplitude transients < 0.5 $\Delta F / F_0$.*

6.2.2.7   Analysis of dynamic Ca^{2+} events

During anesthesia, the range of detected transient peaks was lower, compared to wakefulness, whereas median peak amplitude was statistically indifferent (Figure 27 A, Table 5). Awake animals showed a reduced median transient duration (Figure 27 B). The median area occupied by a dynamic event did not change significantly during wakefulness (Figure 27 C, Table 5). Dynamic events were able to cover greater maximum distances from their origin during wakefulness (Figure 27 D, Table 5), however no statistical increase in median distance

travelled by dynamic events was detected. Further investigation revealed a 4.3x increase in total transient count (Figure 27 F) in awake animals. Analysis of classified transients showed not only a relative increase of transients exhibiting an amplitude >1.5 $\Delta F/F_0$, but also an increased median amplitude in this class (Figure 27 E, Table 6). Signal composition analysis revealed an increase in relative frequency of strong (>1.5 $\Delta F/F_0$) and weak [0.5, 1) $\Delta F/F_0$ transients, reducing the relative frequency of transients exhibiting a medium-sized peak amplitude (Figure 27 F).
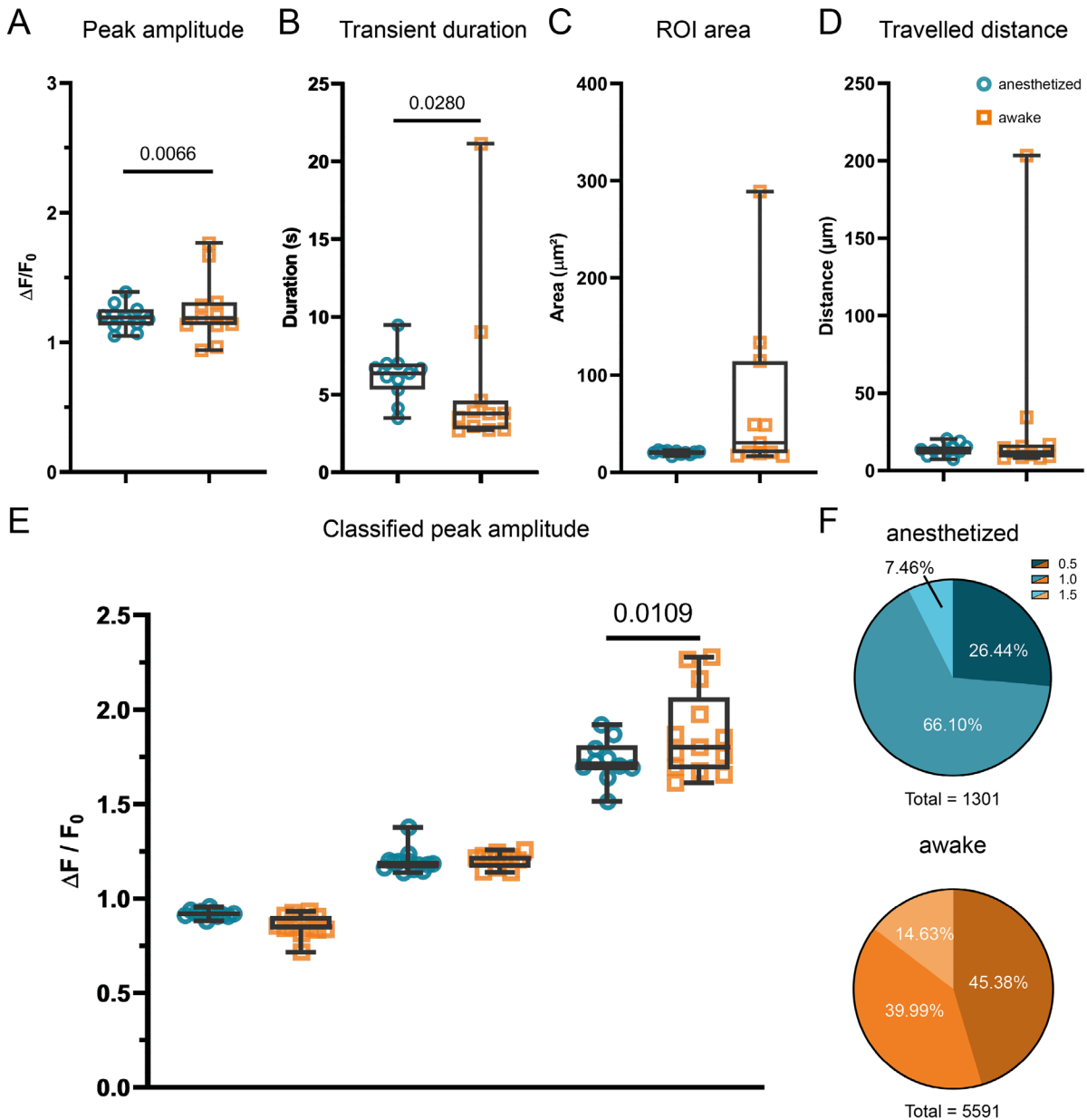
Figure 27: Analysis of dynamic events, detected with MSparkles. *The maximum peak amplitude of Ca²⁺ transients in increased in awake mice, while the median transient duration is reduced (B). Both, average event area (C) as well as the maximum distance travelled by an event (D) showed increased maximal values, but no statistical difference in median values during wakefulness. Investigation of classified transients (E) revealed an increase in peak amplitude in awake animals. Similar to stationary ROIs, the signal composition (F) revealed an increase in relative frequency of both high amplitude ($\Delta F/F_0 > 1.5$) as well as low amplitude ($\Delta F/F_0 < 1.0$) transients. The relative frequency of transients exhibiting an amplitude in the range [1.0, 1.5) was thereby reduced.*

Table 5: Descriptive statistics of dynamic events. *Minimal and maximal values, 25% percentiles median values and 75% percentiles of detected peak amplitudes (Amp), durations (Dur), mean event area as well as the distance travelled by dynamic events.*

	Anesthetized				Awake			
	Amp	**Dur**	**Area (µm²)**	**Dist (µm)**	**Amp**	**Dur**	**Area (µm²)**	**Dist (µm)**
Min	1.05	3.47	16.36	7.19	0.94	2.69	16.54	7.97
25%ile	1.13	5.32	18.70	10.43	1.14	2.76	19.66	8.50
Median	1.19	6.37	20.61	13.06	1.18	3.76	30.35	11.91
75%ile	1.26	7.00	21.41	15.45	1.31	4.61	114.40	16.90
Max	1.39	9.46	22.50	20.51	1.77	21.13	289.00	203.30

Table 6: Peak classification of dynamic events. *Per-class minimal and maximal values, 25% percentiles median values and 75% percentiles of detected peak amplitudes.*

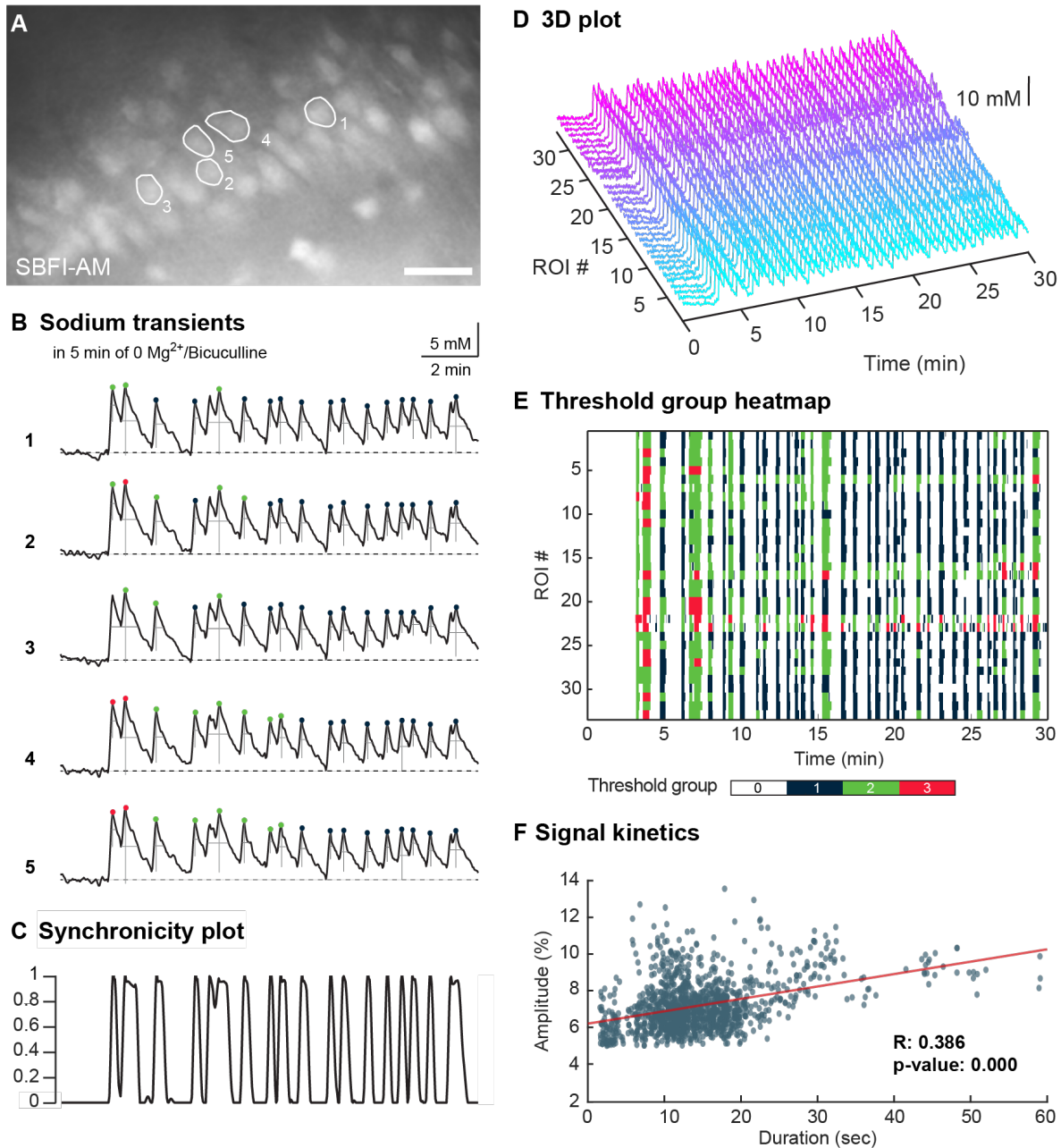|	[0.5 , 1.0)		[1.0 , 1.5)		[1.5 , ∞)	
	Anesthetized	**Awake**	**Anesthetized**	**Awake**	**Anesthetized**	**Awake**
Min	0.88	0.72	1.14	1.14	1.51	1.61
25%ile	0.91	0.84	1.16	1.16	1.68	1.68
Median	0.92	0.85	1.21	1.18	1.71	1.80
75%ile	0.93	0.91	1.23	1.20	1.81	2.07
Max	0.96	0.93	1.26	1.38	1.92	2.28

6.2.3 Analysis of Na⁺ events with MSparkles

Figure 28: Evaluation if Na⁺ signals analyzed with MSparkles *(A) Image of the CA1 pyramidal cell layer of a hippocampal slice (P16) stained with sodium-binding benzofuran isophthalate-AM (SBFI-AM), scale bar is 25 µm. Circles represent regions 1-5 as depicted in (B). (B) Na⁺ signals from regions 1-5 as detected during recurrent network activity. Peaks detected by the software shown by colored dots depending on threshold groups (Red >10% Green >7.5%, Blue >5%). Peak amplitude and full width at half maximum are indicated by black lines. (C) Synchronicity plot of all cells measured in the experiment shown in (A) and (B) (n=33), showing the proportion of cells with activity over time. (D) 3D plot generated by MSparkles, showing Na⁺ traces of all measured cells. (E) Threshold group heat map showing the time points at which each cell was involved in peaks with color code corresponding to that in (B). (F) Scatter plot generated by MSparkles showing the correlation between the duration and amplitude of signals. This figure and therein displayed results have been generated using MSparkles at the University of Düsseldorf. Figure by Lisa Felix & Katharina Everaerts, HHU Düsseldorf*

To demonstrate the applicability of MSparkles beyond the analysis of astroglial Ca^{2+} signals, neuronal Na^+ signals were analyzed as a proof of principle. Recurrent network Na^+ oscillations in CA1 pyramidal neurons, generated by dis-inhibition of the hippocampal network, were reliably detected (N=4 slice preparations from 3 different animals) (Figure 28). For this analysis, ROIs were manually created in ImageJ and then imported with MSparkles. This was necessary, due to non-uniformity of the brightness in ratiometric images, especially near the image boundaries. Computing the ratio of dark image regions, located near the image boundaries resulted in much higher ratios, compared to image regions containing fluorescence events and thus causing the CoRoDe algorithm to detect image boundary regions, rather than pyramidal neurons. F_0-estimation was used to correct drift in the ratiometric data. The onset of Na^+ oscillations was identified after wash-in of the saline containing 0 Mg^{2+}/bicuculline and reported that the network essentially immediately gained a high level of synchronicity (close to 1) between all analyzed CA1 pyramidal neurons in the field of view (30-40 in a given preparation; Figure 28 A-C). Individual transients obtained from neuronal cell bodies were classified into three groups, namely >5, >7.5 and >10% (corresponding to a change in 4.93, 7.39 and 9.85 mM Na^+, Figure 28 B). The corresponding kymograph illustrates that transients detected in individual neurons fell into all three groups, but that individual network events generally tended towards exhibiting either larger (7.5 and 10%) or smaller (5 and 7.5%) peak amplitudes in the contributing cells (Figure 28 E). Peak amplitudes and durations of individual transients were comparable to results published previously (Figure 28 F), (Karus et al., 2015a)). There was a positive linear correlation (R=0.36) between the peak amplitude and the overall duration of individual Na^+ transients.

6.2.4   Comparison with other Ca²⁺ analysis applications

6.2.4.1   Differences in event segmentation and integrated fluorescence profiles

ROIs extracted by the CoRoDe algorithm were compared directly to corresponding ROIs, detected by CHIPS, CaSCaDe and AQuA, analysing the same dataset. Thereby, event segmentation, as well as resulting fluorescence profiles were investigated (Figure 29), in addition to the number of ROIs, the number of not detected active regions (false negatives) and the overall number of extracted transients (Table 17). Comparing event segmentation revealed differences in shape, size and smoothness (Figure 29 A, Figure 38, Table 18). For example, ROIs extracted by CHIPS had rounder shapes, appeared coarser (Figure 29 A) and showed in most cases a larger mean area than ROIs obtained by the other applications (Table 18). Further, segmentation among neighbouring events appeared not as fine-grained as with the other applications. ROIs extracted by CaSCaDe appeared fragmented, and occupied a similar mean area across datasets, compared those obtained by AQuA and MSparkles (Figure 29 A, Table 18). ROIs generated by AQuA appeared rough and fragmented (Figure 38). Overall, the false negative rates of all applications was acceptable with minor variations among applications (Table 17). However, the number of detected ROIs as well as the thereof extracted transients vary strongly between applications (Table 17). Direct comparison of integrated fluorescence profiles revealed several differences. (I) Noise levels of the fluorescence profiles vary across the applications (Figure 29 B). (II) fluorescence profiles obtained with CHIPS showed a drift in baseline fluorescence (Figure 29 B). (III) CaSCaDe tends to extract transients with a longer duration (Figure 29 B, Table 16). (IV) CHIPS and CaSCaDe had difficulties properly resolving spatially close, but temporally separated events (Figure 29 A, B, circled in red and yellow), resulting in fluorescence peaks occurring in the profile of adjacent ROIs (Figure 29 B, C). (V) Integrated fluorescence profiles obtained with AQuA and MSparkles are similar, despite utilizing different analysis paradigms (Figure 29 B, C).

To underline the effects of ROI segmentation on resulting fluorescence profiles, fluorescence profiles of one ROI were overlaid directly (Figure 29 C). This highlights that all applications were able to extract profiles with high resemblance during the first 200 seconds. Especially the prominent amplitude peak occurring after about 100 seconds is largely similar across applications. Due to differences in the segmentation of detected events, fluorescence profiles integrated by CHIPS and CaSCaDe contained an additional prominent peak near the end of the recording, at around 270 seconds.
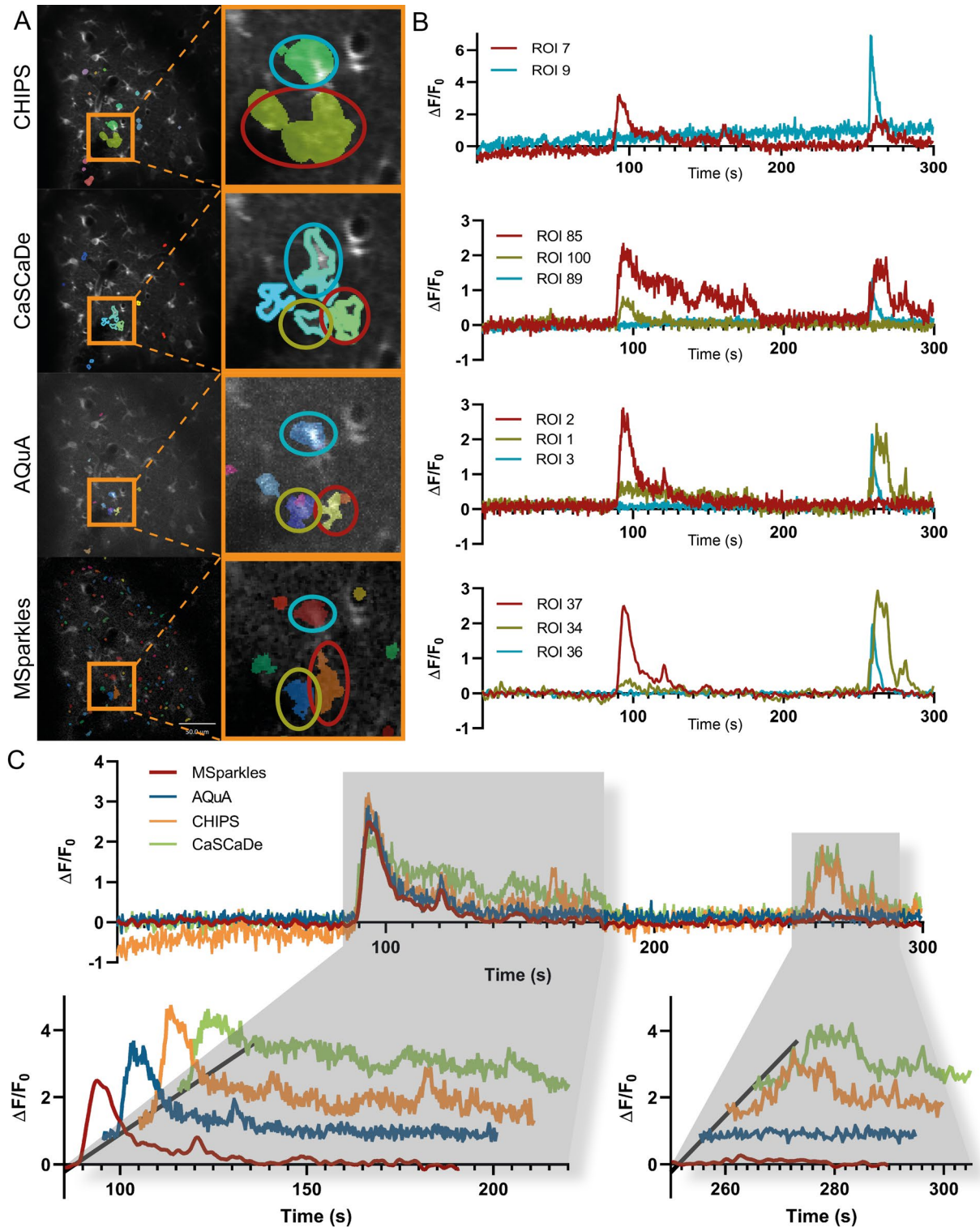
Figure 29: Comparison of ROI detectors. *A) ROIs detected with a specific Ca^{2+} analysis tool. Highlighted areas contain fluorescence activity, similarly detected by all tested applications. Comparing ROIs of the magnified areas reveals segmentation differences, as well as differences in size among Ca^{2+} analysis tools. B) Fluorescence profiles of magnified ROIs marked with red, yellow and blue ellipsesPprofiles obtained using CHIPS show an increase in background fluorescence over time. Especially the profiles obtained with CHIPS and CaSCaDe differ to those obtained with AQUA and MSparkles. AQuA and MSparkles performed a more accurate segmentation between the ROIs marked with red and yellow ellipses, which is reflected by the corresponding fluorescence profiles. C) Direct comparison of fluorescence profiles marked by the red ellipse. Profiles are similar around the first event occurring between 90s and 180s. Profiles by CHIPS and CaSCaDe show a third peak and prolonged event, respectively. CHIPS and CaSCaDe show a second fluorescence event at around 270s. AQuA and MSparkles detected this as a separate event, located at the ROI highlighted in yellow.*
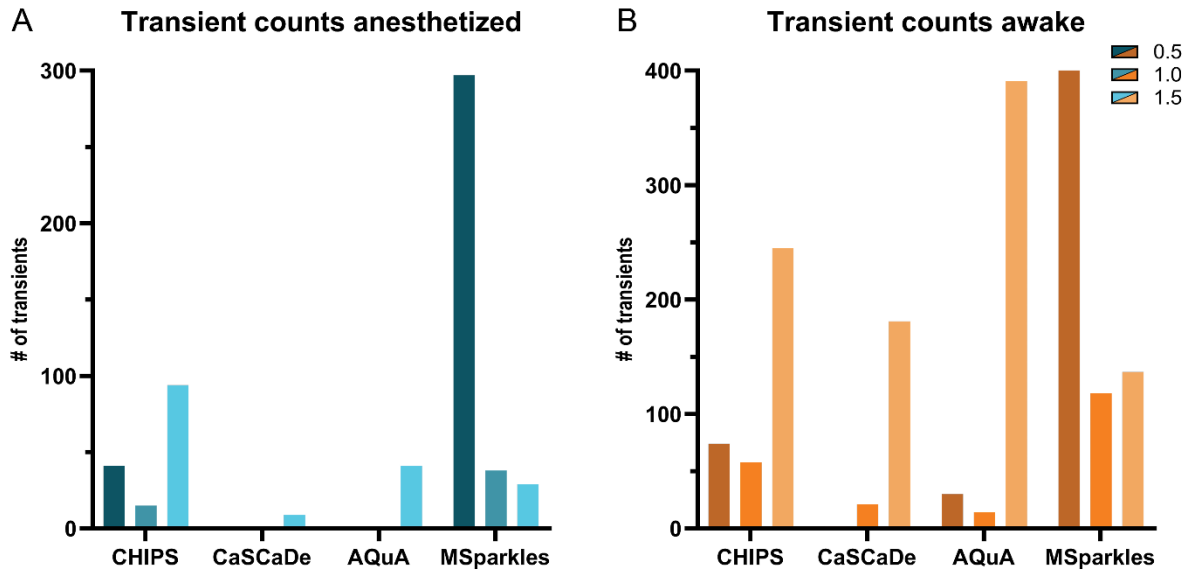
6.2.4.2 Detected Ca²⁺ kinetics are diverse among analysis tools

Figure 30: MSparkles detects more subtle transients. *MSparkles was able to extract overall more transients from the same datasets as the other applications. Moreover, it was able to extract more subtle transients with peak amplitudes < 1 $\Delta F/F_0$ in anesthetized (A) as well as awake mice (B).*

Three FOVs, recorded in mice expressing cytosolic GCaMP3 were chosen randomly to compare the performance of different analysis tools (CHIPS (Barrett et al., 2018), CaSCaDe (Agarwal et al., 2017) and AQuA (Wang et al., 2019)). All FOVs in this comparison exhibited seemingly little Ca²⁺ activity during aesthesia. In one dataset a Ca²⁺ wave within a single astrocyte was observable during awake state. Another dataset contained a large Ca²⁺ wave across the entire FOV during wakefulness.

All applications detected an increased transient count in awake mice (Figure 30). MSparkles was not only able to detect more transients in total, but in particular more low amplitude transients. Especially in anesthetized mice, MSparkles was able to extract about 6x more low amplitude transients than the other applications (Figure 30 A). In awake mice, MSparkles detected about 5x more low amplitude transients then the other applications (Figure 30 B).

Overall, all applications detected a significant increase in median amplitude during wakefulness, compared to anesthesia (Figure 31 A, Table 19). Looking at individual datasets, measured peak amplitudes across the different applications were significantly different between anesthetized and awake states, and in some cases ambiguous (Figure 31 A, Table 11, Table 12, Table 15). In the first dataset CaSCaDe and CHIPS detected no statistical difference between anesthetized and awake mice. AQuA detected a decrease in median peak amplitude in awake state, MSparkles detected an increase in median peak amplitude (Figure 31 A, FOV1). In the second dataset, CHIPS detected an increased median peak amplitude, while the other applications detected no statistical difference (Figure 31 A, FOV2). In the third dataset, AQuA and MSparkles detected an increased median peak amplitude during

wakefulness, while CHIPS and CaSCaDe detected no statistical difference. In all three datasets, the magnitudes of the extracted transient peaks showed considerable differences (Figure 31 A).

Analyzing the extracted transient durations showed similar tendencies (Figure 31 B, Table 13, Table 14, Table 16). Overall, all applications detected an increased median transient duration in awake animals (Table 19). However, looking at individual datasets, none of the tested applications reported significant differences between anesthetized and awake animals in the first dataset (Figure 31 B, FOV1). AQuA detected a decreased median transient duration, while MSparkles detected an increased median transient duration in the second dataset. The other applications did not find significant differences (Figure 31 B, FOV2). In the third dataset, exhibiting a large Ca^{2+} wave, only MSparkles detected a significant increase in median transient duration (Figure 31 B, FOV3). Interestingly, durations reported by CaSCaDe were 2x – 3x longer, compared to the other applications.
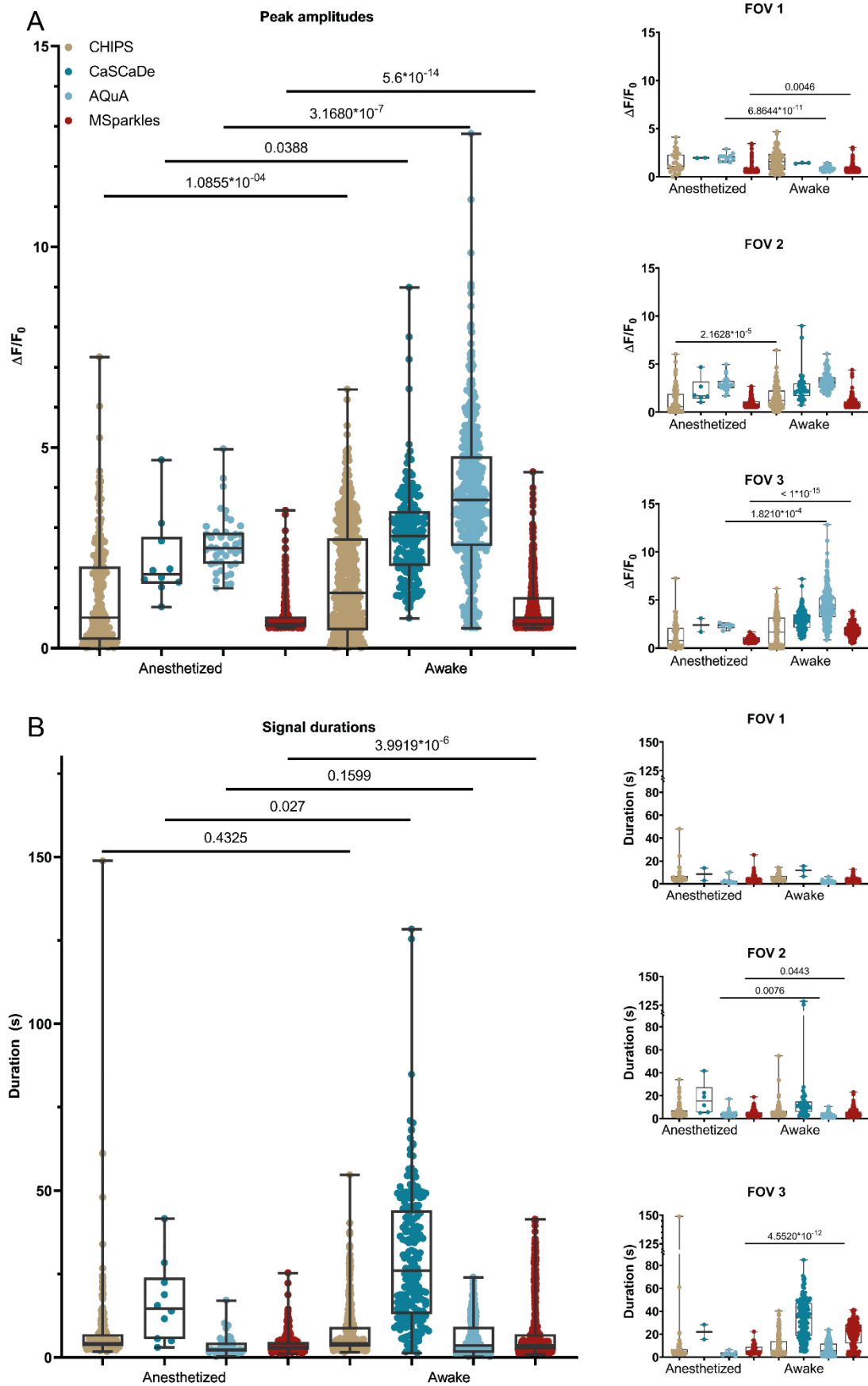
Figure 31: Signal kinetics obtained with different Ca²⁺ analysis tools. *A) Obtained peak amplitudes are diverse across different applications and may result in ambiguous tendencies for individual datasets between applications. B) Transient durations are more consistent, however, CaSCaDe tends to measure longer durations than other applications.*

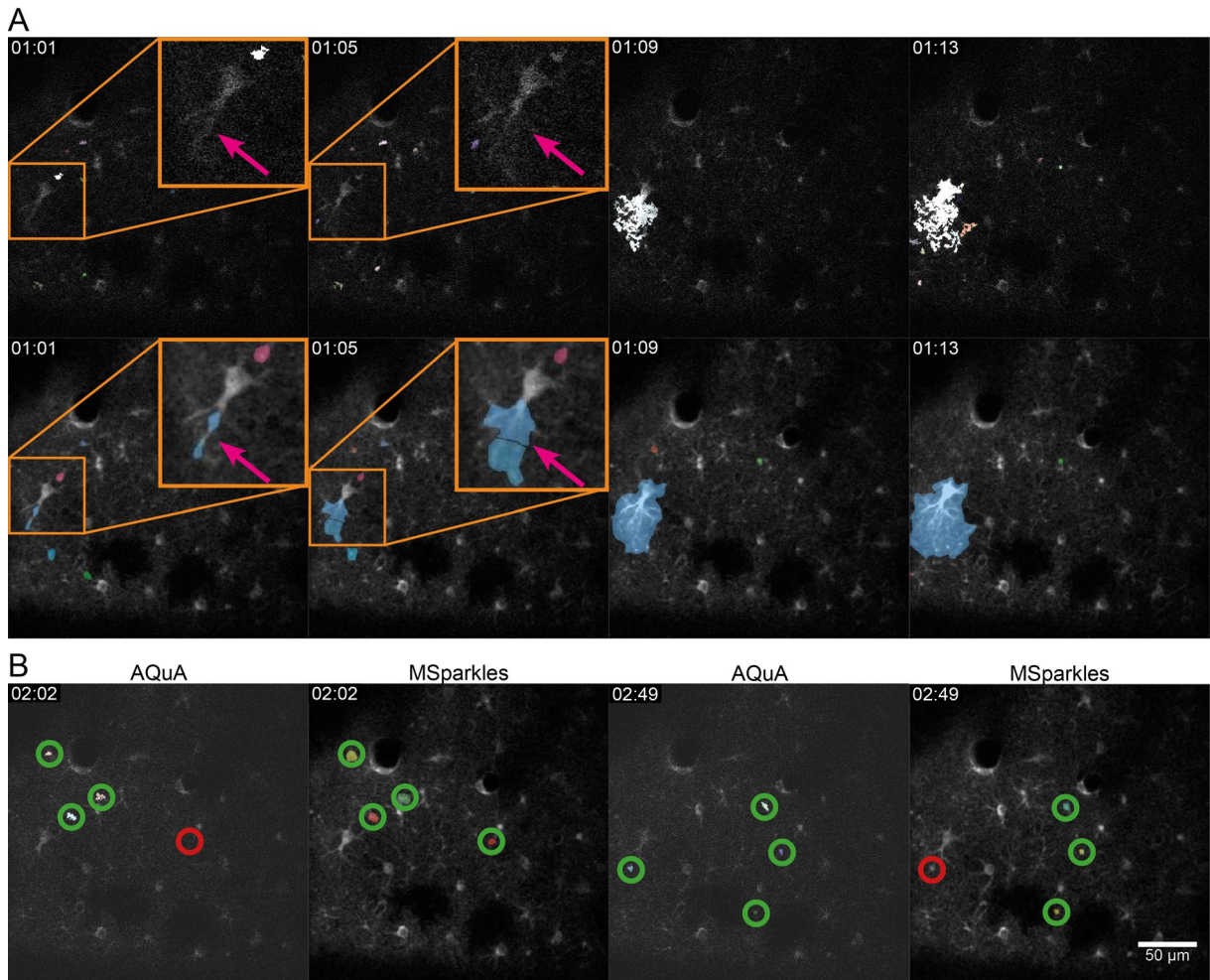### 6.2.4.3 Comparison of dynamic event detectors

A

B

Figure 32: Comparing dynamic events of MSparkles and AQuA. *Comparing dynamic events detected by MSparkles with events obtained using AQuA showed a large resemblance in detected regions (A, B). MSparkles tends to detect the onset of an intracellular Ca^{2+} event earlier than AQuA (A). This allowed to determine the onset of the Ca2^{+} event in one of the astroglial processes and observe its propagation towards the soma. The direct, frame-to-frame comparison of AQuA and MSparkles (B) shows largely identically detected events (green). Events missed by either one of the applications are marked in red.*

AQuA and MSparkles were the only two tested applications being able to detect and analyze dynamic events. For a direct comparison, three datasets obtained from GCaMP3 mice were analyzed with both applications. Each dataset consisted of two image sequences, recorded while the animal was awake and anesthetized, respectively. Event detection and analysis with both applications was performed to achieve the best results, with respect to the author's abilities.

Directly comparing corresponding events, extracted by MSparkles and AQuA showed similar results, with respect to the location and spatial extent of the events (Figure 32 A, B, Table 7). MSparkles was able to detect the onset of Ca^{2+} events earlier than AQuA (Figure 32 A). This made it possible to not only detect an intracellular Ca^{2+} wave, propagating through an entire astrocyte, but further to identify its origin in one of the astroglial processes (Figure 32 A). Both

AQuA and MSparkles largely detected dynamic events at the same locations, with similar spatial extend. However, the median area covered by a Ca^{2+} event differs between both applications, particularly during wakefulness. Both applications occasionally detected some events, missed by the other, and vise-versa (Figure 32 B). Overall, MSparkles detected more active regions than AQuA (Table 7), in particular these regions largely account for fluorescence events in the gliapil, exhibiting peak amplitudes < 1.0 $\Delta F/F_0$.

Table 7: Properties of dynamic events obtained with MSparkles and AQuA. *Comparison of median values for Ca^{2+} peak amplitude, transient duration, event area and total number of detected events in anesthetized and awake animals, as detected by AQuA and MSparkles.*

	Anesthetized				Awake			
	Amplitude	**Duration**	**Area**	**#Events**	**Amplitude**	**Duration**	**Area**	**#Events**
MSparkles	1.20	3.48	15.96	158.00	1.14	2.33	23.89	744.00
AQuA	2.36	2.40	15.00	41.00	3.08	2.10	13.75	435.00

6.2.4.4 Signal properties of dynamic events obtained by MSparkles and AQuA differ

Directly comparing signal kinetics obtained by MSparkles and AQuA showed ambiguous tendencies (Figure 33 A). Median peak amplitudes obtained by MSparkles showed a lower median amplitude than those obtained by AQuA (Figure 33 A, Table 7). Both applications displayed a tendency towards a reduced median transient duration while the animal was awake, with respect to anesthetized state (Figure 33 A, Table 7). Comparing the spatial extent of dynamic events, results obtained with MSparkles suggested an increase in median area during wakefulness (Figure 33 A, Table 7). Analyzing the signal composition (Figure 33 B), suggested similar tendencies of increased relative frequencies of large and small amplitude transients in awake mice. The relative frequencies themselves were vastly different, however (Figure 33 B). In order to compute the signal composition, classification intervals had to be adjusted to account for the generally higher peak amplitudes, detected by AQuA (Figure 33 B).
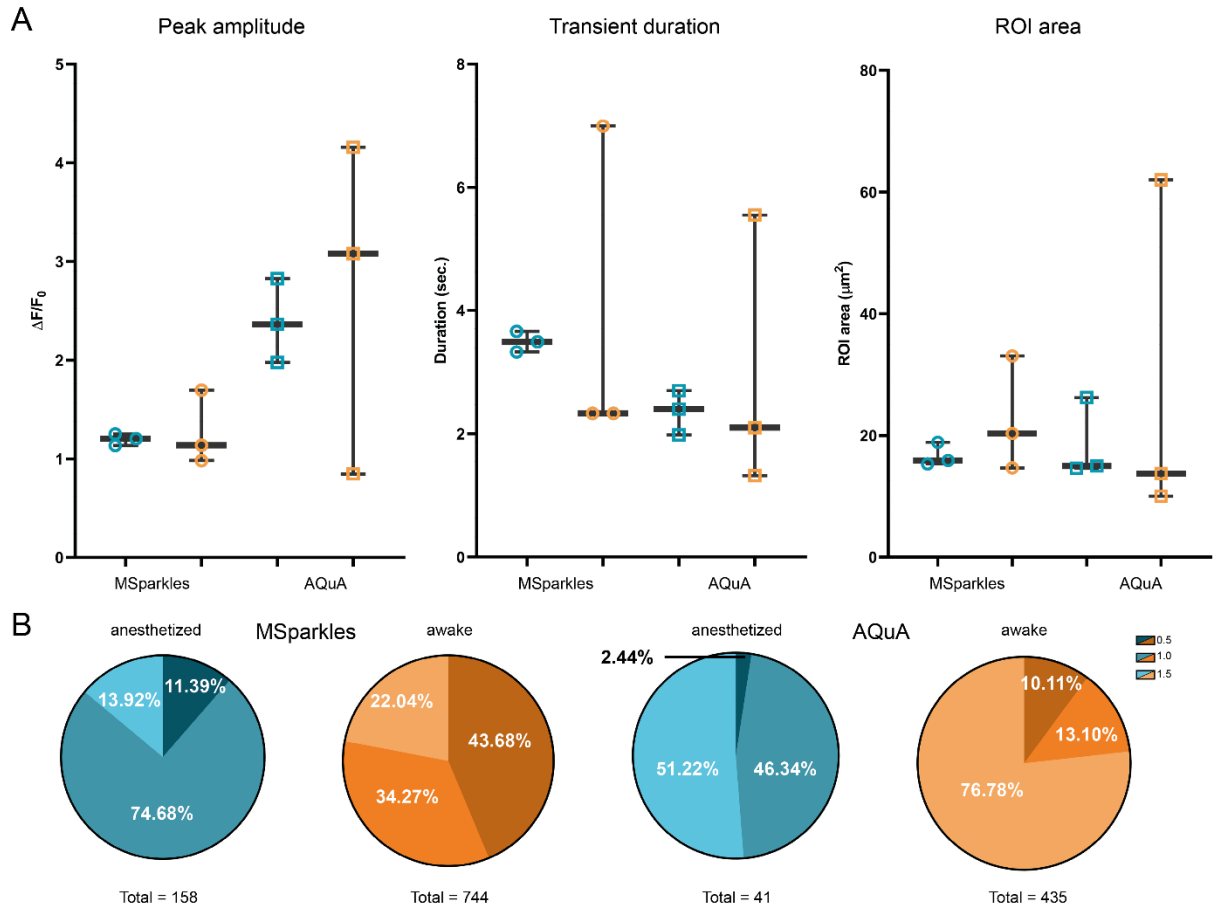
A

B

Figure 33: Statistical comparison of dynamic events obtained with MSparkles and AQuA. A) Obtained median amplitudes differ not only in absolute values, but also in the range of values as well as the projected tendencies. Events extracted by MSparkles are detected sooner, compared to AQuA and thus tend to exhibit longer median durations. Median areas covered by events are larger in MSparkles. B) Signal compositions of MSparkles and AQuA look severely different. However, both, MSparkles and AQuA show similar trends of increased relative frequencies of small amplitude and large amplitude transients in awake animals, at the cost of median amplitude transients. Classification intervals for MSparkles: [0.5, 1.0), [1.0, 1.5), [1.5, ∞) and AQuA: [0.5, 1.5), [1.5, 2.5), [2.5 , ∞) for small, medium and large, respectively.

6.2.5 Evaluation of EEG analysis

To assess the correctness and reliability of MSparkles' spike-train detection and correlated EEG/Ca^{2+} analysis, a proof-of-principle analysis was conducted. Results obtained by spike-train detection were manually verified, whereas results obtained by correlation analysis were additionally compared to previous literature. The analyzed dataset (Figure 34) was recorded in a mouse, expressing GCaMP3, with induced epilepsy, based on (Deshpande et al., 2017). The dataset contains multiple focal seizures and thus provides ideal conditions to evaluate both types of analysis.

6.2.5.1 Spike-train detection

To evaluate MSparkles' spike-train detection, automated analysis results of a test dataset containing multiple periods of hyperactive EEG activity were manually verified. Automated detection parameters were set to a voltage threshold of 300 μV, 2 seconds maximal spike

separation and 10 seconds minimum spike train duration. To reduce noise and increase the stability of the obtained results, the dataset was pre-processed using a Savitzky-Golay filter. To demonstrate spike-train detection, a single channel was analyzed in detail (Figure 34). Four spike trains, with an average duration of 52.0818 seconds (± 19.8547 seconds), lasting for a total of 208.3275 seconds were detected with an average spiking frequency of 8.8952 Hz (± 3.2643 Hz) (Figure 34 A). Upon close inspection (Figure 34 B, C) of the analyzed data, one can see a few false positively detected spikes. These can be mitigated, by either employing additional filtering, or by defining stricter detection rules, than were applied for this proof of concept.

6.2.5.2   Analysis of temporal offset by correlating Ca^{2+} and EEG signals

Cross-correlation analysis was used to determine temporal differences between periods of neuronal activity and astroglial Ca^{2+} activity (Figure 17). The cross correlation was computed between the raw EEG signal, serving as reference signal, and the synchronicity index of the Ca^{2+} events. Based on the maximally computed correlation between these signals, the temporal offset was determined by simple subtraction of the corresponding time points. MSparkles' advanced correlation feature (section 6.1.5.3) was used to compute the cross-correlation of five hyperactive periods. Evaluation of the obtained results suggested that strong, synchronized astroglial Ca^{2+} activity followed neuronal activity, which is in line with recent findings (Berdyyeva et al., 2016; Baird-Daniel et al., 2017; Rossi et al., 2018). MSparkles detected an average delay of 9.637 seconds (± 0.115 seconds) of the synchronous astroglial activity.

Figure 34: EEG spike-train analysis. *A) Four spike trains fulfilling the detection criteria were discovered (colored bars). B, C) Magnification of the second spike train makes it possible to identify individual spikes, and shows that all major amplitude peaks were detected correctly. C) Detailed view of the EEG signal, revealing two false positive spikes (arrow).*

7 Discussion

This thesis presented three algorithms (PBasE, CoRoDe and KalEve) for detecting and analyzing fluorescence fluctuations, evoked by molecular signaling. These algorithms are embedded into a configurable processing pipeline and made accessible by an interactive, MATLAB-based graphical application, called MSparkles. By providing direct visual feedback, MSparkles not only allows to explore fluorescence data, but assists its users in finetuning their detection and analysis parameters. Automatic transient classification permits a fine-grained analysis of fluorescence transients and helps to identify relative changes in signaling behavior. Integrated synchronicity analysis allows to detect and quantify network activity. Moreover, it can be used to analyze signaling and activation patterns. By combining fluorescence analysis with the analysis of secondary signals such as simultaneously recorded ECoG, a correlation analysis can be performed to investigate the interplay of different cell types, such as neuronal cells and glial cells during epilepsy. The capabilities of the presented algorithms and MSparkles were demonstrated by analyzing astroglial Ca^{2+} events, visualized using GCaMP3 and GCaMP5, neuronal Na^+ events, visualized by SBFI-AM and finally, by performing a correlated analysis of simultaneously recorded astroglial Ca^{2+} events and ECoG signals obtained via a brain surface electrode. Finally, the results obtained in this thesis were not only compared to current literature, but also to results from other analysis applications, applied to the same source data.

7.1 Pre-processing

Data acquired using 2P-LSM is typically degraded by various kinds of noise. Additionally, *in vivo* data often suffer from motion artifacts and image drift. MSparkles' freely configurable pre-processing pipeline provides denoising (SURE-LET (Luisier et al., 2007)), image registration, linear unmixing as well as a standard set of spatial and temporal filters (Gaussian, median, boxcar, etc.). Although the pipeline is freely configurable, by default it is pre-configured with spatial denoising, followed by a temporal median filter. These filters are automatically set for each new dataset. The default median filter has a window width of three frames. This ensures that no transients with respect to the Shannon-Nyquist theorem are deleted, but can eliminate small motion artifacts and perturbations that persist only during a single frame, while preserving sharp transient edges. For this study, pre-processing was individually adapted per dataset, if required.

7.2 F_0-estimation with PBasE

Accurate estimation of fluorescence levels at basal concentrations of Ca^{2+} and other important messenger molecules (F_0) is crucial in order to extract low amplitude Ca^{2+} transients such as microdomain events, especially in the gliapil (Müller et al., 2021). During *in vivo* imaging, in particular when performing long-term imaging, basal fluorescence levels can vary. These variations do not necessarily occur homogeneously throughout the FOV. Therefore, a per-pixel estimate of F_0 is necessary. Balkenius et al. (Balkenius et al., 2015) compared different background estimation methods for Ca^{2+} imaging in insect brains with only one fluorescence dye present. They found the most accurate results, by fitting a low-order polynomial to signals before and after the occurrence of Ca^{2+} transients. Recently, an adaptive algorithm to automatically estimate F_0 was introduced and verified by comparing it to a reference signal, recorded in a secondary fluorescence channel (Müller et al., 2021). Approaches, based on biophysical principles (Balkenius et al., 2015; Müller et al., 2021) allow to reveal the fluorescence profile of Ca^{2+} changes (Müller et al., 2021), and make it possible to detect low amplitude events close to noise level. Similar to the algorithm presented in (Balkenius et al., 2015), the PBasE algorithm performs polynomial fitting to estimate fluorescence levels at basal Ca^{2+} concentrations. In addition, it provides two statistics-based methods to automatically exclude fluorescence events from baseline estimation. The Hampel filter allows to closely follow slow fluctuations of given signal and is able to exclude relatively short peaks. Thereby, slow and long-lasting fluorescence elevations are incorporated into the baseline. This may be desirable to compensate for slowly rising basal fluorescence levels e.g. due to thermal activation and closely resembles the behavior presented in (Müller et al., 2021). The temporal mean filter on the other hand is capable to preserve such slow and long-lasting elevations for later analysis, providing extended capabilities, compared to the other two methods. Automatic signal stabilization not only prevents high frequency oscillations, but makes this algorithm suitable for long-term recordings.

7.3 Automated detection of stationary ROIs

In combination with PBasE, the CoRoDe algorithm made it possible to detect a plethora of ROIs containing very dim events, not easily visible to a human observer and also not detectable by most other Ca^{2+} analysis applications. These ROIs were predominantly located in the gliapil, where the majority of Ca^{2+} transients occur (Bindocci et al., 2017). This can be attributed to two reasons. The computed F_0 baseline allows to effectively remove slow fluctuations in background fluorescence and thus to extract subtle transients, otherwise obscured by these fluctuations. In addition, the CoRoDe algorithm is capable to extract fluorescently active regions more precisely than the commonly used watershed segmentation

(Figure 22), permitting subsequent ROI integration to more accurately extract fluorescence transients. Using the fluorescence range for ROI extraction has the advantage to only project actual changes in $\Delta F/F_0$, in contrast to using the original image stack, maximum or summed intensity projections which do not necessarily correspond to fluorescence events and tend to suppress low amplitude transients (Figure 36).

Regional growth is strongly governed by the correlation threshold. A crucial step hereby is to set an adequate parameter for the correlation threshold in order to obtain reliable results. This can be done via an interactive configuration dialog, provided by MSparkles. The range threshold can be used as a lower quality criterion to ensure a minimal change in $\Delta F/F_0$. This allows to generate ROIs closely capturing the actual extent of fluorescence events, by requiring participating pixels to show a minimal level of temporal similarity. It is important to note, that a too high correlation threshold will tend to result in ROIs that are too small, in turn overestimating transient amplitudes.

If multiple events overlap during the recorded time period, these events might not be resolved properly and in some cases might not be detected. This is a general shortcoming of projection-based ROI detectors.

7.4 Automated detection of dynamic events

The KalEve algorithm is based on a Kalman filter, and thus provides robust tracking with respect to image distortions such as motion artefacts. Due to its adjustable sensitivity, this algorithm can detect a large number of active regions, not detectable by other applications. Results obtained with this algorithm agree with recent literature (Thrane et al., 2012a; Bojarskaite et al., 2020; Müller et al., 2021), but require more careful statistical analysis, mainly due to the sensitivity of the of the algorithm and its ability to detect events close to baseline fluorescence. In this study, this resulted in relatively low median amplitudes in both anesthetized and awake anmials. However, analysing the signal composition revealed the relative changes between both conditions, visible in the group of strong signals ($\Delta F/F_0 > 1.5$).

7.5 Automated analysis of Ca^{2+} transients

Analyzing Ca^{2+} transients in awake and anesthetized mice showed an increased ROI count (Figure 24 A, Figure 26 A), ROI area (Figure 24 B, Figure 26 B) as well as transients per ROI (Figure 24 C, C) in awake animals. Further, awake animals exhibited about two times (GCaMP3, Figure 24 J) and three times (GCaMP5, Figure 26 J) as many Ca^{2+} transients, as well as an increased relative frequency of potentially higher peak amplitudes (Figure 24 E, J Figure 26 E, J). This overall increased Ca^{2+} activity in awake animals is in line with previous

studies (Thrane et al., 2012a; Bojarskaite et al., 2020; Müller et al., 2021). No difference in the duration of Ca^{2+} transients was detected in awake animals, using stationary ROI analysis (Figure 24 F, Figure 26 F). However, analysing dynamic events showed a decreased transient duration in awake animals (Thrane et al., 2012b; Bojarskaite et al., 2020; Müller et al., 2021). In both cases, some animals displayed a prolonged transient duration, which can be attributed to the presence of large and long lasting Ca^{2+} waves, exclusively occurring in awake animals.

Classifying Ca^{2+} transients based on their peak amplitude allowed to calculate the signal-composition, i.e. the relative frequency of transient amplitude peaks within a defined interval. This facilitates the detection of changes in the relative incidence of the respective classes, compared to simply analyzing peak amplitudes. Visualizing the signal composition shows not only the overall reduction of Ca^{2+} event activity, but further illustrates that this reduction happens largely on the cost of high amplitude transients, which is line with previous work (Thrane et al., 2012a; Müller et al., 2021).

7.6 Synchronous Ca^{2+} events occur during wakefulness

To detect synchronous event activity, a threshold of 50% simultaneously active ROIs was defined. This is a rather strict criterium, considering up to 220 detected ROIs per FOV in this study. A lower detection threshold of 30% - 40% might be advisable. Synchronous activity, was detected exclusively during wakefulness, which is in line with previous literature (Thrane et al., 2012a). Most of the synchronous activity can directly be attributed to animal motion, clearly visible in the original image stacks as motion artefacts. In addition, detailed investigation of multiple, consecutive synchronous events showed that these events are highly diverse (Figure 25). Each of the detected events showed a different activation order, and no detectable activation pattern. However, with each reoccurring synchronous event, the number of participating astrocytes decreased. One has to keep in mind though, that only one such event series occurred during this study and more data are required.

7.7 Visualization

MSparkles' built-in visualizations help the data analyst to quickly grasp details of intricate datasets. Its specialized tools for graph and video-export help to easily generate powerful visualizations (Figure 19, Figure 20, Figure 25, Figure 37). New and enhanced visualization methods thereby help to present and understand obtained results. Trace-plots connect the fluorescence profile of one or multiple ROIs with their location within the FOV. They further help to visualize the complex activation sequence of synchronous events (Figure 25, Figure 37 B, C).Transient-duration heatmaps are a new, cleaned-up variant of kymographs, only

showing detected transients with their duration, color-coded by their classified transient amplitude. Synchronicity analysis not only allows to identify epochs of highly synchronous signaling behavior, utilizing synchronicity plots, but also the activation-sequence of the affected ROIs. Visualizing the signal composition as relative frequency of classified transients is a simple, yet powerful visualization method, illustrating changes in signalling behaviour, when comparing different conditions.

7.8 Comparison with other software

MSparkles was compared to three Ca^{2+} analysis applications. All of the tested applications detected similar overall trends (Figure 31 A, B, Table 19). Surprisingly, the individual results per FOV were diverse (Figure 31 A, B, Table 15, Table 16, Table 17). Investigating ROIs with high resemblance across all applications (Figure 29, Figure 38) in combination with their corresponding fluorescence profiles provided a possible answer for this diversity. Not only did the number and size of detected ROIs differ substantially, but event segmentation was also considerably different across applications. These factors have a direct effect on the number of extracted transients and more importantly on the amplitudes of fluorescence profiles, directly affecting analysis results (Figure 22). Another critical factor for the analysis of fluorescence events is background correction. If performed improperly, this can result in persistent trends within fluorescence profiles and even in parts of the integrated signal being negative. ROIs subjected to further investigation integrated with CHIPS and CaSCaDe contained a secondary prominent transient (Figure 29 A, B). Further analysis revealed this peak originating from the way fluorescence events were segmented. Only AQuA and MSparkles were able to resolve these ROIs properly (Figure 29). Despite AQuA performing dynamic event analysis, MSparkles' CoRoDe algorithm, generating stationary ROIs, was able to extract nearly identical fluorescence profiles, with the difference being that profiles extracted by MSparkles' appear smoother (Figure 29 A, B). MSparkles is able to detect substantially more events exhibiting a low peak amplitude $< 1.0\ \Delta F/F_0$, compared to the other applications. This has an considerable effect on the statistical evaluation of transient peak amplitudes. For this reason, transients are classified by their respective amplitude and further analysed by their composition (relative frequencies of classes). Transient durations computed with CaSCaDe were 2x to 3x longer than reported by any other application (Figure 31 B). Transient amplitude peaks reported by AQuA tend to exhibit a higher amplitude compared to any other analysis (Figure 31 A). However, AQuA reports fluorescence values based on local maxima, in contrast to averaged values reported by the other applications.

AQuA and MSparkles were the only applications providing a full graphical user interface, granting also non-programming experts access to advanced fluorescence analysis. MSparkles

takes this concept even further, providing specialized user interfaces with direct visual feedback (Figure 35). Additionally, it interactively connects ROIs and analysis results, allowing to easily verify the quality and the plausibility of obtained results in every intermediate step of the processing pipeline. As an effort to work towards a common standard within the Ca^{2+} analysis community we provide extensive definitions and explanations of our terminology and computed event properties (Figure 13, Table 8, Table 9, Table 10).

7.9 EEG analysis

Qualitative and quantitative EEG analysis is essential for the analysis of neurodegenerative diseases. MSparkles tightly integrates the analysis of EEG signals, recorded using brain surface electrodes (Schweigmann et al., 2021) with the analysis of fluorescence signals.

Spike-train analysis is a simple, yet important analysis of EEG recordings, since spike-trains are important indicators of epileptiform activity and correspond to epileptic seizures. They allow to detect periods of hyper-synchronized neuronal activity as well as to quantitatively measure these periods. Visualizing the relative power spectral density across wave bands allows to identify shifts in relative power distribution during a period of hyper-synchronized activity.

The synchronicity index introduced in section 6.1.4.2 shows a prominent peak during strong, synchronized Ca^{2+} activity. Similarly, one can observe a peak in EEG power in the event of an epileptic seizure of TLE, right before it is abruptly down regulated. Cross-correlation is used to determine the temporal difference between both signals (Figure 17 B). In contrast to manually measuring the temporal displacement between synchronicity peaks of both cell types, cross-correlation analysis is robustness against noise, human bias and other perturbations, while still being able to produce reliable results.

Finding the cross-correlation between Ca^{2+} events and corresponding EEG spiking activity (Figure 17 B) can be an important step towards understanding neuropathological diseases. In the scope of epilepsy, this can help identify the role if astroglial Ca^{2+} events during epileptic seizures.

7.10 MSparkles is a versatile analysis tool

MSparkles is a MATLAB-based, application designed to analyze fluorescence changes evoked by molecular signalling. Its interactive and configurable processing pipeline allowed to create optimized analyses for each dataset. Besides analyzing Ca^{2+} obtained *in vivo* from GCaMP3 and GCaMP5 reporter mice, ratiometric Na^+ signals recorded in acute hippocampal slices were successfully analyzed. Each of these use-cases poses different challenges, such as varying

signal-to-noise ratios, vastly different fluorescence levels or motion artefacts. In particular, the ratiometric Na$^+$ signals exhibited about 100x lower amplitudes than Ca^{2+} signals obtained in GCaMP3 animals. To achieve this, three novel algorithms were introduced. PBasE for adaptive background estimation, CoRoDe for the detection of fluorescently active stationary regions, and KalEve to robustly detect and track dynamic fluorescence events. These algorithms made it possible to identify a large number of ROIs not detected by other applications which were predominantly located in the gliapil. From these regions, MSparkles was able to extract close-to-noise Ca^{2+} transients.

Unique features, like differential ROI analysis, multi-threshold transient classification and the analysis of signal composition allowed to compare not only relative changes within transient amplitude classes, but also signaling behavior in somatic regions and the gliapil. The automated analysis of synchronous Ca^{2+} activity allowed to identify the diversity of consecutive network activity.

Ca^{2+} analysis is tightly integrated with EEG analysis and not only allows to identify periods of hyper synchronicity, but the correlated analysis of synchronous Ca^{2+} activity with EEG signals.

Finally, MSparkles provides a full user-interface and requires no programming skills. By automating cumbersome and error-prone tasks like metadata management, parameter documentation and result export, it allows scientists to focus on the analysis of their data.

8 Outlook & conclusions

This thesis presented three algorithms specifically developed to analyze fluorescence fluctuations originating from molecular signalling. PBasE, CoRoDe and KalEve operate independent of the used fluorescence dye. The underlying model of a fluorescence signal provides a high level of abstraction, making these algorithms suitable to analyze arbitrary molecular signals originating from any cell type. This was demonstrated not only by analyzing signals recorded with different fluorophores, but also originating from different cell types in multiple brain regions. In addition, a metric to compute the synchronicity of fluorescence events was introduced and used to not only correlate fluorescence events with EEG recordings, but to measure the delay between electrical neuronal signals and astroglial Ca^{2+} events during an epileptic seizure. These algorithms are encapsulated in an easy-to-use application, called MSparkles.

The unique and interactive connection of MSparkles' algorithms with its graphical user interface allow to create optimized analyzes and do not require any programming skills. Being able to configure multiple analyses per dataset makes it possible to differentially analyze astroglial somata and the gliapil and thus to compare their signaling behavior.

The next steps in the development of MSparkles include:

- Improved analysis of dynamic events, allowing to analyze the direction of propagation and the shape of events in cell networks and on a single-cell level.
- Semi-automated tissue annotation for contextual analysis of signals and their propagation.
- Cell network analysis using graph theory with implicit modeling of the gliapil in combination with boundary interfaces of neighboring cells.
- Advanced, machine learning based analysis of EEG recordings to automatically detect and classify phenomena such as post-ictal depression and specific types of seizures.
- Encapsulate the source code into a modular software library, usable independent of the UI.
- Implement a software module to analyze cultured cells, capable of analysing multiwell plates and automatically classify cell fate.

9 References

Agarwal A, Wu PH, Hughes EG, Fukaya M, Tischfield MA, Langseth AJ, Wirtz D, Bergles DE (2017) Transient Opening of the Mitochondrial Permeability Transition Pore Induces Microdomain Calcium Transients in Astrocyte Processes. Neuron 93:587-605.e587.

Alberdi E, Sánchez-Gómez MV, Matute C (2005) Calcium and glial cell death. Cell Calcium 38:417-425.

Araque A, Parpura V, Sanzgiri RP, Haydon PG (1999) Tripartite synapses: glia, the unacknowledged partner. Trends Neurosci 22:208-215.

Araque A, Carmignoto G, Haydon PG, Oliet SHR, Robitaille R, Volterra A (2014) Gliotransmitters Travel in Time and Space. Neuron 81:728-739.

Baird-Daniel E, Daniel AGS, Wenzel M, Li D, Liou JY, Laffont P, Zhao M, Yuste R, Ma H, Schwartz TH (2017) Glial Calcium Waves are Triggered by Seizure Activity and Not Essential for Initiating Ictal Onset or Neurovascular Coupling. Cereb Cortex 27:3318-3330.

Balkenius A, Johansson AJ, Balkenius C (2015) Comparing Analysis Methods in Functional Calcium Imaging of the Insect Brain. PLoS One 10:e0129614.

Barrett MJP, Ferrari KD, Stobart JL, Holub M, Weber B (2018) CHIPS: an Extensible Toolbox for Cellular and Hemodynamic Two-Photon Image Analysis. Neuroinformatics 16:145-147.

Bean BP (2007) The action potential in mammalian central neurons. NatRevNeurosci 8:451-465.

Bearden LJ, Snead OC, Healey CT, Pegram GV (1980) Antagonism of gamma-hydroxybutyric acid-induced frequency shifts in the cortical EEG of rats by dipropylacetate. Electroencephalogr Clin Neurophysiol 49:181-183.

Bedner P, Dupper A, Hüttmann K, Müller J, Herde MK, Dublin P, Deshpande T, Schramm J, Häussler U, Haas CA, Henneberger C, Theis M, Steinhäuser C (2015) Astrocyte uncoupling as a cause of human temporal lobe epilepsy. Brain 138:1208-1222.

Berdyyeva TK, Frady EP, Nassi JJ, Aluisio L, Cherkas Y, Otte S, Wyatt RM, Dugovic C, Ghosh KK, Schnitzer MJ, Lovenberg T, Bonaventure P (2016) Direct Imaging of Hippocampal Epileptiform Calcium Motifs Following Kainic Acid Administration in Freely Behaving Mice. Front Neurosci 10:53.

Berridge MJ, Bootman MD, Roderick HL (2003) Calcium signalling: dynamics, homeostasis and remodelling. Nat Rev Mol Cell Biol 4:517-529.

Bindocci E, Savtchouk I, Liaudet N, Becker D, Carriero G, Volterra A (2017) Three-dimensional Ca(2+) imaging advances understanding of astrocyte biology. Science 356.

Bohn C, Unbehauen H (2016) Identifikation dynamischer Systeme. Methoden zur experimentellen Modellbildung aus Messdaten: Springer Vieweg.

Bojarskaite L, Bjørnstad DM, Pettersen KH, Cunen C, Hermansen GH, Åbjørsbråten KS, Chambers AR, Sprengel R, Vervaeke K, Tang W, Enger R, Nagelhus EA (2020) Astrocytic Ca^{2+} signaling is reduced during sleep and is involved in the regulation of slow wave sleep. Nat Commun 11:3240.

Brazhe AR, Postnov DE, Sosnovtseva O (2018) Astrocyte calcium signaling: Interplay between structural and dynamical patterns. Chaos 28:106320.

Bubenik P (2012) Statistical topological data analysis using persistence landscapes. In.

Butt AM, Duncan A, Hornby MF, Kirvell SL, Hunter A, Levine JM, Berry M (1999) Cells expressing the NG2 antigen contact nodes of Ranvier in adult CNS white matter. Glia 26:84-91.

Campbell NA, Reece JB, Kratochwil A (2011) Biologie, 8., akt. Aufl., [Nachdr.] Edition: Pearson Studium.

Carmignoto G, Haydon PG (2012) Astrocyte calcium signaling and epilepsy. Glia 60:1227-1233.

References

Caudal LC, Gobbo D, Scheller A, Kirchhoff F (2020) The Paradox of Astroglial Ca2 + Signals at the Interface of Excitation and Inhibition. Frontiers in Cellular Neuroscience 14.

Chazal F, Guibas LJ, Oudot S, Skraba P (2011a) Scalar Field Analysis over Point Cloud Data.

Chazal F, Guibas L, Oudot S, Skraba P (2011b) Scalar Field Analysis over Point Cloud Data. Discrete & Computational Geometry 46:743-775.

Cheng H, Song LS, Shirokova N, González A, Lakatta EG, Ríos E, Stern MD (1999) Amplitude distribution of calcium sparks in confocal images: theory and studies with an automatic detection method. Biophys J 76:606-617.

Cooley JW, Tukey JW (1965) An algorithm for the machine calculation of complex Fourier series. Mathematics of Computation 19:297-301.

Cupido A, Catalin B, Steffens H, Kirchhoff F (2014) Surgical procedures to study microglial motility in the brain and in the spinal cord by in vivo two-photon laser-scanning microcopy. In: Confocal and Multiphoton Laser-Scanning Microscopy of Neuronal Tissue: Applications and Quantitative Image Analysis (Bakota L, Brandt R, eds), pp 37-50: Springer.

David C-s, Lucioles B (2006) Vines and vineyards by updating persistence in linear time.

Deistler M, Scherrer W (2018) Modelle der Zeitreihenanalyse / von Manfred Deistler, Wolfgang Scherrer: Birkhäuser.

Deshpande T, Li T, Henning L, Wu Z, Müller J, Seifert G, Steinhäuser C, Bedner P (2020) Constitutive deletion of astrocytic connexins aggravates kainate-induced epilepsy. Glia 68:2136-2147.

Deshpande T, Li T, Herde MK, Becker A, Vatter H, Schwarz MK, Henneberger C, Steinhäuser C, Bedner P (2017) Subcellular reorganization and altered phosphorylation of the astrocytic gap junction protein connexin43 in human and experimental temporal lobe epilepsy. Glia 65:1809-1820.

Di Castro MA, Chuquet J, Liaudet N, Bhaukaurally K, Santello M, Bouvier D, Tiret P, Volterra A (2011) Local Ca2+ detection and modulation of synaptic release by astrocytes. Nat Neurosci 14:1276-1284.

Drongelen Wv (2007) Signal Processing for Neuroscientists : An Introduction to the Analysis of Physiological Signals. Amsterdam: Academic Press.

Edelsbrunner H, Letscher D, Zomorodian A (2000) Topological persistence and simplification. In, pp 454-463.

Ellefsen KL, Settle B, Parker I, Smith IF (2014) An algorithm for automated detection, localization and measurement of local calcium signals from camera-based imaging. Cell Calcium 56:147-156.

Felix L, Ziemens D, Seifert G, Rose CR (2019) Spontaneous Ultraslow Na(+) Fluctuations in the Neonatal Mouse Brain. Cells 9.

Fernand M (1993) SIGNAL PROCESSING Topographic distance and watershed lines.

Fields RD, Araque A, Johansen-Berg H, Lim SS, Lynch G, Nave KA, Nedergaard M, Perez R, Sejnowski T, Wake H (2014) Glial Biology in Learning and Cognition. Neuroscientist.

Filiano AJ, Gadani SP, Kipnis J (2015) Interactions of innate and adaptive immunity in brain development and function. Brain Res 1617:18-27.

Gee JM, Smith NA, Fernandez FR, Economo MN, Brunert D, Rothermel M, Morris SC, Talbot A, Palumbos S, Ichida JM, Shepherd JD, West PJ, Wachowiak M, Capecchi MR, Wilcox KS, White JA, Tvrdik P (2014) Imaging activity in neurons and glia with a Polr2a-based and cre-dependent GCaMP5G-IRES-tdTomato reporter mouse. Neuron 83:1058-1072.

Giaume C, Kirchhoff F, Matute C, Reichenbach A, Verkhratsky A (2007) Glia: the fulcrum of brain diseases. Cell DeathDiffer 14:1324-1335.

References

Giovannucci A, Friedrich J, Gunn P, Kalfon J, Brown BL, Koay SA, Taxidis J, Najafi F, Gauthier JL, Zhou P, Khakh BS, Tank DW, Chklovskii DB, Pnevmatikakis EA (2019) CaImAn an open source tool for scalable calcium imaging data analysis. Elife 8.

Gonzalez RC, Woods RE (2008) Digital image processing, 3. ed. Edition: Pearson Prentice Hall.

Guo ZV, Hires SA, Li N, O'Connor DH, Komiyama T, Ophir E, Huber D, Bonardi C, Morandell K, Gutnisky D, Peron S, Xu NL, Cox J, Svoboda K (2014) Procedures for behavioral experiments in head-fixed mice. PLoS One 9:e88678.

Haas B, Schipke CG, Peters O, Söhl G, Willecke K, Kettenmann H (2006) Activity-dependent ATP-waves in the mouse neocortex are independent from astrocytic calcium waves. Cereb Cortex 16:237-246.

Hampel FR (1974) The Influence Curve and Its Role in Robust Estimation. Journal of the American Statistical Association 69:383-393.

Hausmann ON (2003) Post-traumatic inflammation following spinal cord injury. Spinal Cord 41:369-378.

Haydon PG (2001) Glia: Listening and talking to the synapse. Nature Reviews Neuroscience 2:185-193.

Haydon PG (2003) The tripartite synapse: astrocytes listen and talk. Journal of Neurochemistry 85:27-27.

Heuser K, Nome CG, Pettersen KH, Åbjørsbråten KS, Jensen V, Tang W, Sprengel R, Taubøll E, Nagelhus EA, Enger R (2018) Ca2+ Signals in Astrocytes Facilitate Spread of Epileptiform Activity. Cereb Cortex 28:4036-4048.

Hoogland TM, Kuhn B, Göbel W, Huang W, Nakai J, Helmchen F, Flint J, Wang SS (2009) Radially expanding transglial calcium waves in the intact cerebellum. Proc Natl Acad Sci U S A 106:3496-3501.

Huang W, Zhao N, Bai X, Karram K, Trotter J, Goebbels S, Scheller A, Kirchhoff F (2014) Novel NG2-CreERT2 knock-in mice demonstrate heterogeneous differentiation potential of NG2 glia during development. Glia 62:896-913.

Im C-H (2018) Computational EEG analysis. methods and applications: Springer.

Jahn HM, Kasakow CV, Helfer A, Michely J, Verkhratsky A, Maurer HH, Scheller A, Kirchhoff F (2018) Refined protocols of tamoxifen injection for inducible DNA recombination in mouse astroglia. Sci Rep 8:5913.

John GR, Scemes E, Suadicani SO, Liu JS, Charles PC, Lee SC, Spray DC, Brosnan CF (1999) IL-1beta differentially regulates calcium wave propagation between primary human fetal astrocytes via pathways involving P2 receptors and gap junction channels. Proc Natl Acad Sci U S A 96:11613-11618.

Jähne B (2012) Digitale Bildverarbeitung. [Elektronische Ressource] : und Bildgewinnung, 7., neu bearbeitete Aufl. 2012 Edition: Springer.

Kalman RE (1960) A New Approach to Linear Filtering and Prediction Problems. Journal of Fluids Engineering 82:35-45.

Karus C, Mondragao MA, Ziemens D, Rose CR (2015a) Astrocytes restrict discharge duration and neuronal sodium loads during recurrent network activity. Glia 63:936-957.

Karus C, Mondragão MA, Ziemens D, Rose CR (2015b) Astrocytes restrict discharge duration and neuronal sodium loads during recurrent network activity. Glia 63:936-957.

Kettenmann H, Verkhratsky A (2013) Neuroglia. In: Neuroscience in the 21st Century (Pfaff DW, ed), pp 475-506. Springer Science+Business Media.

Kislin M, Mugantseva E, Molotkov D, Kulesskaya N, Khirug S, Kirilkin I, Pryazhnikov E, Kolikova J, Toptunov D, Yuryev M, Giniatullin R, Voikar V, Rivera C, Rauvala H, Khiroug L (2014) Flat-floored

air-lifted platform: a new method for combining behavior with microscopy or electrophysiology on awake freely moving rodents. J Vis Exp:e51869.

Kovacev-Nikolic V, Bubenik P, Nikolić D, Heo G (2014) Using persistent homology and dynamical distances to analyze protein binding. In.

Luisier F, Blu T, Unser M (2007) A new SURE approach to image denoising: interscale orthonormal wavelet thresholding. IEEE Trans Image Process 16:593-606.

Luisier F, Blu T, Unser M (2010) Fast interscale wavelet denoising of Poisson-corrupted images. SignalProcessing 10:415-427.

Marchthaler R, Dingler S (2017) Kalman-Filter : Einführung in die Zustandsschätzung und ihre Anwendung für eingebettete Systeme / von Reiner Marchthaler, Sebastian Dingler: Springer Vieweg.

Matias I, Morgado J, Gomes FCA (2019) Astrocyte Heterogeneity: Impact to Brain Aging and Disease. Front Aging Neurosci 11:59.

Mori T, Tanaka K, Buffo A, Wurst W, Kühn R, Götz M (2006) Inducible gene deletion in astroglia and radial glia--a valuable tool for functional and lineage analysis. Glia 54:21-34.

Müller FE, Cherkas V, Stopper G, Caudal LC, Stopper L, Kirchhoff F, Henneberger C, Ponimaskin EG, Zeug A (2021) Elucidating regulators of astrocytic Ca. Glia 69:2798-2811.

Nakai J, Ohkura M, Imoto K (2001) A high signal-to-noise Ca(2+) probe composed of a single green fluorescent protein. Nat Biotechnol 19:137-141.

Nimmerjahn A, Mukamel EA, Schnitzer MJ (2009) Motor behavior activates Bergmann glial networks. Neuron 62:400-412.

O'Carroll SJ, Cook WH, Young D (2020) AAV Targeting of Glial Cell Types in the Central and Peripheral Nervous System and Relevance to Human Gene Therapy. Front Mol Neurosci 13:618020.

Oberheim NA, Goldman SA, Nedergaard M (2012) Heterogeneity of astrocytic form and function. Methods in molecular biology (Clifton, NJ) 814:23-45.

Paukert M, Agarwal A, Cha J, Doze VA, Kang JU, Bergles DE (2014) Norepinephrine controls astroglial responsiveness to local circuit activity. Neuron 82:1263-1270.

Picht E, Zima AV, Blatter LA, Bers DM (2007) SparkMaster: automated calcium spark analysis with ImageJ. Am J Physiol Cell Physiol 293:C1073-1081.

Pologruto TA, Sabatini BL, Svoboda K (2003) ScanImage: flexible software for operating laser scanning microscopes. Biomed Eng Online 2:13.

Richardson WD, Young KM, Tripathi RB, McKenzie I (2011) NG2-glia as multipotent neural stem cells: fact or fantasy? Neuron 70:661-673.

Rossi LF, Kullmann DM, Wykes RC (2018) The Enlightened Brain: Novel Imaging Methods Focus on Epileptic Networks at Multiple Scales. Front Cell Neurosci 12:82.

Rueden CT, Schindelin J, Hiner MC, DeZonia BE, Walter AE, Arena ET, Eliceiri KW (2017) ImageJ2: ImageJ for the next generation of scientific image data. BMC Bioinformatics 18:529.

Rutecki PA (1992) Neuronal excitability: voltage-dependent currents and synaptic transmission. J Clin Neurophysiol 9:195-211.

Scemes E, Giaume C (2006) Astrocyte calcium waves: what they are and what they do. Glia 54:716-725.

Schweigmann M, Caudal LC, Stopper G, Scheller A, Koch KP, Kirchhoff F (2021) Versatile Surface Electrodes for Combined Electrophysiology and Two-Photon Imaging of the Mouse Central Nervous System. Frontiers in Cellular Neuroscience 15.

Shigetomi E, Bushong EA, Haustein MD, Tong X, Jackson-Weaver O, Kracun S, Xu J, Sofroniew MV, Ellisman MH, Khakh BS (2013) Imaging calcium microdomains within entire astrocyte

territories and endfeet with GCaMPs expressed using adeno-associated viruses. J Gen Physiol 141:633-647.

Siuly S, Li Y, Zhang Y (2016) EEG signal analysis and classification. techniques and applications: Springer.

Smith IF, Parker I (2009) Imaging the quantal substructure of single IP3R channel activity during Ca2+ puffs in intact mammalian cells. Proc Natl Acad Sci U S A 106:6404-6409.

Sofroniew MV (2009) Molecular dissection of reactive astrogliosis and glial scar formation. Trends Neurosci 32:638-647.

Srinivasan R, Huang BS, Venugopal S, Johnston AD, Chai H, Zeng H, Golshani P, Khakh BS (2015) Ca(2+) signaling in astrocytes from Ip3r2(-/-) mice in brain slices and during startle responses in vivo. Nat Neurosci 18:708-717.

Stevanovic D (2012) Epilepsy: Histological, Electroencephalographic and Psychological Aspects.

Stopper L, Bălşeanu TA, Cătălin B, Rogoveanu OC, Mogoantă L, Scheller A (2018) Microglia morphology in the physiological and diseased brain - from fixed tissue to in vivo conditions. Rom J Morphol Embryol 59:7-12.

Thrane AS, Rangroo Thrane V, Zeppenfeld D, Lou N, Xu Q, Nagelhus EA, Nedergaard M (2012a) General anesthesia selectively disrupts astrocyte calcium signaling in the awake mouse cortex. Proc Natl Acad Sci U S A 109:18974-18979.

Thrane AS, Thrane VR, Zeppenfeld D, Lou N, Xu Q, Nagelhus EA, Nedergaard M (2012b) General anesthesia selectively disrupts astrocyte calcium signaling in the awake mouse cortex. Proceedings of the National Academy of Sciences of the United States of America 109:18974-18979.

Volterra A, Meldolesi J (2005) Astrocytes, from brain glue to communication elements: the revolution continues. Nat Rev Neurosci 6:626-640.

Volterra A, Liaudet N, Savtchouk I (2014) Astrocyte Ca²⁺ signalling: an unexpected complexity. Nat Rev Neurosci 15:327-335.

Wang Y, DelRosso NV, Vaidyanathan TV, Cahill MK, Reitman ME, Pittolo S, Mi X, Yu G, Poskanzer KE (2019) Accurate quantification of astrocyte and neurotransmitter fluorescence dynamics for single-cell and population-level physiology. Nat Neurosci 22:1936-1944.

Yang Y, Liu N, He Y, Liu Y, Ge L, Zou L, Song S, Xiong W, Liu X (2018) Improved calcium sensor GCaMP-X overcomes the calcium channel perturbations induced by the calmodulin in GCaMP. Nat Commun 9:1504.

Young T (1807) A course of lectures on natural philosophy and the mechanical arts. By Thomay Young, MD.

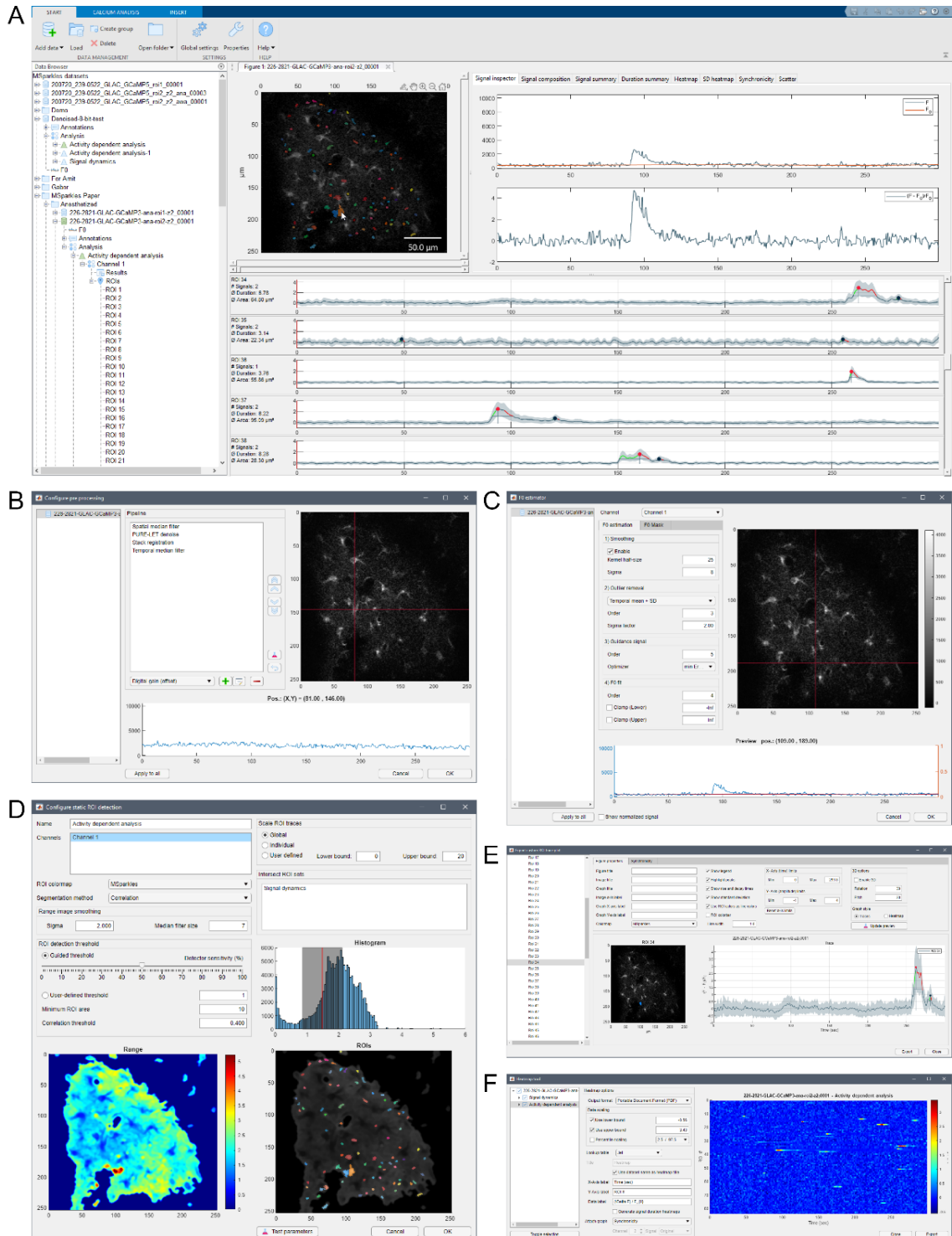# 10 Appendix

MSparkles' user-interface

Figure 35: MSparkles user interface*. A) The main window with its hierarchical data management (left) the currently loaded dataset with detected ROIs (center) and analyzed fluorescence profiles (bottom). Moving the mouse across the loaded dataset, displays the original and the normalized fluorescence profile (top-right) of the pixel currently underneath the mouse pointer. B) Configuration dialogs for pre-processing and C) F_0 estimation with interactive preview. Moving the red crosshair previews effects of the current parameter set to the pixel at the cross-section. D) Configuration of ROI detection displays the fluorescence range image next to a preview of detected ROIs, based on the current detector settings. Export dialogs for trace-plots (E) and heatmaps (F) provide a high level of customization and preview the resulting figures for visual verification.*

Comparison of intensity projections
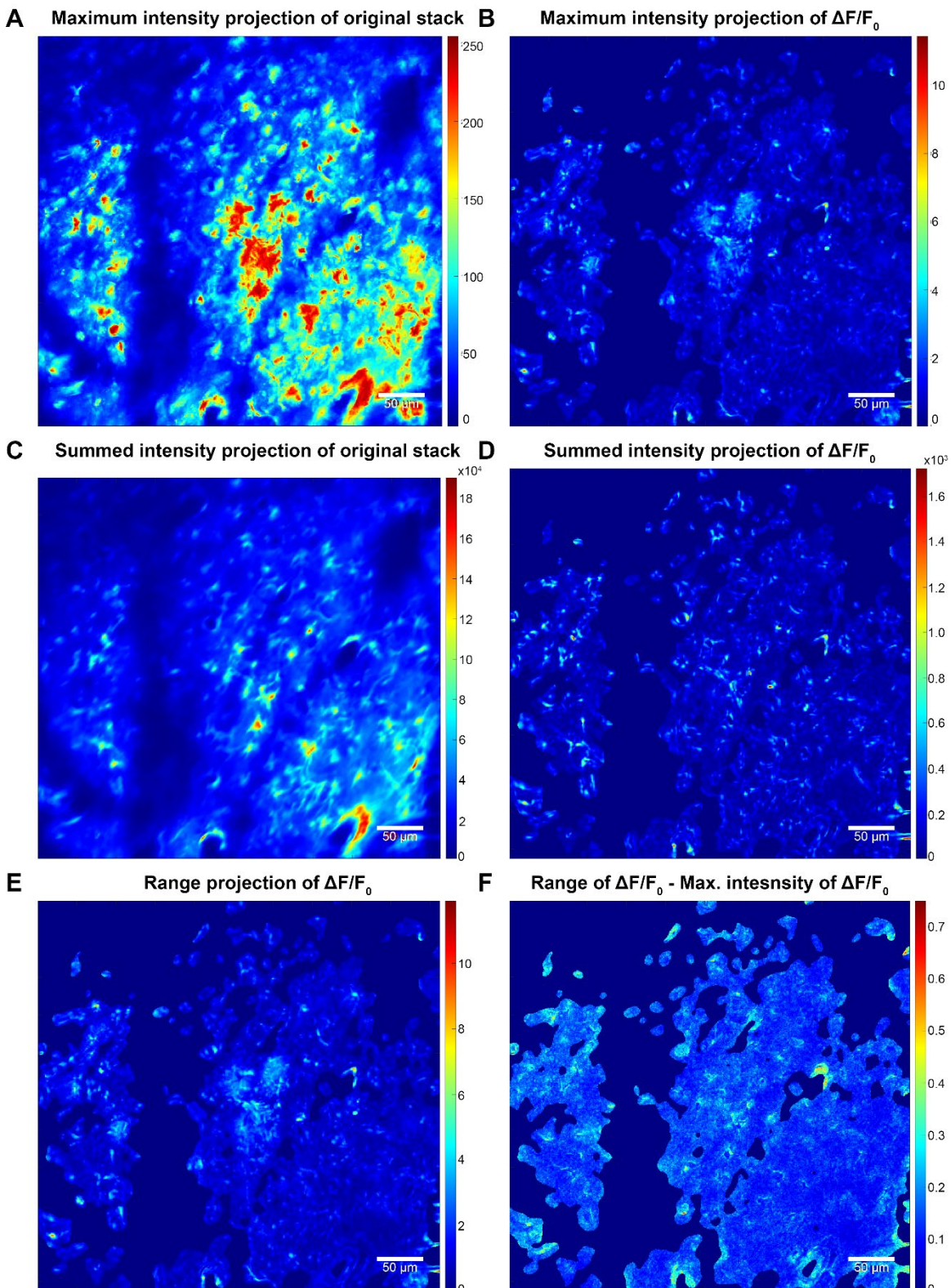
Figure 36: Comparison of intensity projections. *Maximum intensity projections (A, B) and summed intensity projections (C, D) of the original dataset F and $\Delta F/F_0$, respectively. Projections based on F preserve unwanted cell structures. Maximum projections cannot guarantee to project actual signals, while summed projections suppress signals with small amplitude and low frequencies. Fluorescence range projections of $\Delta F/F_0$ (E) on the other hand are capable to reflect the entirety of fluorescence changes. Although maximum projections and range projections have strong visual resemblance, the difference image (F) illustrates areas in which the fluorescence range projection was able to capture stronger differences.*

Table 8: Definition of terminology. *Deinition of terminilogy and quantities used in MSparkles and throughout this thesis.*

Property	Description
Field of view (FOV)	Typically, a quadratic or rectangular area, recorded by a microscope or camera system. FOVs are usually observed and recorded for a defined period of time.
Signal	Amplitude measurement of a physical quantity, recorded within a finite time interval at a defined sampling rate. Signals can be 1-dimensional or multi-dimensional (e.g. images).
Amplitude	(Maximum) elevation of a signal above zero.
Prominence	Measures how much a peak stands out with respect to other peaks or a non-zero reference level immediately before or after the peak. Not necessarily identical with amplitude.
Event	Occurrence of a temporal physiological phenomenon (e.g. local increase of intracellular $[Ca^{2+}]$, occupying a finite area or volume.
Wave	Special type of event with the ability to propagate through space and change its morphology.
Transient	Integrated, 1D representation of an event (ROI trace), identifyable as amplitude increase used for signal analysis (e.g. peak amplitude and duration measurements).
F_{org}	Original, raw dataset or signal obtained from microscope.
F	Dataset after pre-processing.
F_0	Fluorescence levels at basal concentrations of Ca^{2+} or other messenger molecules.
$\Delta F = F - F_0$	Background-subtracted signal.
$\dfrac{\Delta F}{F_0}$	Background subtracted, normalized signal. This signal is considered to be of biophysical relevance and quasi identical to a normalized signal obtained with a secondary reference dye.
Stationary event	Non-migrating fluorescent event, exhibiting little to no change in shape and spatial extent. This might be an inherent property of the event itself, or due to limitations of the recording technology.
Dynamic event	Fluorescent event, able tochange its shape and location, also termed "wave". Dynamic events can occur within a single cell or across multiple cells.
ROI	General term for a hand-drawn or computer-generated area of particular interest e.g. representing the extent and position of a fluorescent event.
Pixel trace	Entire recorded time-span of a pixel.
ROI trace	Signal, resulting from ROI integration. For each ROI, the average value of $\Delta F/F_0$ is computed for each frame.
Height reference	By convention typically measured as *full width at half-maximum* (FWHM). However, MSparkles also has the options to measure the duration at 25% or 10% of maximum.
Start / end of transient	Intersection of height reference with the rising and falling edge of a transient curve.
Rise time	Time delta on the rising edge between start of a transient and 90% of its peak amplitude.
Decay time	Time delta on the falling edge between 90% of the peak amplitude and end of transient.
Transient Duration	Time span between the start and end of a transient.
Peak-to-peak time	Time interval between two consecutive transient peaks.
Start-to-start time	Time interval between the start of two consecutive transients.
Inter-transient time	Time interval between two consecutive transients.

Table 9: Event properties in MSparkles. *Definition of properties of Ca^{2+} transients and dynamic events, variable names and exported quantities measured by MSparkles.*

Property	Description
SigTAvg	Average $\Delta F/F_0$ per ROI per timepoint.
SigTStd	Standard deviation of $\Delta F/F_0$ per ROI per timepoint.
SigTMax	Peak $\Delta F/F_0$ per ROI.
SigTSum	Summed $\Delta F/F_0$ for the entire duration of a detected signal (integral under curve).
SigMax	Peak $\Delta F/F_0$ per event.
SigAvg	Average $\Delta F/F_0$ per event.
SigSum	Summed $\Delta F/F_0$ per event.
Prominence	Signal Prominence of $\Delta F/F_0$ per event.
PxIntersectPoints	Intersection points at x% of the peak value with the signal curve. 50% = Full width at half-maximum (FWHM). Intersection "left" of the peak identifies signal start. Intersection "right" of the peak identifies signal end.
P90IntersectPoints	Intersection points at 90% of peak value "left" and "right" of the peak.
Areas	Area per event (ROI) per timepoint. (constant for stationary ROIs).
AreaCenter	Area center per event (ROI) per timepoint.
StartTime	Time (in seconds) of signal onset per ROI per signal. Depends on the percentage of the peak value at which PxIntersectPoints is determined.
StartFrame	The frame number of signal start per ROI per signal. See StartTime.
PeakTime	Time (in seconds) of signal peak in $\Delta F/F_0$ PeakTime per ROI per signal.
PeakFrame	Frame of signal peak per event (ROI) per signal.
RiseTime	Δt between StartTime and the time point "left" of the peak in P90IntersectPoints per ROI per signal.
DecayTime	Δt between the time point "right" of the peak in P90IntersectPoints and (StartTime + Duration) per ROI per signal.
Duration	Δt between PxIntersectPoints in seconds.
DurationF	Δt between PxIntersectPoints in # of frames.

Table 10: Properties of Ca²⁺ transients extracted from stationary ROI analysis. *Definition of properties of Ca²⁺ transients, variable names and exported quantities measured by MSparkles.*

Property	Description
StartToStartTime	Δt between the starting timepoints of two consecutive signals per ROI.
PeakToPeakTime	Δt between the peak timepoints of two consecutive signals per ROI.
InterSignalTime	Δt between the end of one and the start of the next signal per ROI.
SigMeanFreq	Average signaling frequency per ROI as $\dfrac{1}{\mu_{PeakToPeakTime}}$ per ROI.
AvgArea	Average area per ROI.
MaxArea	Maximum area per ROI.
AvgDuration	Average signal duration per ROI.
AvgDurationStd	Standard deviation of the signal duration per ROI.
PeakCount	Number of peaks per ROI.

Graphs and visualizations generated by MSparkles
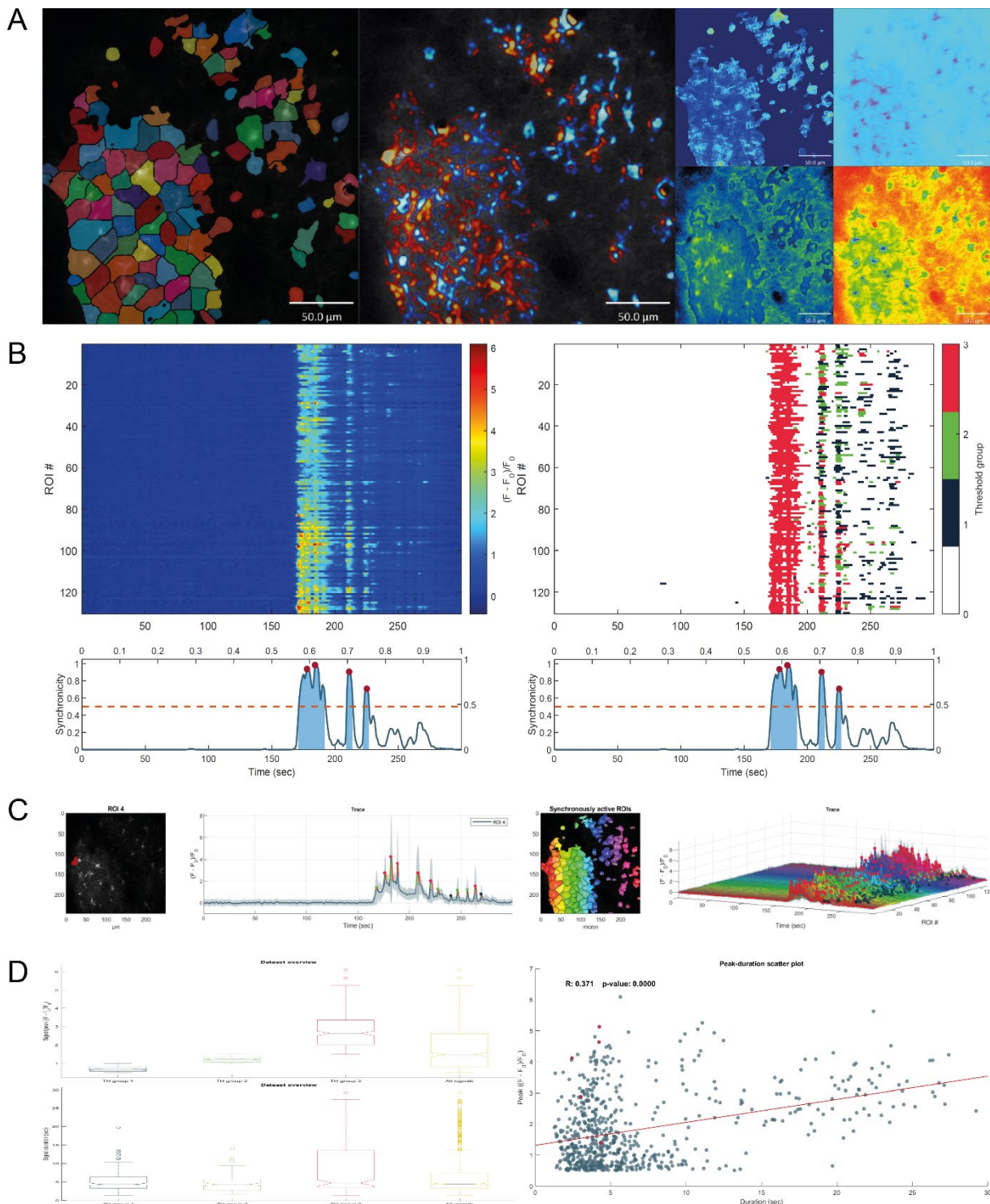
Figure 37: Data visualization. MSparkles features a variety of visualization methods for displaying image datasets (A). These include translucent overlaying of detected ROIs, visualization of temporal derivatives to illustrate fluorescence increase and decrease in a so-called hot-and-cold style, as well as various color maps. Colormaps cannot only be applied to the original data, but also to computed data, such as F_0, ΔF or $\Delta F / F_0$. Heatmaps and signal-duration heatmaps (B) provide a dense and compact overview over an entire dataset. Both kinds of heatmap have an attached synchronicity plot at their bottom to explicitly illustrate periods of highly synchronous signaling events. Customizable trace-plots (C) visualize not only the signals occurring within one or multiple ROIs, but also highlight the spatial relation of a signal within the recorded field of view. Finally, result-plots (D) provide e.g. a statistical overview about the classified distributions of detected signal peaks and durations. Scatterplots additionally highlight the relation between signal peak and duration.

Extended comparison of ROI detectors
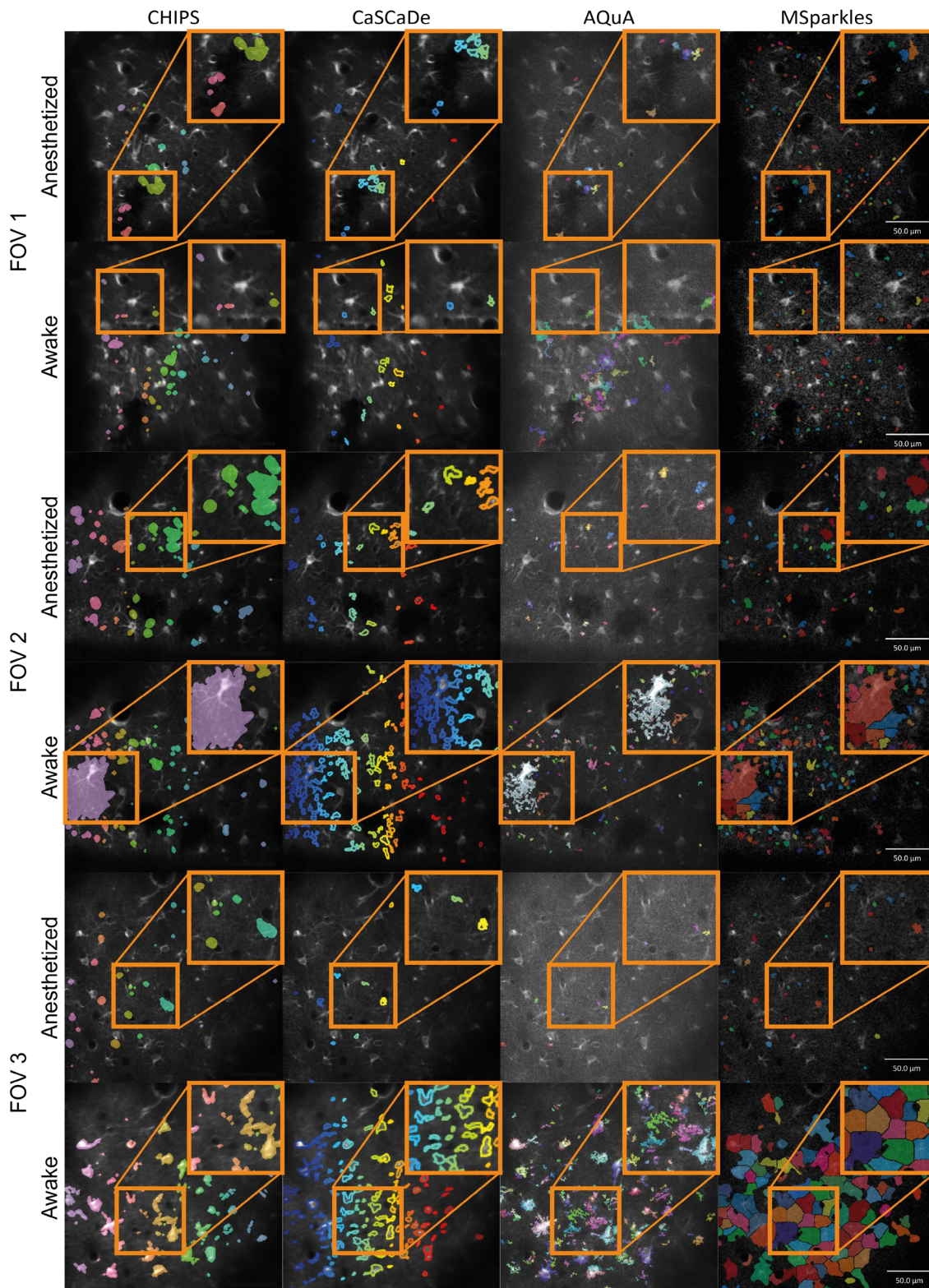
Figure 38: Detailed comparison of ROI detectors. *Each column shows detected ROIs obtained with a specific Ca^{2+} analysis tool. Each row is dedicated to a single FOV. Highlighted regions point out differences in detector sensitivity as well as region segmentation, potentially resulting in ambiguous measurements of ROI sizes and thus differences in ROI integration and resulting peak amplitudes. CHIPS tends to extract large and smooth regions. CaSCaDe extracts regions with a high degree of segmentation. Regions extracted by AQuA tend to be rough and contain holes. MSparkles is able to extract regions with varying smoothness, based on the temporal correlation of pixels. Due to the interplay of the PBasE and CoRoDe algorithms, MSparkles is able to detect active regions with localized and dim fluorescence events. Scale bar 50 µm.*

Table 11: P-values between all peak amplitudes by analysis tool during anesthesia. *P-values indicate statistically significant differences between the results obtained by different analysis applications analysing transients of anesthetized mice. Graphical data shown in Figure 31.*

	CHIPS	CaSCaDe	AQuA	MSparkles
CHIPS		$5.683*10^{-3}$	$< 1*10^{-15}$	$3.741*10^{-5}$
CaSCaDe	$5.683*10^{-3}$		>0.9999	$3.840*10^{-5}$
AQuA	$< 1*10^{-15}$	>0.9999		$< 1*10^{-15}$
MSparkles	$3.741*10^{-5}$	$3.84*10^{-5}$	$< 1*10^{-15}$	

Table 12: P-values between all peak amplitudes by analysis tool in awake state. *P-values indicate statistically significant differences between the results obtained by different analysis applications analysing transients of awake mice. Graphical data shown in Figure 31.*

	CHIPS	CaSCaDe	AQuA	MSparkles
CHIPS		$< 1*10^{-15}$	$< 1*10^{-15}$	$6.206*10^{-12}$
CaSCaDe	$< 1*10^{-15}$		0.2732	$< 1*10^{-15}$
AQuA	$< 1*10^{-15}$	0.2732		$< 1*10^{-15}$
MSparkles	$6.206*10^{-12}$	$< 1*10^{-15}$	$< 1*10^{-15}$	

Table 13: P-values between all measured signal durations by analysis tool during anesthesia. *P-values indicate statistically significant differences between the results obtained by different analysis applications analysing transients of anesthetized mice. Graphical data shown in Figure 31.*

	CHIPS	CaSCaDe	AQuA	MSparkles
CHIPS		0.0377	$1.5643*10^{-4}$	$8.2352*10^{-9}$
CaSCaDe	0.0377		$2.5638*10^{-5}$	$7.1187*10^{-5}$
AQuA	$1.5643*10^{-4}$	$2.5639*10^{-5}$		>0.9999
MSparkles	$8.2352*10^{-9}$	$7.1187*10^{-5}$	>0.9999	

Table 14: P-values between all measured signal durations by analysis tool in awake state. *P-values indicate statistically significant differences between the results obtained by different analysis applications analysing transients of awake mice. Graphical data shown in Figure 31.*

	CHIPS	CaSCaDe	AQuA	MSparkles
CHIPS		$< 1*10^{-15}$	$7.8676*10^{-9}$	$1.0546*10^{-4}$
CaSCaDe	$< 1*10^{-15}$	$< 1*10^{-15}$	$< 1*10^{-15}$	$< 1*10^{-15}$
AQuA	$7.8676*10^{-9}$	$< 1*10^{-15}$		0.1712
MSparkles	$1.0546*10^{-4}$	$< 1*10^{-15}$	0.1712	

Table 15: Comparison of median peak amplitudes. *Median peak amplitude per field of view, extracted by Ca^{2+} analysis applications.*

Peak amplitudes	FOV 1		FOV 2		FOV 3	
	Anesthetized	**Awake**	**Anesthetized**	**Awake**	**Anesthetized**	**Awake**
CHIPS	1.086	1.564	0.551	1.215	0.786	1.646
CaSCaDe	1.952	1.449	1.699	2.227	2.406	2.916
AQuA	2.096	0.849	2.827	3.079	2.363	4.157
MSparkles	0.565	0.595	0.696	0.845	0.911	1.851

Table 16: Comparison of median transient durations. *Transient duration extracted by Ca^{2+} analysis applications.*

transient durations	FOV 1		FOV 2		FOV 3	
	Anesthetized	**Awake**	**Anesthetized**	**Awake**	**Anesthetized**	**Awake**
CHIPS	4.12	3.99	4.406	4.25	4.01	4.40
CaSCaDe	8.41	11.88	15.18	11.22	21.95	34.49
AQuA	1.98	1.32	2.7	2.10	2.40	5.55
MSparkles	2.80	2.85	3.599	4.02	4.243	22.51

Table 17: Comparison of detected ROIs. *Detected ROIs, false negative ROIs and signal counts. False negatives were assessed by careful manual evaluation in ImageJ for each application.*

#Rois / #fn (#sig)	FOV 1		FOV 2		FOV 3	
	Anesthetized	**Awake**	**Anesthetized**	**Awake**	**Anesthetized**	**Awake**
CHIPS	13/2 (32)	43/7 (70)	47/3 (139)	54/18 (175)	28/4 (78)	80/23 (265)
CaSCaDe	13/10 (30)	26/23 (147)	30/14 (50)	127/14 (588)	10/17 (13)	185/11 (534)
AQuA	11/11 (11)	58/12 (58)	24/17 (24)	91/24 (91)	7/20 (7)	306/14 (306)
MSparkles	85/6 (121)	105/12 (303)	71/8 (119)	121/14 (266)	29/8 (33)	114/7 (138)

Table 18: Mean ROI areas per FOV as detected by applications. *Mean areas of detected ROIS wich corresponding standard deviation, per FOV and condition.*

ROI area (std. dev.)	FOV 1		FOV 2		FOV 3	
	Anesthetized	**Awake**	**Anesthetized**	**Anesthetized**	**Awake**	**Anesthetized**
CHIPS	80.20 (102.85)	39.05 (38.08)	75.72 (103.68)	105.99 (442.85)	45.35 (38.74)	83.20 (91.35)
CaSCaDe	24.42 (19.15)	16.40 (14.02)	24.36 (14.37)	24.07 (15.43)	15.73 (10.22)	28.26 (22.86)
AQuA	17.78 (21.24)	73.97 (49.09)	17.38 (10.53)	24.08 (103.10)	14.54 (4.48)	26.89 (37.09)
MSparkles	16.67 (12.35)	14.00 (5.38)	26.41 (23.65)	48.36 (145.54)	19.95 (11.07)	218.84 (132.37)

Table 19:Comparison of signal kinetics.*Overall median peak amplitude and transient duration, as detected by the tested Ca^{2+} analysis applications.*

	Peak amplitude		Signal duration	
	Anesthetized	**Awake**	**Anesthetized**	**Awake**
CHIPS	0.768	1.380	4.264	4.255
CaSCaDe	1.846	2.799	14.69	26.070
AQuA	2.498	3.694	2.355	3.600
MSparkles	0.610	0.768	3.133	3.666

Table 20: Maximum synchronicity of GCaMP3 animals in percent. *FOVs exhibiting a high synchronous activity above 50% are marked green.*

	2821-FOV1	2821-FOV2	2821-FOV3	2821-FOV3_2	2823-FOV1	2823-FOV2	2823-FOV3	2823-FOV3_2	4053-FOV1	4053-FOV2	4053-FOV3	4053-FOV4
GCaMP3 anesthetized	19.79	9.468	11.59		11.2	8.393	8.333	8.473	13.56	15.47	11	16.29
GCaMP3 Awake	7.748	15.15	80.39	71.2	13.18	9.17	9.691	98.61	37.52	36.73	96.78	35.86

Table 21: Maximum synchronicity of GCaMP5 animals in percent. *FOVs exhibiting a high synchronous activity above 50% are marked green. FOVs exceeding the threshold due to low ROI counts are marked red.*

	0521 FOV1	0521 FOV2	0521 FOV4	0532 FOV1	0532 FOV2	0532 FOV3	0532 FOV4	0531 FOV1	0531 FOV2	0531 FOV3	0531 FOV4
GCaMP5 anesthetized	40.76	16.23	25.38	17.46	54.76	24.81	23.38	15.34	100	16.63	17.98
GCaMP5 awake	98.63	17.78	26.69	72.06	59.93	14.29	15.65	100	46.94	21.39	51.73

11 List of publications

Publications

Published

Franziska E. Müller, Volodymyr Cherkas, **Gebhard Stopper**, Laura C. Caudal, Laura Stopper, Frank Kirchhoff, Christian Henneberger, Evgeni G. Ponimaskin, Andre Zeug. Elucidating regulators of astrocytic Ca^{2+} signaling via multi-threshold event detection (MTED). | 2021 *Glia vol. 69, issue 12 -* PMID: 34388285 - https://doi.org/10.1002/glia.24070

Schweigmann M, Caudal LC, **Stopper G**, Scheller A, Koch KP and Kirchhoff F. *Versatile surface electrodes for combined electrophysiology and two-photon imaging of the mouse central nervous system.* | Front. Cell. Neurosci., 10 August 2021*. - PMID: 34447299 -* https://doi.org/10.3389/fncel.2021.720675

In Preparation

Gebhard Stopper, Laura C. Caudal, Lisa Felix, Laura Stopper, Christine R. Rose, Anja Scheller, Frank Kirchhoff. MSparkles – An open-source tool to visualize and analyze fluorescence events based on ion fluctuations in cells.

Carmen V. Kasakow, Laura Stopper, Laura C. Caudal, Alyssa M. Price, Svenja Linder, Qilin Guo, Raphaela XXX, Liu Qing, Xianshu Bai, **Gebhard Stopper**, Wenhui Huang, Anja Scheller, Frank Kirchhoff. Tamoxifen independent recombination of DNA (TIReD) in various glial Cre[ERT2] transgenic mouse lines

Caudal LC, **Stopper G**, Schweigmann M, Scheller A and Kirchhoff F (in preparation). In vivo contributions of astroglial GABA$_B$ receptors to pathological network function in temporal lobe epilepsy.

Rieder P, Gobbo D, **Stopper G**, Welle A, Damo E, Kirchhoff F, Scheller A Astrocytes and microglia exhibit cell-specific Ca^{2+} signaling dynamics in the murine spinal cord.

National & International conferences

Gebhard Stopper[1], Lea Kaschek[1], Marcel A. Lauterbach[2], Markus Hoth[1], Carsten Kummerow (2021) Towards automated tracking and analysis of individual killer cell cytotoxicity. Cell Physics 2021

Gebhard Stopper, Laura Stopper, Laura C. Caudal, Phillip Rieder, Anja Scheller and Frank Kirchhoff (2019) Analysis of multi-modal brain signals in awake mice. XIV European Meeting on Glial Cells in Health and Disease

Caudal LC, **Stopper G**, Schweigmann M, Bedner P, Steinhäuser C, Scheller A, Kirchhoff F (2019) In vivo contributions of astroglial receptors in pathological network function in temporal lobe epilepsy, XIV European Meeting on Glial Cells in Health and Disease

Schweigmann M, Caudal L, **Stopper G**, Scheller A, Koch KP, Kirchhoff F (2019), Exploring cortical brain Networks with flexible microelectrode arrays in parallel to two-photon imaging of anesthetized and awake mice. 13th Göttingen Meeting of the German Neuroscience Society

Caudal LC, Bai X, Bohn CV, Schlosser L, **Stopper G**, Schweigmann M, Scheller A, Kirchhoff F (2017) Contribution of glial transmitter receptors to pathological network function in mouse models of epilepsy. XIII European Meeting on Glial Cells in Health and Disease

Stopper G, Schweigmann M, Schlosser L, Scheller A, Koch KP, Kirchhoff F (2017) Recording and analysis of multi-modal brain signals in awake mice. XIII European Meeting on Glial Cells in Health and Disease

Gebhard Stopper, Laura Stopper, Laura C. Caudal, Anja Scheller and Frank Kirchhoff (2018) Automatic extraction and analysis of Ca^{2+}-signals in mice. Young Glia, Japan

Presentations

Gebhard Stopper (2018) Analysis of Ca^{2+} signals in mice. Presentation at Trends in Microscopy (TIM), Düsseldorf, Germany

12 Acknowledgements

First and foremost, my gratitude goes to Frank Kirchhoff. Frank, I'm grateful not only for giving me the opportunity to pursue a PhD, but for giving me the chance to look outside a computer scientist box. My time in your lab was great fun, I enjoyed working on various projects and of course participating to all the conferences and workshops. I'd also like to thank you for the great story I can tell about how I became a member of your lab (I always would drink the bottle of Argentinian wine and the Caipirinhas with you again).

I thank professor Peter Lipp for accepting to review my thesis.

Anja, thank you for the best Soljanka in the world, and (the admittedly weird sounding, but super delicious) Sauerkraut-Pizza. I loved the parties at you house and the movie nights. Thank you for all the lively discussions and input you gave me. It was always great fun working with you. I hope everything goes as planned with your new house, and you can enjoy it for a long time with you family.

A very special thank you goes out to André Zeug at the MHH in Hannover. I always enjoyed our discussions and our collaborations. Thank you for your support, your input and your constructive advice when I approached you with questions.

MiniMe! Ma soeur de parents différents. Nous avons le même sens de l'humour étrange et un esprit aussi tordu l'un que l'autre. Merci pour toutes les discussions et les contributions que tu m'as apporté. Merci d'avoir toujours voulu aller plus loin dans notre reflexion grâce à tes remarques, tes idées et d'avoir participer faire de MSparkles ce qu'il est aujourd'hui. Merci pour tout le fun que nous avons partagé!

Kitty-Cat, mon croissant préféré. J'ai caché du gingembre quelque part dans le laboratoire. Merci pour tous ces moments oú tu t'es plainte à moi et notre haine partagée pour les mêmes personnes. Nous avons passé de bons moments. A quand notre prochaine course ?

Davide (Don Gobbo) & Phillip (Herr Riederer), thank you for identifying tons of bugs, and showing all kinds of weird behavior of all kinds of devices and programs. You showed me things a computer can do (or not) I had never seen before (and never believed they were possible) in 15+ years of being a computer scientist. Most importantly, thank you for all the fun and discussions we had!